VGF growth of 4" GaAs single crystals with traveling magnetic fields

D I S S E R T A T I O N

zur Erlangung des akademischen Grades

doctor rerum naturalium
(Dr. rer. nat.)
im Fach Physik

eingereicht an der
Mathematisch-Naturwissenschaftlichen Fakultät
Humboldt-Universität zu Berlin

von
Dipl.-Phys. Alexander Glacki

Präsident der Humboldt-Universität zu Berlin:
Prof. Dr. Jan-Hendrik Olbertz

Dekan der Mathematisch-Naturwissenschaftlichen Fakultät:
Prof. Dr. Elmar Kulke

Gutachter:
1. Prof. Dr. Roberto Fornari
2. Prof. Dr. Peter Wellmann
3. Prof. Dr. Matthias Bickermann

eingereicht am: 15.05.2014
Tag der mündlichen Prüfung: 03.09.2014

Abstract

Within the framework of this thesis Si-doped and undoped 4" VGF-GaAs single crystals were grown under the influence of traveling magnetic fields (TMF). A KRIST$\widetilde{MAG}$® heater-magnet module (HMM) was used for the efficient simultaneous generation of heat and TMF during the process through a combination of DC and AC control. Growth experiments were carried out in a commercial VGF growth setup equipped with a single-crucible HMM and a newly designed VGF setup with a multi-crucible HMM.

The impact of the Lorentz force driven melt flow on the shape of the solid-liquid interface was analyzed in a TMF parameter study on frequency, phase shift, and current. With the application of suitable double-frequency TMF during growth, the interface deflection was reduced by about 30% and crucible contact angles increased within the order of 10%, compared to reference crystals grown without TMF. Furthermore, conventional growth conditions were improved by substituting graphite with isotropic BN as susceptor material. TMF application and the additional reduction of radial heat dissipation led to nearly continuously flat interfaces. Synergy effects of TMF application on process intensification approaches scale-up, speed-up, and numbering-up were successfully shown. Here, too, the positive TMF influence on process stability and interface shape was proven. Two 4" VGF-GaAs:Si single crystals were simultaneously grown under the influence of a TMF in the multi-crucible HMM. Obtained interfaces in both crystals were nearly symmetric and without tilting.

With TMF application changing structural and electronical properties as well as micro- and macrosegregation were investigated on Si-doped VGF-GaAs single crystals. Striations were observed in crystals grown without or too strong TMF ($\mathrm{Ta}_m > 1{\times}10^6$). Almost no micro-inhomogeneities were detected when the magnetic flux densities of the TMF were matched to the progression of solidification. With utilized TMF, induced melt flow opposed natural convection driven by buoyancy forces. Axial dopant incorporation was enhanced through a reduction of flow velocities and converging melt flow towards the center of the solid-liquid interface. The radial segregation profiles were flattened through a reduction of the concave deflection. Facets lengths in the crystal cone were found to be more stable with applied TMF. Further, the combined optimization of the conventional thermal setup and a reduction of the interface deflection with TMF application significantly reduced dislocation densities inside the crystals. An average EPD value around 100 cm^{-2} was obtained for GaAs:Si growth with a growth-matched double-frequency TMF and applied BN susceptor in the single-crucible VGF setup. Average EPD values around 500-1000 cm^{-2} were reached in simultaneously grown crystals within the multi-crucible VGF setup. EPD values in the lower crystal cylinder of semi-insulating GaAs crystals grown with TMF were around 2100-3600 cm^{-2} with cellular dislocation structures with up to several millimeters in diameter. The origin and trigger of with progressing growth emerging localized crucible-near polycrystalline transition areas was investigated. Evidence was found, that a local enhancement and bundling of dislocations close to the crystal edge resulted in the formation of small angle grain boundaries, which ultimately led to polycrystalline growth.

Zusammenfassung

Im Rahmen der vorliegenden Arbeit wurden Si-dotierte und undotierte 4" VGF-GaAs Einkristalle unter dem Einfluss von Wandermagnetfeldern (TMF) gezüchtet. Die für den Prozess benötigte Wärme und das Wandermagnetfeld wurden simultan mithilfe der kombinierten Regelung von Gleich- und Wechselströmen in einem KRIST$\widetilde{MAG}$® Heizer-Magnet-Modul (HMM) erzeugt. Alle Züchtungsexperimente wurden in einer kommerziellen VGF-Anlage mit eingebautem Eintiegel-HMM und in einer neu entwickelten VGF-Anlage mit Multitiegel-HMM durchgeführt.

Der Einfluss der durch die Lorentzkräfte angetriebenen Schmelze auf die Form der fest-flüssig Phasengrenze wurde innerhalb einer TMF-Parameterstudie von Frequenz, Phasenverschiebung und Stromstärke analysiert. Im Vergleich mit Referenzkristallen, welche ohne TMF gezüchtet wurden, zeigte sich, dass die Durchbiegung der Phasengrenze durch die Anwendung eines geeigneten Doppelfrequenz-TMF um etwa 30% verringert und der Kontaktwinkel am Tiegel um etwa 10% vergrößert werden kann. Des Weiteren wurden die konventionellen Züchtungsbedingungen optimiert, indem Graphit als Suszeptormaterial durch isotropes BN ersetzt wurde. Die dadurch zusätzlich reduzierte radiale Wärmeabfuhr und die Anwendung eines TMF führten in den Kristallen zu einer nahezu durchgehend ebenen Phasengrenzform. Zudem wurden Synergieeffekte von TMF-Anwendung und den Ansätzen zur Prozessintensivierung - Scale-Up, Speed-Up und Numbering-Up - für die Verbesserung der Prozesseffizienz erfolgreich nachgewiesen. Auch hier wirkten sich die angewandten Magnetfelder positiv auf Prozessstabilität und Form der Phasengrenze aus. Es wurden gleichzeitig zwei 4" VGF-GaAs:Si Einkristalle unter dem Einfluss eines TMF in einer Multitiegel-Anlage gezüchtet. Die dabei erlangte Phasengrenzform war in beiden Kristallen symmetrisch und nicht verkippt.

In gezüchteten Si-dotierten VGF-GaAs Einkristallen wurden sowohl die sich durch die Anwendung der Wandermagnetfelder veränderten strukturellen und elektronischen Eigenschaften, als auch Segregationseffekte untersucht. In Kristallen, welche ohne oder mit zu starkem ($\mathrm{Ta}_m > 1{\times}10^6$) TMF gezüchtet wurden, waren Wachstumsstreifen sichtbar. Wurde die magnetische Flussdichte des TMF an den Kristallisationsverlauf angepasst, konnten nahezu keine Mikroinhomogenitäten detektiert werden. Die durch das TMF induzierte Strömung der Schmelze wirkte der natürlichen Konvektion entgegen. Der axiale Einbau der Dotanden wurde durch die resultierenden verringerten Geschwindigkeiten in der Schmelze und die konvergierende Strömung entlang der Kristallachse mit TMF vergrößert. Mit der Verringerung der Konkavität der Phasengrenze ging zudem die Homogenisierung der radialen Segregationsprofile einher. Die Länge der Kristallfacetten stabilisierte sich durch den Einsatz der Wandermagnetfelder. Zusätzlich konnten die Versetzungsdichten innerhalb der Kristalle durch Optimierung des thermischen Aufbaus und der Phasengrenzform signifikant reduziert werden. Mithilfe eines dem Züchtungsverlaufes angepassten Doppelfrequenz-TMF sowie der Nutzung eines BN-Suszeptors in der Eintiegel-VGF-Anlage, wurde eine durchschnittliche EPD von 100 cm^{-2} in einem GaAs:Si Kristall erzielt. Die gleichzeitig in der Multitiegel-VGF-Anlage gezüchteten Einkristalle besaßen eine durchschnittliche EPD von 500-1000 cm^{-2}. In mit TMF

gezüchteten halbleitenden GaAs Kristallen wurden im unteren Kristallzylinder EPDs zwischen 2100-3600 cm^{-2} gemessen. Die Zellgrößen der Versetzungsstruktur überschritten im Kristallinnern Durchmesser von mehreren Millimetern. Der Ursprung und der Auslöser, der mit fortschreitendem Wachstum lokal in Tiegelnähe auftretenden polykristallinen Übergangsbereiche, wurde näher untersucht. Die Ergebnisse weisen darauf hin, dass eine örtliche Ansammlung und Bündelung von Versetzungen am Kristallrand zur Bildung von Kleinwinkelkorngrenzen und letztlich zu polykristallinem Wachstum führt.

Contents

Nomenclature

List of abbreviations

AC	alternating current
AMF	alternating magnetic field
CFD	computational fluid dynamics
CMF	carousel magnetic field
DC	direct current
DS	directional solidification
DSL	diluted Sirtl with light
EPD	etch pit density
HMM	heater-magnet module
IRT	infrared transmission
LEC	liquid-encapsulation Czochralski
LST	laser scattering tomography
RMF	rotating magnetic field
SC	semiconducting
SI	semi-insulating
SIMS	secondary ion mass spectroscopy
TMF	traveling magnetic field
VB	vertical Bridgman
VCz	vapor-pressure-controlled Czochralski
VGF	vertical gradient freeze

List of symbols

α	contact angle solid/crucible
β	angle between crucible and melt isothermal line
ΔH	specific latent heat of fusion
$\Delta z/R$	deflection of the solid-liquid interface
Δ	convexto-diffusive parameter
δ	thickness of solute boundary layer
λ	wavelength of the traveling magnetic field
$\lambda_{s,l}$	thermal conductivity in solid, liquid
μ	charge carrier mobility
$\nabla T_{s,l}$	thermal gradient in solid, liquid
ν	kinematic viscosity

ω	angular frequency
ϕ	phase shift between neighboring coils
ρ	electrical resistivity
$\rho_{s,l}$	density of solid, liquid
σ	electrical conductivity
$\vec{b}$	Burgers vector
$\vec{u}_{melt}$	flow velocity of the melt
$\vec{v}$	velocity of the traveling field
a, b	fitting parameters after Czapelski [Cza98]
B	magnetic flux density
c	concentration
D	diffusion coefficient
d	distance between coils
d_c	dislocation cell diameter
$D_{in,out}$	inner/outer diameter of coils
E	electric field
f	frequency of the traveling magnetic field
F_L	Lorentz force
F_{buo}	buoyancy force
g	solidified fraction
h	height of coils
I	electrical current
j	current density
K	curvature of the interface
k	wavenumber
k_0	equilibrium distribution coefficient
k_{eff}	effective distribution coefficient
L	total melt height
N	number of coils windings
n	charge carrier density
n_{crit}	critical particle number for nucleation
q	heat flux
R	radius of the melt column
r, z, φ	cylindrical coordinates
r_{crit}	critical radius for nucleation
T	temperature
t	time
T_m	melting temperature
v_{gr}	growth velocity
Ta_m	dimensionless magnetic Taylor number

1 Introduction

The III-V compound semiconductor gallium arsenide (GaAs) is, apart from silicon, the most deployed semiconductor material. Due to its electronical properties, it is widely used for high-frequency microelectronics. Transistors with very short switching times and high operating frequencies can be manufactured. Monolithic microwave integrated circuits (MMIC) based on semi-insulating (SI) GaAs not only dominate the market for power amplifiers and switches in telecommunication devices, but are also important components for sensor technologies in satellites, radar systems and Wi-Fi. Furthermore, semiconducting (SC) GaAs is an essential substrate material for opto-electronic devices, like light-emitting and laser diodes (LEDs and LDs). In addition to the use of LEDs for long-life and energy-saving lighting, GaAs-based LDs are applied in fiber optic networks.

In the last years, strong growth of the GaAs market took place, mainly because of the rapid increase of smartphone shipments and the coupled development of 3G mobile telecommunication technologies [Hig13]. But also rising data demand in wired networks, e.g. for high-definition video-on-demand services, provided strong growth for GaAs power amplifiers. The global rising application of LEDs in displays and the automotive sector are likely to overhaul the SI GaAs market in the next years [Yol12]. At present, wafers with 6" and 4" diameter represent about 98% of the total market by area, with a share of crystals grown with vertical gradient freeze (VGF) or vertical Bridgman (VB) technique of about 80% [Hig12]. The successful growth of 8" VGF-GaAs was demonstrated [Ste03]. For a high degree of usability of the with epitaxial processes manufactured devices, high-quality single-crystalline GaAs substrate material with a low dislocation density is of upmost importance. This is the reason why VGF/VB replaced the liquid-encapsulation Czochralski (LEC) process since the beginning of 2000s.

Aim of ongoing research is, in addition to structural improvement of the GaAs single crystals, the enhancement of the yield per growth process and a reduction of the process costs. Quality criteria for wafers are low dislocation densities, small residual stress, and uniform structural and electronic properties on the whole wafer area. The shape of the solid-liquid interface during growth is one of the most important factors for determination of the final crystals properties.

Process enhancement approaches are, e.g. increasing the crystallization rate, increasing the diameter and length of the crystals, and the simultaneous growth of multiple crystals in one setup. Within all these attempts, rising problems with heat and mass transport during crystallization are of paramount importance, which can significantly decrease crystal quality and leaves the above mentioned quality requirements unfulfilled. Finding a possibility to influence melt flow and interface

morphology in VGF-GaAs growth is therefore decisive for process enhancement. Its development has to consider industrial feasibility and setup costs, too.

1.1 Motivation and objectives

The shape of the solid-liquid interface in VGF crystal growth is determined by heat transfer. The generated latent heat and the thermal conductivities of the liquid and solid phase, the confining crucible, crucible support etc. are the main parameters affecting the interface morphology. In semiconductor material, the thermal conductivity of the melt is larger than in the crystal. If the crucible materials thermal conductivity is larger, too, the semiconductor material is cooled through the crucible contact, which results in concave interface deflections. The negative effects are, e.g. high thermal stress, large radial inhomogeneities on a wafer, and enhanced tendency of polycrystalline growth.

Various methods were proposed to achieve flat or even slightly convex interfaces, e.g. localized heating of the crucible surface near the axial location of the interface or Peltier cooling of the interface [Jas85], but their wide-ranging applicability failed because of complex experimental setup requirements.

Recently, Zhang et al. [Zha12] reported on a new approach to achieve convex shaped interfaces using a "bell-curve" axial temperature profile in the melt during growth of cadmium zinc telluride with the electrodynamic gradient freeze technique with 18 controlled heating zones. Based on numerical simulations, with such a temperature profile the upper melt region was colder than the melt near the interface. This introduced a significant change and redirection of the heat flow. Result was a uniform mainly convex interface shape during the entire growth run when the "bell-curve" profile was dynamically adapted. However, such a method is not easily transferable to VGF-GaAs growth. First, the temperature gradients are mainly adjusted by the bottom and top heaters and only a small number of heating zones are available. Side heaters primarily maintain the unidirectional heat flow along the axis. The adjustment of a dynamic "bell-curve" profile is therefore difficult. Secondly, the danger of freezing of the upper melt region with liquid underneath is enhanced, which could damage crystal and the growth setup.

Nevertheless, controlling the melt flow is very promising in order to influence the interface shape. Molten semiconductor materials have high electrical conductivities. Therefore, magnetic fields can be used to induce a Lorentz force for a effective control of the melt flow. The heat dissipation and mass transport can be influenced during the growth process. Appropriate Lorentz force fields have the potential to flatten the concave interface, to reduce the melt interaction with the crucible wall and to improve the process stability with increasing melt volumes. Hence, they may be the favorable tool to simultaneously increase process yield and crystal quality.

Especially, the application of traveling magnetic fields (TMF) in melt growth features several advantages [Rud08a]. It induces axisymmetric Lorentz force fields with the capability of counteracting the natural buoyancy force. Their applica-

tion was studied extensively, both numerically and experimentally, e.g. for the directional solidification (DS) of multicrystalline silicon [Kud13, Dad13, Dro11] and VGF growth of various materials [Sch04b, Lan08, FR09, Dro12a]. Improvements of the solid-liquid interface shape and thermal stress, reduced micro-inhomogeneities and enhanced melt mixing were reported. While a multiplicity of numerical investigations on VGF/VB-GaAs with TMF [Lyu04, Gra09, Dro13a] was performed, experimental results from VGF-GaAs with TMF are scarce. In the thesis of Lantzsch [Lan09] results from the growth of semiconducting 3" VGF-GaAs grown with a combined TMF/DC (TMF + direct-current induced steady magnetic field) field were reported. TMF frequencies varied between 10-800 Hz. The concave deflection of the solid-liquid interface was slightly reduced with downward-directed TMF, but the sole employment of a TMF resulted in an unsteady flow and the generation of undesired striations. They were suppressed only with the additional application of a damping steady magnetic field. However, unfavorable was the structure of the experimental setup. The TMF/DC field was generated with external coils outside of the growth vessel. Because of the shielding of the steel furnace jacket and the side heaters as well as the distance between coils and melt, such a setup lacks in efficiency. Larger needed currents for the generation of the magnetic field significantly increase energy consumption. Furthermore, in this setup only small currents of up to 20 A per winding and a fixed phase shift between the coils of 60° limits the parameter range for optimization of the TMF impact on the melt.

Within the KRIST$\widetilde{MAG}$® project (2005-2008) at the Leibniz Institute for Crystal Growth Berlin the heater-magnet module for the combined generation of heat and TMF in vertically stacked graphite coils was developed [Rud08a]. Here, the side heater-magnets inside the VGF furnace are provided with a combination of direct current and alternating current (AC). Hence, TMF and the thermal field for crystal growth are simultaneously supplied. The generation of the TMF in immediate vicinity of the melt is efficient and energy-saving.

Further advantage of the heater-magnet module is the freely selectable AC phase shift between 0-120°, high possible currents up to 330 A, a frequency range of 10-600 Hz, and the possible application of a double-frequency TMF, each with its own set of parameters. An optimization of the melt flow conditions during VGF growth benefits from this broad range of possible TMF parameter adjustments.

This concept was tested for VGF growth of 4" germanium [FR09, FR12]. Germanium, with its low melting point and its high electrical conductivity, served as a model substance for VGF growth with utilized TMF. Optimized downward-directed traveling magnetic fields led to a flat/slightly convex interface shape with significantly reduced micro-inhomogeneities. Furthermore, radial homogeneity of the electrical parameters were improved and the dislocation density on a wafer was slightly reduced compared to crystals grown without TMF.

The material parameters, that are important for VGF growth of Ge and GaAs, are compared in table 1.1. Compared to Ge, the GaAs material properties are rather unfavorable. The biggest challenge for VGF-GaAs growth is to remove the large

	Germanium	Gallium arsenide
melting temperature T_m[°C]	937	1238
thermal conductivity [W/mK]		
in the liquid λ_l	39.0	17.8
in the solid λ_s	17.7	5.4
electr. conductivity liquid σ[1/Ωm]	1.5×10^6	7.9×10^5
latent heat of fusion ΔH[kJ/mol]	34.7	105.4
kinematic viscosity ν[m^2/s]	1.4×10^{-7}	4.9×10^{-7}

Table 1.1: Comparison of important material parameters of Ge and GaAs, values taken from [Hur95] and [Wun06]

latent heat from the interface, due to the small thermal conductivity in the solid. With a smaller electrical conductivity and larger kinematic viscosity of the melt, stronger TMF are needed to influence the melt flow. In summary, a reduction of the interface deflection and a general improvement of the crystal quality is challenging.

Within the framework of this thesis, the growth of industrial-sized 4" semiconducting and semi-insulating GaAs in a heater-magnet module was tested. This investigation was conducted during my work at the Leibniz Institute for Crystal Growth Berlin. Objective of this work was, to use the wide range of TMF parameters provided by the heater-magnet module for experimental analyses of the interface shaping potential of VGF-GaAs. Grown crystals were analyzed with respect to interface shape, micro-inhomogeneities, electronic and structural properties as well as macrosegregation. Additionally, the effect of unwanted polycrystalline growth starting near the crucible wall, especially occurring in semi-insulating GaAs, was further investigated.

Compared to other experimental investigations on the effects of a TMF on the melt in VGF/VB growth for various materials, this work was not realized in model systems and/or in a laboratory scale. Furthermore, through the effective and efficient generation of the TMF in the heater-magnet module, the usability of the KRIST$\widetilde{MAG}$® concept for VGF-GaAs growth on an industrial scale was examined. Additionally, synergy effects of the utilization of a TMF for process intensification, i.e. scale-up, speed-up, and numbering-up, were analyzed. Particular attention was put on the numbering-up concept: Within this work, knowledge was transferred from single-crucible VGF growth with TMF to a multi-crucible VGF growth setup. Simultaneous growth of multiple crystals in one growth run with an applied TMF was carried out.

1.2 Structure of this thesis

In chapter 2, the theoretical background of VGF-GaAs growth with TMF is discussed. First, VGF growth related phenomena like heat flux, micro- and macrosegregation and the issue of unwanted polycrystalline growth near crucible wall is ad-

dressed. Furthermore, general properties of VGF grown doped and undoped GaAs crystals are outlined. In the second part, the use of external force fields in VGF is introduced. Main emphasis lies on the utilization of traveling magnetic fields and the KRIST$\widetilde{MAG}$® technology. The generation of a TMF in a heater-magnet module is deduced. Numerical and experimental prior knowledge on state of the art crystal growth in a heater-magnet module is presented.

In chapter 3, methods of process intensification are illustrated and it is discussed how related obstacles can be conquered with the use of a TMF. Within the numbering-up method, the concept of the multi-crucible heater-magnet module is introduced. Numerical simulations and characterization methods to analyze the shape of the solid-liquid interface and other crystal properties are explained.

In chapter 4, the single-crucible VGF setup and the newly developed multi-crucible VGF setup are described. Focus is put on the extension of the already existing single-crucible VGF setup to GaAs growth and the installation of the new multi-crucible VGF growth setup. Optimization of the thermal design layout and temperature profile measurements are outlined. In addition, the preparation steps before growth, features of the growth process, and sample preparation are illustrated. Furthermore, the technique to mark the solid-liquid interface with the use of the TMF is presented.

In chapter 5, the impact of TMF on the interface morphology in the single- and multi-crucible VGF setup is shown. A TMF parameter study addresses the influence of TMF frequency, phase shift, and current on the solid-liquid interface shape. Growth with and without TMF is directly compared. Process optimization by introducing a new susceptor material and growth-matched TMF parameters is outlined. Furthermore, results from the process intensification approaches scale-up and speed-up with applied TMF in the single-crucible VGF setup are presented. The start-up of the multi-crucible VGF setup is described and outcomes from test runs and first numbering-up growth experiments with TMF are displayed.

In chapter 6, general effects of the utilization of a TMF on crystal properties of GaAs:Si and semi-insulating GaAs are described. Differences in micro- and macrosegregation, as well as the influence of the TMF on faceting, dislocations, and residual stress is analyzed in GaAs:Si crystal grown with various TMF parameters. The section on the growth of SI GaAs concentrates on properties of crystals grown with optimized interface shapes. The issue of polycrystalline growth developing in the crystal cylinder near the crucible wall is extensively treated. Origin and trigger of this yield-reducing phenomenon is investigated.

In chapter 7, all results are being summarized and evaluated. In chapter 8, an outlook on future strategies on process intensification approaches with TMF is given. The application of other magnetic field types in VGF-GaAs growth is discussed.

2 Theoretical principles

2.1 Vertical gradient freeze of gallium arsenide

In the vertical gradient freeze (VGF) process a crystal is directionally solidified with a vertical temperature gradient within a crucible. In contrast to the related Vertical Bridgman (VB) technique, where the crucible and the heaters are shifted with respect to each other through a steady temperature profile for solidification with stable gradients, in the VGF process both crucible and heaters are fixed. In this mechanically rather simple setup, temperature controllers for each heater are used to create and adjust a desired time-dependent axial gradient field. At the same time, the temperatures at various places within the setup are the only control entities.

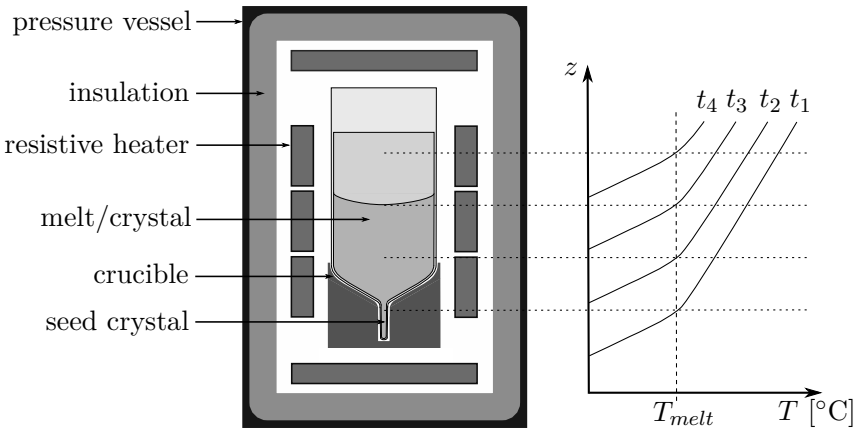

Figure 2.1: Sketch of a typical VGF growth setup and the corresponding temperature profiles during the growth process with interface position at t_3 ($t_1 < t_2 < t_3 < t_4$), the crystal is directionally solidified through cooling within a vertical temperature gradient

The typical growth setup and the corresponding temperature profiles during the growth process are depicted in Fig. 2.1. Within pressure vessel and insulation, resistive top-, bottom-, and several side heaters are located around the melt container. The polycrystalline feedstock is loaded into the cylindrical crucible and heated up until it is molten. A seed crystal is located in the bottom of the tapered crucible. The monocrystalline seed has a given orientation and determines the orientation of the growing single crystal. Only the upper part of the seed is molten where-

upon the cooling and the solidification starts. A given control vertically shifts the temperature gradients, the crystal is growing from bottom to top. It adopts the monocrystalline structure from the seed. The growth velocity v_{gr} depends on the adjusted axial thermal gradients $\frac{\partial T}{\partial z} = \nabla T$ and the cooling rate. Both parameters can be simultaneously controlled via the heater power.

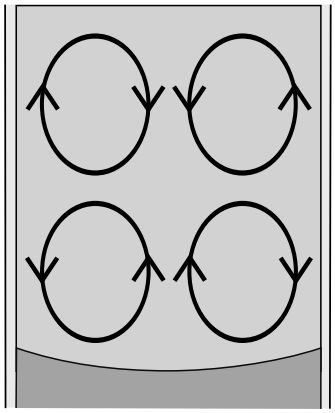

Figure 2.2: Sketch of the natural flow field during conventional VGF growth of GaAs and the related concave interface morphology

Convection in the melt is generated by varying radial thermal gradients along the axis. A natural double meridional vortex flow is generated by the heat flow and the released latent heat at the solid-liquid interface (see Fig. 2.2) [Pae02a, Nie11]. The magnitude of the radial gradient in the upper melt area is usually stronger than in the lower area, resulting in a stronger upper vortex flow and poorer melt mixing near the interface [Pae13]. The downwards-directed heat dissipation is mainly influenced by the difference in heat conductivities of the liquid and solid phase. In semiconductor material the heat conductivity in the solid is smaller than in the liquid. The position and the form of the solid-liquid interface during growth is determined by the thermal heat flux of the melt, the crystal, the crucible and the crucible support. A favorable flat interface shape is created when the radial temperature gradient is zero. In this case the thermal stress is minimized which leads to reduction of the dislocation density [Bir03]. The growth velocity is determined by the heat flux balance [Eic08a]:

$$v_{gr} = \frac{q_l - q_s}{\Delta H \rho_s} = \frac{\lambda_s \nabla T_s - \lambda_l \nabla T_l}{\Delta H \rho_s} \tag{2.1}$$

where ΔH denotes the latent heat, $q_{s,l}$ the heat flux, $\rho_{s,l}$ the density, and $\lambda_{s,l}$ the thermal conductivity of the solid and the liquid, respectively. The growth velocity is limited to the case of ∇T_l=0

$$v_{gr,max} = \frac{\lambda_s \nabla T_s}{\Delta H \rho_s}. \tag{2.2}$$

The released latent heat across the interface and the transported heat from the melt to the interface have to be removed efficiently in order to ensure maximum growth velocities. Therefore, the axial thermal gradients in the crystal should be larger than in the melt (see Fig. 2.1).

The application of the VGF process for the growth of high quality III/V-materials was initially proposed by Gault et al. [Gau86]. Typical temperature gradients in VGF of GaAs are 2-5 K/cm and growth velocities are between 2-4 mm/h. The other main techniques for growing GaAs single crystals are the liquid-encapsulation Czochralski (LEC) and the vapor-pressure-controlled Czochralski method (VCz). In the LEC method, large temperature gradients around 100 K/cm allow an efficient heat removal from the interface and therefore larger growth velocities, typically around 7-10 mm/h for crystals larger than 3" [Shi93, Jur05]. Typical growth parameters for the VCz of GaAs are gradients of 20-40 K/cm and growth rates of 3-5 mm/h [Neu01]. Compared to the Czochralski processes, the significantly lower nonlinearities of the temperature field in the VGF cause a reduction of thermal stress during the process [Ind79] and therefore crystals with less dislocations can be grown. State-of-the-art VGF growth of GaAs is characterized by etch pit densities (EPD) below 500 cm^{-2} for 4"-GaAs:Si and around 1300 cm^{-2} for undoped 4"-GaAs [Bir03, Bue01]. This is about one order of magnitude smaller compared to LEC growth [Jur05]. Additionally, diameter control is not necessary due to the predetermined crucible form in VGF growth. Losses during wafering of the crystal are minimized. Certainly disadvantageous is the crucible contact, which can lead to parasitic nucleation and mechanical stress. Additionally, small temperature gradients are accompanied by small growth velocities. By now, VGF grown GaAs single crystals with diameters up to 200 mm have been reported [Ste03]. A more extensive review of the functional principles, advantages, and disadvantages of these and further growth techniques with particular respect to the growth of semi-insulating GaAs is given by Rudolph and Jurisch [Rud99].

Since the As-equilibrium vapor pressure at the melting point is about 2 bar (see Fig. 2.5) the GaAs melt tends to decompose [Hur99]. One possibility to avoid decomposition is growth in a sealed quartz ampoule. An additional As source is heated up to around 617°C to create an arsenic atmosphere over the stoichiometric GaAs melt. Such a setup was applied in numerous studies [Fra95, Wun06, Lan09] and in industry [Mar08]. A second approach is the growth in a open system with the encapsulation of the melt with liquid boron oxide (B_2O_3) and an applied inert gas counter pressure to suppress As evaporation. Such a setup is characterized by a reduced complexity and superior upscaling potential [Bir03]. It is therefore in particular suitable for industrial production [Jur05].

The factual standard crucible material for GaAs growth is pyrolytic boron nitride (pBN). It is chemically inert and has a similar thermal expansion as GaAs. Reusability of the crucible and a non-destructive removal of the grown GaAs crystal can be assured. But the utilized pBN crucibles show highly anisotropic thermal conductivities with a higher value along the wall (about 27:1 [Shi09]) because of their layered

structure. Together with the comparatively rather poor thermal conductivity of the GaAs crystal and the large latent heat of fusion, the heat removal occurs to a great extent towards the sides. This results in a concave interface shape (see Fig. 2.2) and thermal stress along the interface [Eic08a]. High growth velocities increase the concavity of the interface due to larger extend of latent heat release per time unit and therefore amplify the thermal stress. Hence, optimization of heat dissipation is of great importance. For example, the adjustment of the thermal conductivity of the crucible support increases the axial temperature gradients near the seed and improves heat dissipation along the crystal [Bir03].

2.1.1 Melt-crucible contact and unwanted nucleation

Despite its non-reactivity, the direct contact of the melt and the pBN crucible can cause random nucleation of low angle grain boundaries and contamination. Bourret and Merk showed that besides the prevention of arsenic evaporation, a complete coating of the melt with B_2O_3 prevented the contact with the crucible wall [Bou91]. The residual water content of the B_2O_3 was revealed to influence the wetting behavior and the properties of the GaAs. Reactions between encapsulation and GaAs melt effected concentrations of Si, B, and C inside the crystals, which will be discussed in detail later.

However, transitions to polycrystalline growth starting at the crucible wall, often near the <110>-directions for growth in [001]-direction, are still a pronounced problem, which significantly reduces the monocrystalline yield of a growth run [Jur05]. The mechanisms of the occurrence is not yet completely understood, but there seem to be several influencing factors.

One reason for polycrystalline growth can be the formation of a supercooled area near the crucible wall. Due to dispersive adhesion a contact angle between melt and crucible develops and bends the interface near the crucible wall, as shown in Fig. 2.3. The model of the development of a supercooled region near the three-phase boundary has to be complemented when full wetting of the pBN crucible with liquid B_2O_3 is assumed. But B_2O_3 has with λ_l=1.8 W/mK at melting temperature the same thermal conductivity like the pBN crucible in radial direction. Therefore a large influence is not to be expected.

Because of the Gibbs-Thomson effect, an interface with a curvature K has a lower melting point compared to a flat interface [Vol99]. Here, the melting temperature is reduced by the supercooling of the curvature

$$\Delta T_K = K \cdot \frac{\sigma T_m}{\Delta H \rho_s} \tag{2.3}$$

where σ is the surface energy, ΔH the specific latent heat, and ρ_s the density of the solid phase. A supercooled area develops in contact with the crucible, which size is dependent on the contact angle α and the angle β between the crucible wall and the melt isothermal line. The temperature along the interface T_I can now be written as

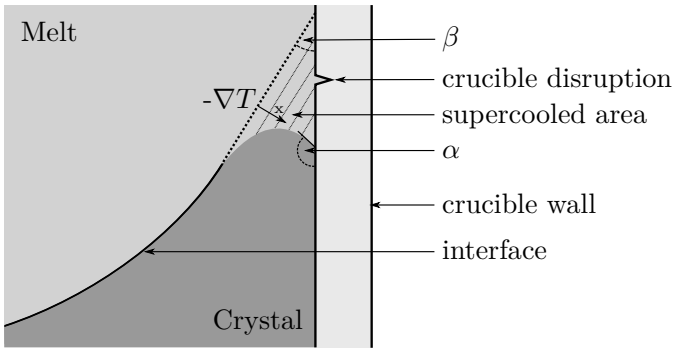

Figure 2.3: Model of the development of a supercooled area near the three phase boundary caused by the Gibbs-Thomson effect. The size of the supercooled area is substantially dependent on the angle β between the crucible wall and the melt isothermal line. It reaches values for a small β of few hundreds of nanometers [Eic05].

[Eic05, Dre08]:

$$T_I = T_m \left(1 - \frac{\nabla T \cdot x}{T_m}\right) = T_m \left(1 - K \cdot \frac{\sigma}{\Delta H \rho_s}\right) \tag{2.4}$$

In the supercooled area, homogeneous and heterogeneous nucleation can occur. The latter is strongly dependent on material parameters and surface geometry of the crucible. The generated nucleus is assumed to be spheric. The critical radius is identical for homogeneous and heterogeneous nucleation [Wil88]:

$$r_{crit} = \frac{2\sigma T_m}{\Delta H \rho_s \Delta T} \tag{2.5}$$

with the supercooling $\Delta T = T_m - T_I$. However, the critical particle number for the formation of a new nucleus n_{crit} is dependent on the volume and the geometry function F, where $F = 1$ for homogeneous nucleation and $0 < F << 1$ for heterogeneous nucleation on crucible disturbances like indentations [Dre08]:

$$n_{crit} = F \cdot \frac{32\pi\sigma^3 T_m^3}{3m(\Delta H)^3 \rho_s^2 (\Delta T)^3} \tag{2.6}$$

Dreyer et al. [Dre08] numerically investigated the critical particle numbers for homogeneous and heterogeneous nucleation in GaAs, assuming the number of accidentally colliding atoms for nucleus formation in the liquid is less than 100. After equation 2.6 homogeneous nucleation in GaAs requires ΔT>240 K for $n_{crit} < 100$, but nucleation already occurs already for ΔT around 5 K [Eic05]. Thus, heterogeneous nucleation must be the responsible effect. For crucible disruptions at the triple point with very small cone angles <11° and a small contact angle α=80° the critical particle

number is below 100. However, it has to be acknowledged that $\beta<0.002°$ is required for supercooling in the range of a few Kelvin. This demands very large interface deflections accompanied by an increase of the size of the supercooled area. Temperature fluctuations enhance the possibility of polycrystalline growth. Marchenko et al. connected the frequency of defect appearance to growth specific numerical characteristics for a vast number of growth experiments of 6" VGF-GaAs [Mar08]. They found the scatter of the heat flux at the solid-liquid interface to be an indicator the process stability during a growth run. Large growth velocities and small temperature gradients both led to larger supercooled areas and favored heat flux scattering. In such experiments a significant decrease of yield was observed. The role of faceting is disregarded in previous assumptions but may contribute to the phenomenon of polycrystalline growth. For example, the tendency of twin formation was correlated to the occurrence of facets [Hur95, Amo98]. Here, too, temperature gradients, interface shape, and temperature fluctuations had large influence on facets and had to be optimized to avoid twinning.

Independent from these considerations, other investigations about the cause of the polycrystalline growth reached different conclusions. Tower et al. found the onset of polycrystallinity for 3"- and 4"-LEC-GaAs to be triggered by the increase of interface curvature near the crystal rim [Tow91]. Grain boundary formation was caused by gallium droplets in this region, that migrated from the crystal surface to the interface. Arsenic evaporates preferentially from {110} planes, which is why the disturbances occurred mostly in this direction. Shibata et al. identified an accumulation of dislocations at any concavity of the solid-liquid interface to be the origin of polycrystalline growth in 3"-LEC-GaAs [Shi93]. Grown-in dislocations propagating perpendicular to the interface tended to gather towards the center of the concavity. The control of the interface shape successfully suppressed polycrystalline growth. Investigations on polycrystallinity in VB-GaAs growth by Althaus et al. resulted in the dependency on the wettability of the crucible by B_2O_3 [Alt96]. When the quartz crucible was coated with pyrolytic graphite or pyrolytic BN, the wettability was reduced and polycrystalline areas were observed. Their development started when very high dislocation densities above 5×10^5 cm^{-2} were reached. Small angle grain boundaries were formed, which subsequently started to coalesce. These small angle grain boundaries multiplicated and ultimately grains were formed. It was concluded that polycrystalline growth is attributed to As leakage through the reduced coating, which resulted in the nucleation of dislocations.

In summary it can be said, that the crucible contact causes, but not necessarily triggers polycrystalline growth. An approach to prevent crucible contact is detached growth. During solidification a gap between the crucible wall and the growing crystal is established through the formation of a melt meniscus. Here, a suitable pressure at the meniscus is counterbalancing the hydrostatic pressure of the melt and the pressure above the melt [Duf00]. Consequently without crucible contact, a reduced thermal and mechanical stress and a reduced interface deflection [Pae05] causes a higher structural perfection of the crystals. Germanium with diameter up to 3" were

grown so far [Lan10]. However, disadvantageous is that the application is limited to the ampoule growth variant.

2.1.2 Solute transport and segregation

Segregation phenomena, both microscopic and macroscopic, result from the differences of solubility of foreign atoms in the solid and in the liquid phase. The incorporation of dopants influences structural and electronic properties of the grown crystals. Therefore, the knowledge of the incorporation mechanisms and distribution of desired and undesired impurities in the crystal lattice is crucial.

In this section the following assumptions are made: Complete mixing of the dopants in the melt, diffusion in the solid is neglected, the growth rate is constant, and the solute concentration in the liquid phase is constant with the value $c_{l,\infty}$ sufficiently far away from the interface.

Axial macrosegregation

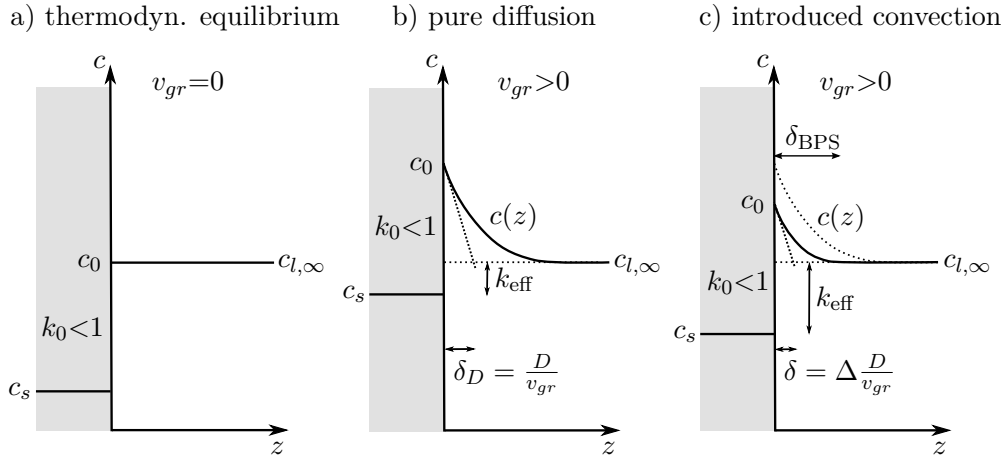

Figure 2.4: Illustration the solute concentrations in the melt c_0, $c_{l,\infty}$ and in the crystal c_s, of the solute boundary layer δ, and the variability of the effective distribution coefficient k_{eff} for $k_0 < 1$ for growth in z-direction: a) in thermodynamic equilibrium, b) for the case of pure diffusion and c) with increasing convection (inspired by [Ubb12])

Axial macrosegregation is the non-uniform distribution of solutes along the growth direction of a crystal. It occurs during the directional solidification process with an initial concentration of impurities and dopants in the melt. It can lead to an axial enrichment or depletion of impurities and dopants in the growing crystal with the progression of the process.

The ratio of the solute concentration in the solid and the liquid phase in the thermodynamic equilibrium is defined by the distribution coefficient k_0 (see Fig.

2.4a):

$$k_0 = \frac{c_s}{c_0} \tag{2.7}$$

For k_0<1, solidification of a small melt portion will result in a concentration in the solid c_s<c_0 and the remaining concentration in the liquid will rise. There is an enrichment of the concentration c_s with progression of the growth of the crystal. For k_0>1 the solute concentration c_s is larger than c_0 and the concentration in the solid diminishes during growth.

The transport of solutes in a melt and at the solid-liquid interface is governed by contributions of diffusion and convection. Both effects have to be considered to describe the incorporation mechanisms during crystal growth [Cam86]. The following relation describes the progression of the solute concentration c with a moving growth front [Gar94]

$$\frac{\partial c}{\partial t} = D\nabla^2 c + (\vec{v}_{gr} \cdot \nabla)c - (\vec{u}_{melt} \cdot \nabla)c \tag{2.8}$$

where D is the diffusion coefficient, $\vec{v}_{gr}$ the growth velocity, and $\vec{u}_{melt}$ the velocity of the melt flow. Tiller et al. treated the mass transport as a one-dimensional steady-state problem and neglected melt convection [Til53]

$$D\frac{\partial^2 c}{\partial z^2} + \vec{v}_{gr}\frac{\partial c}{\partial z} = 0. \tag{2.9}$$

With boundary conditions for $z = 0$

$$D\left(\frac{\partial c}{\partial z}\right)_{z=0} = -\vec{v}_{gr}(c_0 - c_s) = -\vec{v}_{gr}(1 - k_0)c_0 \tag{2.10}$$

and for z=∞

$$c = c_{l,\infty} \tag{2.11}$$

the solution of the pure diffussive problem is given as (see Fig. 2.4b)

$$c(z) = c_{l,\infty} \cdot \left[1 + \frac{1 - k_0}{k_0}\exp\left(-z\frac{v_{gr}}{D}\right)\right]. \tag{2.12}$$

As a characteristic parameter, the boundary layer at the solid-liquid interface with the thickness δ was introduced by the model of Burton, Prim and Schlichter [Bur53]. All incorporation-related phenomena occur within this layer. By their definition δ=δ_{BPS} is the thickness after which the solute concentration c adopts its equilibrium value of the melt $c_{l,\infty}$. Within this area the solute transport was assumed to be not influenced by convection, but only by diffusion ("stagnant film model"). The solute concentration at the solid-liquid interface can differ significantly from $c_{l,\infty}$during crystal growth. However, solute incorporation into the crystal is still governed by k_0. Therefore, the experimentally measurable effective distribution coefficient k_{eff}

was introduced:

$$k_{\text{eff}} = \frac{c_s}{c_{l,\infty}} \tag{2.13}$$

Burton, Prim and Schlichter found a fundamental relation, linking k_0, v_{gr}, D, and δ_{BPS} to k_{eff}:

$$k_{\text{eff}} = \frac{k_0}{k_0 + (1 - k_0)\exp\left(-\frac{\delta_{\text{BPS}} v_{gr}}{D}\right)} \tag{2.14}$$

It has to be noticed that δ_{BPS} cannot be interpreted as real physical thickness of the boundary layer. Here, it acts more like an adaption parameter to define diffusive and convective shares in front of the solid-liquid interface. Wilson [Wil78] defined the diffusion boundary layer thickness δ_D by

$$\delta_D = \frac{c_0 - c_{l,\infty}}{-(\frac{\partial c}{\partial z})_{z=0}}. \tag{2.15}$$

Together with equation 2.12 we get for the pure diffusive case the following expression:

$$\delta = \delta_D = \frac{D}{v_{gr}} \tag{2.16}$$

This definition has the advantage of being extendable when convection is introduced. An estimation of the value of the thickness is easier. The effective segregation coefficient k_{eff} depends on the physical thickness of the boundary layer δ, the growth rate v_{gr}, and the flow velocity along the interface u_i [Ost92]. The latter is responsible for the removal of the solutes from the progressing interface (see Fig. 2.4c). A non-dimensional convecto-diffusive parameter Δ can be defined by [Gar90]

$$\Delta = \frac{\delta}{\delta_D} = \frac{\delta v_{gr}}{D} = 1 - \exp\left(-\frac{\delta_{\text{BPS}} v_{gr}}{D}\right) \tag{2.17}$$

with $0 \leq \Delta \leq 1$. A value of 1 means pure diffusion, 0 dominating convection. Therefore, Δ quantifies the respective share of diffusion and convection on the solute transport. The effective distribution coefficient can now be written as:

$$k_{\text{eff}} = \frac{k_0}{1 - (1 - k_0)\Delta} \tag{2.18}$$

For the pure diffusive solute transport the effective distribution coefficient becomes approximately k_{eff}=1, in case of complete mixing k_{eff}=k_0. In VGF growth a preferably large area with a homogeneous dopant distribution is desired. For typical values of $k_0 \approx 0.1$, $k_{\text{eff}} \rightarrow k_0$ is therefore intended. As already been shown, this can be achieved by slow growth velocities or a reduction of the boundary layer thickness. Certainly, a reduction of v_{gr} is not desired. Hence, an enhancement of the flow velocities in the melt is preferred (see the following sections of this thesis).

For the case of pure diffusion, Tiller et al. [Til53] found the following expression for the solute concentration in the solid:

$$c_s(z) = c_0 \cdot \left[1 - (1 - k_0) \exp\left(-z \frac{k_0 \cdot v_{gr}}{D}\right)\right] \tag{2.19}$$

The qualitative behavior of c_s with progressing growth for complete mixing of the solutes in the melt was deduced by Scheil [Sch42]

$$c_s(g) = k_0 \cdot c_0 (1 - g)^{k_0 - 1} \tag{2.20}$$

where $g = z/L$ is the share of the solidified fraction of the melt with L as the total melt length. Here, the concentration gradient at the interface during solidification (for $k_0 \neq 1$) is neglected, the growth velocity is close to zero. Macrosegregation is influenced by diffusion and convection and the axial solute distribution in the solid lies between the two limiting cases of 2.19 and 2.20. A good approximation for c_s can be determined when the effective distribution coefficient is used for the calculation [Alb97]:

$$c_s(g) = k_{\text{eff}} \cdot c_0 (1 - g)^{k_{\text{eff}} - 1} \tag{2.21}$$

To describe the solute concentrations in the melt and the solid for growth processes with varying growth conditions, e.g. under consideration of solute reactions with the encapsulation material, variable growth velocities or boundary layer thicknesses, the effective distribution coefficient can considered to be varying during growth. The coefficients a and b can be introduced using experimental results [Cza98]:

$$c_s = a \cdot c_{l,\infty}^{(1-b)} \tag{2.22}$$

For $b = 0$, k_{eff} is constant and the upper equations apply, while for $b \neq 0$ the melt and solid concentrations can now be written as:

$$c_l(g) = \left[a + \frac{{c_0}^b - a}{(1 - g)^b}\right]^{\frac{1}{b}} \tag{2.23}$$

$$c_s(g) = a \cdot \left[a + \frac{{c_0}^b - a}{(1 - g)^b}\right]^{\frac{1-b}{b}} \tag{2.24}$$

These expressions allow to establish an expression for k_{eff} as a function of the solidified fraction of the melt

$$k_{\text{eff}} = a \cdot \left[a + \frac{{c_0}^b - a}{(1 - g)^b}\right]^{-1}. \tag{2.25}$$

The coefficients can be determined by non-linear fitting of the measured solute distribution in the crystal.

Radial macrosegregation

The problem of macrosegregation was solely treated as a one-dimensional problem in the previous section. Hereafter, the interface is not to be considered as planar anymore. The radial homogeneity of electronic and structural properties on a wafer is crucial for the manufacturing of devices. The main origin of radial segregation is the deflection of the interface. But also variations of growth velocities and boundary layer thicknesses along the solid-liquid interface can cause lateral inhomogeneities. Faceted growth can be another reason, but will not be discussed in detail.

Coriell et al. found a solution for the radial macrosegregation under purely diffusive conditions for a determined interface deflection [Cor79]:

$$\Delta c_{s,r} = -\frac{v}{D} c_0 (1 - k_{\text{eff}}) \Delta z \tag{2.26}$$

where $\Delta c_{s,r}$ is the maximum radial segregation in the solid and Δz is deflection of the interface. Assuming pure convection, a uniform melt composition, a constant boundary layer thickness, but a small interface curvature, the radial composition can be written as [Gar94]

$$\Delta c_{s,r} = \frac{c_0 k_{\text{eff}}}{L} (1 - k_{\text{eff}}) (1 - g)^{k_{\text{eff}} - 2} \Delta z. \tag{2.27}$$

But also in case of a flat interface, variations in the boundary layer thickness through convection can lead to radial segregation. Drevet et al. [Dre93] used the minimum and maximum of the convecto-diffusive parameter Δ_{min} and Δ_{max} along the interface to describe the maximum radial segregation Δc_M in the solid:

$$\Delta c_M = c_{s,max} - c_{s,min} = (c_i - c_{l,\infty}) \left(\frac{1}{\Delta_{min}} - \frac{1}{\Delta_{max}} \right) \tag{2.28}$$

The maximum radial composition variation scales with the difference of the melt concentration at the interface c_i and $c_{l,\infty}$ as well as with the inverse of the convecto-diffusive parameters.

Chang et al. [Cha83] analyzed the influence of natural convection in the melt and along the solid-liquid interface on radial dopant segregation for gallium-doped germanium in a VB crystal growth system. The change in solute concentration along the interface was evolving with increasing convection. It caused discrepancies in the thickness of the boundary layer δ and the effective distribution coefficient k_{eff}, which led to radial segregation. Furthermore, the melt zone height and the ratio of thermal conductivities between melt and crystal were identified as additional critical parameters for setting the degree of radial segregation. Priede and Gerbeth theoretically showed for a VB growth configuration, that converging melt flows at the solid-liquid interface caused a radial segregation profile with a concentration peak along the crystal axis [Pri05]. For a solidification front with the fixed radius R they obtained an analytic solution showing that the concentration of the solute

depends on the radius r, following $c_r \propto \ln(R/r)$ near the crystal center and with $c_r \propto \ln^{1/3}(R/r)$ near the crucible wall.

Microsegregation

Microscopic segregation of impurities is a well known problem in crystal growth. The undesired noticeable localized fluctuations in composition are called striations. They are caused by a time-dependent modulation of the growth rate due to temperature fluctuations and an unsteady convective flow [Jun97]. They are often characterized by random distances and intensities and they can be found in a broad range of growing techniques and materials. Their cause can be growth setup related, like striations through minor back-melting at the solid-liquid interface because of rotation and/or vibration (e.g. in Czochralski growth) and heater controller variations (VGF growth), or generated by unsteady convection conditions with varying diffusion boundary layer thicknesses. A qualitative investigation of striations can provide useful information about the form of the solid-liquid interface during growth.

Carlson and Witt used high resolution NIR transmission microscopy for a quantitative analysis of striation spacings and microscopic composition uniformity in 3"-LEC-GaAs:Si [Car91]. In a cut parallel to the growth axis they found striations generated by turbulent flow with widths between 2-20 µm with locally decreasing carrier concentrations of about one order of magnitude. These large variations become even more vital when the conventional wafer geometry is considered. A slightly deflected interface generates circular dopant fluctuations on a wafer. The quality of epitaxial layers in (opto-)electronic devices can be markedly reduced with an inhomogeneous composition of the substrates.

2.1.3 Properties and real structure of undoped and doped VGF-GaAs crystals

Point defects like vacancies, interstitials, anti-site defects, and impurity atoms can have a positive or negative influence on the electrical and structural properties on the grown GaAs crystals. Their presence can be influenced during growth by additional doping, post-growth annealing steps and the adjustment of the partial pressure of the volatile As component. Fig. 2.5 shows the phase diagram of the binary system Ga-As and an enlarged section of the solid GaAs with the congruent melting point at 1238°C lying slightly on the As-rich side. Hence, stoichiometric GaAs crystallizes from a Ga-rich melt. However, excess Ga can form droplets which can destroy the morphological stability of the interface. Therefore, GaAs is grown with a slight As-excess [Rud99]. Additionally, to achieve semi-insulating (SI) behavior, which means a high electrical resistivity of $\rho > 10^7$ Ωcm, GaAs has to be grown from As-rich melts. The reason for this is the intrinsic midgap double donor EL2. The As anti-site defect As_{Ga} is known to be the source of the EL2 defect in GaAs [vB86]. The requirements for semi-insulating behavior can be described following the compensation model of

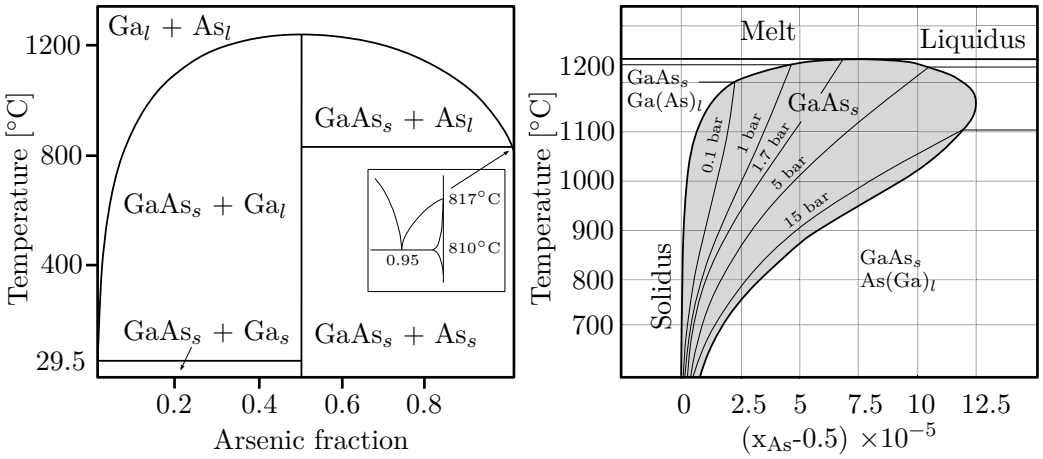

Figure 2.5: Phase diagram of the binary system Ga-As and an enlarged section of the solid GaAs at the congruent melting point, after [Wun06]

Martin et al. [Mar80]:

$$N_{\mathrm{EL2}} > N_{\mathrm{A}} - N_{\mathrm{D}} > 0 \tag{2.29}$$

The concentration of the deep donor N_{EL2} has to exceed the difference of shallow acceptors N_{A} and donors N_{D}. With a constant EL2 concentration of usually about $\sim 10^{15}$-10^{16} cm^{-3}, depending if the crystals are as-grown or annealed after growth, the control of the carbon concentration during growth is of great importance to guarantee semi-insulating behavior along the whole crystal [Bue06]. The shallow acceptor C_{As} is added with a usual intended concentration around $\sim 10^{15}$ cm^{-3} to compensate the residual impurities with concentrations below $\sim 10^{14}$ cm^{-3}. Semiconducting n-type VGF-GaAs is mainly produced by adding silicon to the melt, with an intended concentration around 10^{18} cm^{-3} [Eic08a]. The initial dopant concentration in the melt has to exceed this concentration in the crystal by about one order of magnitude due to the small distribution coefficient of Si in GaAs of k_0=0.023 ([Chm90] in [Wun06]) and k_{eff}=0.15 for VGF-GaAs with B_2O_3 melt cover [Bir02]. Silicon shows amphoteric behavior. While at first charge carrier concentration increases linearly with the Si concentration, Si on Ga sites act as shallow donors Si_{Ga}, at higher Si concentrations of about 5×10^{18} cm^{-3} Si is also occupying As lattice sites acting as shallow acceptor Si_{As} [New94]. Compensation of the charge carriers takes place, leading to a saturation of the charge carrier concentration.

The interaction of the B_2O_3 encapsulation with dopants and melt during VGF-GaAs growth has significant influence on dopant concentrations in the crystals. The liquid melt cover not only helps to maintain melt stochiometry together with a

counter pressure, also reactions occur, e.g. of B_2O_3 with Si [Wun06]

$$3\ Si + 2\ B_2O_3 \rightleftharpoons 3\ SiO_2 + 4\ B \tag{2.30}$$

$$3\ Si + B_2O_3 \rightleftharpoons 3\ SiO + 2\ B \tag{2.31}$$

leading to a reduction of the available Si and to the enhancement of B in the melt. Boron is mainly incorporated in GaAs as isoelectronic defect B_{Ga}. The boron antisite B_{As} defect is only observed for a very high boron content $>10^{18}$ cm^{-3} related to Ga-rich growth conditions [Alt91]. The water content of the B_2O_3 has also a large influence on the reactions of melt and encapsulation. Bourret et al. [Bou91] showed that C and B incorporation into the crystals with the utilization of wet (1200ppm H_2O) B_2O_3 is enhanced compared to dry (400ppm H_2O) B_2O_3. In literature, experimentally determined values of the distribution coefficient of B and C are varying. Depending on growth conditions, methods of measurement, and water content of the B_2O_3 values between k_C=1.15-2.6 and k_B=0.4-2.1 were reported [Sat90, Nis93, Fra95, Kor99].

A dislocation is a one-dimensional defect in the crystal structure. These crystal disturbances are highly undesired for any applications. Their reduction is one of the main objectives in VGF growth. The dislocation density characterizes the structural perfection of a crystal. Since dislocations are often detected by chemical etching of polished surface, the dislocation density is often referred to as etch pit density (EPD). Dislocations are generated through plastic deformation when subjected to thermal and mechanical stress [Ind79] and the elastic limit of the crystal is exceeded. Other sources of dislocations are: growing-in of dislocations from the seed or a foreign particle, dislocations through misfits from grain boundaries, inclusions etc., and condensation of point defects [Wil88]. The two different primary types are screw and edge dislocations. The interaction with impurity atoms is driven by the strain field around dislocations, leading to a preferred agglomeration of impurities around them, the so called Cottrell atmosphere. Grown-in dislocations are connected with the solid-liquid interface. Post-growth dislocations are generated behind the interface. Either during growth shortly behind the growth front or during cooling down to room temperature [Kla00]. Dislocations can move within their specific glide planes, which are spanned by the dislocation line and the Burgers vector $\vec{b}$. In the GaAs zinc blende structure $\vec{b}=\frac{1}{2}<110>$ [Hor58]. Glide plane and glide direction form a glide system. Dislocations can also climb out of their glide plane through accumulation and deposition of point defects. Cross-slip to another glide plane is possible for screw dislocations.

It is known that Si-doping (in connection with and without B_2O_3 encapsulation) can significantly reduce EPD values in GaAs crystals. Silicon incorporation, formation of complexes and B incorporation together seem responsible for this reduction. Si-doping has an impact on intrinsic point defect concentration. When a critical limit of Si concentration $>10^{18}$ cm^{-3} is exceeded, arsenic interstitials As_i are reduced and therefore nucleation sites of dislocations are eliminated [Gil86]. EPD

values also decrease with increasing acceptor concentrations of Si_{Ga}-V_{Ga} [Mo83]. Further, EPD values of VGF-GaAs:Si crystals grown without B_2O_3 encapsulation are comparatively higher [Han99], therefore B-related mechanisms also influence the dislocation reduction. The so called lattice hardening effect is claimed to be responsible for the reduction of dislocation generation with incorporation of dopants. This effect is attributed to the strength of the bonds formed between impurity atoms and surrounding host crystal atoms [Sek78]. The stronger lattice contraction in liquid-encapsulated VGF-GaAs:Si compared to SI GaAs is a result of the with Si-doping accompanied incorporation of B_{Ga} in the range of 10^{18} cm^{-3} [Bas97] (see equations 2.30 and 2.31).

Usually the most important types of dislocation in Si-doped GaAs with dislocation densities >200 cm^{-2} are thermal stress-induced glide dislocations. They lie in the $\{111\}\frac{1}{2}<110>$ glide system with an angle of 60° between line vector $\vec{l}=<110>$ and $\vec{b}$. For crystals with very low dislocation densities, obtained residual dislocations are mainly induced by the seed crystal, not by thermal stress, e.g. grown-in dislocations coming from the seed with line vectors parallel to the [001] growth direction [Amo99]. A cross-shaped arrangement of dislocations belonging to the $(010)\frac{1}{2}[101]$ or $(010)\frac{1}{2}[\bar{1}01]$ glide system [Bir05] is often observed on low EPD GaAs:Si wafers in [100] and [010] direction [Han99]. Furthermore, on such wafers an increase of the dislocation density in the wafer center can be seen. This is caused by dislocation walls growing through the whole crystal extending in [110] and $[1\bar{1}0]$ directions [Bir05]. They are formed by edge dislocations belonging to the $(110)\frac{1}{2}[\bar{1}10]$ or $(\bar{1}10)\frac{1}{2}[110]$ glide system.

Dislocation densities of VGF SI GaAs lie around one order of magnitude higher compared to VGF-GaAs:Si [Eic08a]. Here, dislocations are patterned in a cellular network of globular shape. Rudolph et al. described their generation process as a combination of the formation of dislocation networks by dynamical polygonization due to thermo-elastic stress in the growing crystals (previously disordered dislocations rearranging to an energetically favorable position to each other) and cell patterning by dissipative structuring (ordering, i.e. reduction of entropy) [Rud04, Rud07]. Laser scattering tomography (LST) measurements revealed that cellular structure already exist at high temperatures between 800-1100°C [Nau01]. The size of the cell networks is dependent on the dislocation density. With EPD <1000 cm^{-2} cell diameter is about 1-2 mm, at densities in the order of 10^5 cm^{-2} the diameter is <500 µm [Hur04]. Most dislocations are concentrated in the cell walls, while the inner area is almost dislocation free. The formation of dislocation bundles, consisting of closely arranged parallel dislocations, was described by numerous authors independent from the applied GaAs growth method [Tow91, Shi93, Rud04]. Their generation can be originated from inclusions like Ga droplets or accumulation of stress-induced dislocations through distinct interface concavities and concave-to-convex transition regions.

The occurrence of facets has an important influence on the real structure of VGF-GaAs. The form of the solid-liquid interface with respect to the crucible wall has

to extend a certain angle to reach faceting. There can be a coincidence between atomistically kinked and atomistically flat interfaces with a large interface deflection or in the cone area of the crucible. Growth on the kinked surface is continuous and occurs at very small supercooling $\Delta T \ll 1$ K. Growth on a flat surface requires the formation of a 2D supercritical nucleus with several degrees of supercooling [Mue12]. If in the crystal periphery the growth front falls behind the melt isothermal line, layer-by-layer facet growth occurs. Incorporation of dopants is higher in the facets compared to growth on a rough interface. Crystals grown in [001] direction have {111}As facets that are larger than {111}Ga facets [Amo98] due to the larger supercooling required for forming a 2D nucleus for layer growth on an As plane compared to Ga plane GaAs.

Most important two-dimensional defects in in GaAs are the crystal surface, twins, and grain boundaries. Their formation is affected by the accumulation of point defects, dislocations, and polycrystalline growth. Grain boundaries can be differentiated into small and large angle grain boundaries. The former have only a small misorientation and are composed of dislocations, the latter have misoriented angles of more than 10°. Twins are generated when lattice planes are tilted by about 60° about a <111> axis, while the lattice structure itself is not disturbed. Their formation has been correlated to by the temperature field near the solid-liquid interface, the interface energy of the material, melt stoichiometry, the cone angle of the crystal, dopant concentration, heat-flux scattering, and the occurrence of large irregular facets [Koh95, Amo98, Hur04, Mar08]. The theory of Hurle states that for a large supercooling on {111} facets a misoriented nucleus forms with twin orientation for energetic and geometrical reasons [Hur95]. The tendency towards twinning was shown to be avoided by reducing the length of facets in LEC growth [Tow91], by keeping the length uniform, and through increasing the cone angle of the crucible in VGF growth [Amo98].

Three-dimensional microscopic and macroscopic distribution inhomogeneities, inclusions, voids, and precipitates also affect crystal and device quality. Often occurring are non-stoichiometry related As precipitates formed in the grown crystal during the cooling down process by point defect agglomeration. For example, As precipitates decorate dislocation cells in SI GaAs or are distributed in the crystal matrix [Nau01]. The size distribution between as-grown and annealed GaAs crystals significantly differs [Sch92].

2.2 External force fields in VGF crystal growth

Convection in a conventional Bridgman/VGF configuration is driven by differences in buoyancy force, which are induced by radial temperature gradients in the melt. With large melt diameters the magnitude of the gradients in the melt rises and the convective flow changes from laminar to time-periodic. Temperature fluctuations at the solid-liquid interface occur - undesired striations are generated. Furthermore,

unfavorable melt convection can cause high deflections of the interface, leading to high dislocation densities. All these obstacles have to be avoided.

The use of external force fields during crystal growth is an effective method to damp and control undesirable convection and to create desirable convection. Additionally, controlled convection enhancement improves melt mixing for a homogeneous distribution of dopants in the melt and reduces the risk of constitutional supercooling. A positive effect on the melt flow has been shown for different mechanical, electrical, and magnetical steady and non-steady force fields.

There is a large variety of force fields, which have been applied during Bridgman/VGF crystal growth, some even simultaneously. Mechanical methods were, for example, the application of ultrasound or low-frequency vibrations to reduce the thickness of the diffusion boundary layer [Ubb12]. Radial direct electric current was utilized to stir the melt and control the species distribution in semiconductor crystals [Wan06]. Axial time-dependent electric currents were successfully used to mark the solid-liquid interface utilizing the Peltier effect [Bly97]. Of course, the focus of this work was put in the application of (traveling) magnetic fields during crystal growth, which in the following shall be discussed in detail. A complete overview about growth from the melt under external force fields, including their application for a large number of different growth techniques and materials, is given by the review of Rudolph and Kakimoto [Rud09b].

A moving melt with an electrical conductivity σ is subjected to Lorentz forces when situated within a steady magnetic field. Following Lenz's law the force is so directed as to oppose the motion. The effective melt viscosity is being artificially enhanced and convective turbulence can be damped. The micro-homogeneity of the dopant distribution in the crystal can be improved [Hur94]. Typical steady magnetic fields used for crystal growth of various materials with different methods are axial, horizontal, and cusp fields [Rud08a]. The latter is formed with magnetic coils with different field directions.

The application of non-steady magnetic fields offers several advantages. While steady magnetic fields are used to damp the flow, non-steady magnetic fields induce melt motion themselves. They provide a permanent control of the melt flow. Compared to steady magnetic fields, with non-steady magnetic fields much lower magnetic flux densities are necessary to counteract natural convection. But their penetration depth is limited (see section 2.2.2). A controlled enhancement and adjustment of convection can be used for improving the melt mixing, stabilization of the heat and mass transport, or even for a specific modification of solute segregation and the shape of the solid-liquid interface. Figure 2.6 shows the arrangement of the magnetic coils for the generation of the different types of non-steady magnetic fields.

Alternating magnetic fields (AMF) are generated by vertically aligned electromagnetic coils around the melt container. Here, they are simultaneously fed by an alternating current with no phase shift. They were successfully applied in VB growth of GaInSb alloys for the enhancement of melt mixing and stabilization of the radial segregation profile along the grown crystal [Mit06]. But numerical investiga-

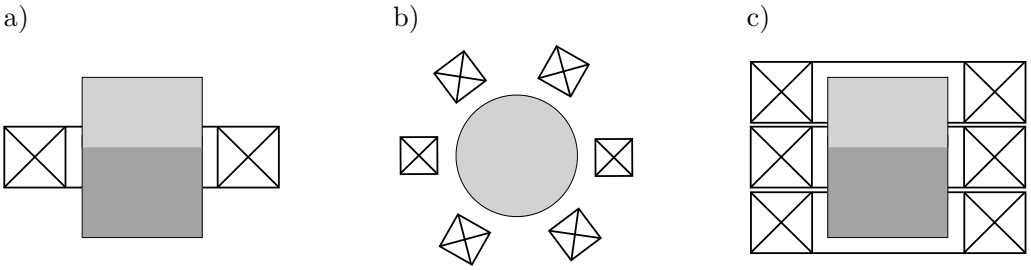

Figure 2.6: Sketch of the arrangement of the magnetic coils for the generation of various types of non-steady magnetic fields with an input of alternating currents: a) Alternating magnetic fields, b) Rotating magnetic fields, c) Traveling magnetic fields

tions for the VB growth of GaAs revealed decreasing flow velocities and increasing radial segregation with increasing magnetic field strengths [Lyu04]. Other types of non-steady magnetic fields like rotating or traveling magnetic fields showed also a better stirring efficiency [Dro13b].

Rotating magnetic fields (RMF) are generated by several pairs of electromagnetic coils, which are horizontally aligned around the melt. The coils are fed by a phase-shifted alternating current and the transverse magnetic field is rotating with a determined angular frequency. A melt flow with a stronger azimuthal and in comparison somewhat weaker meridional components is induced [Pae13], which helps to reduce temperature fluctuations in the melt and improves mass transport [Dol99]. The meridional flow influences the shape of the solid-liquid interface. Pätzold et al. showed a decreasing curvature of the nominally concave interface or even a w-shape of the interface with an applied RMF for 2" VGF-GaAs [Pae02b, Pae04]. Within the work of Wunderwald [Wun06] the bending of the interface of 2" VGF-GaAs was reduced about 20% compared to the growth without a RMF with the same experimental setup through decreasing radial temperature gradients near the growth front. The influence of the RMF on solute transport and segregation was studied in the model system VGF-Ge:Ga with crystal diameters of 15 mm. The forced RMF convection led to a reduction of the axial charge carrier density of up to 22%. The thickness of the boundary layer decreased. Furthermore, radial macrosegregation was reduced through enhancement of the meridional flow. Bellmann et al. found for VGF-Ge:Ga with crystal diameters of 6 mm grown with RMF, that the effective distribution coefficient k_{eff} approached k_0 for early stages of the growth [Bel04]. Numerical investigations showed that at high magnetic field intensities the induced steady-state flow became unstable and unsteady flow was observed [Lyu04].

2.2.1 Traveling magnetic fields

Traveling magnetic fields (TMF) are generated by vertically stacked electromagnetic coils (see Fig. 2.6c). An upward or downward traveling Lorentz force field is induced

in the semiconductor melt, when they are supplied with an alternating current with a phase shift (see the following section for a detailed derivation). The melt flow results from superposition of Lorentz force field and the buoyant forces. Depending on the direction of the force field it creates a mostly axisymmetric meridional flow [Pae13], which can counteract or amplify natural convective flow near the solid-liquid interface (see Fig. 2.7 and compare it to Fig. 2.2). One has to consider, that the depicted flow field is only valid for symmetrical thermal boundary conditions and linear axial thermal gradients. The shape of the growth front is determined by the altered vertical heat flux in the melt. Hence, traveling magnetic fields may be superior compared to other non-steady magnetic fields to influence the shape of the interface.

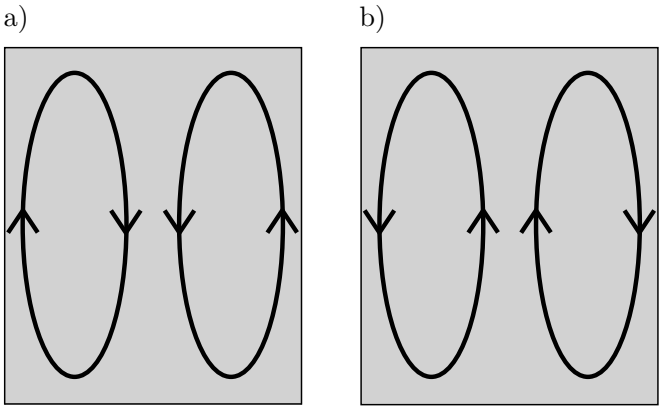

Figure 2.7: Sketch of the flow field created by a) an upward-directed TMF and b) a downward-directed TMF when the influence of the buoyancy is neglected and the thermal boundary conditions are symmetrical, after [Lan09]

With increasing magnetic field strength ($F_L >> F_{\mathrm{buo}}$) the natural buoyant flow is superimposed by the meridional single vortex flow induced by the TMF [Nie11]. An upward-directed TMF creates a Lorentz force oriented upwards at the edge of the melt near the crucible. The deflection of the solid-liquid interface increases with increasing magnetic induction, thermal stress in the crystal rises. A downward-directed TMF creates a Lorentz force oriented downwards at the edge of the melt, which can decrease the interface bending and thermal stress [Sch04b]. With a flattened interface radial dopant segregation decreases [Lyu04], too. Furthermore, the flow towards the interface is intensified with a downward-directed TMF.

Numerical studies predicted a large influence of the direction of the flow near the interface on radial macrosegregation [Gra08]. In the case of pure buoyancy the radial thermal gradients over a concave interface caused a converging flow and a solute concentration peak along the inner crystal axis [Pri07]. While downward-directed TMF can potentially increase this effect, with upward-directed TMF the flow along the interface can be reversed and the concentration peak removed.

But the application of a TMF can also disturb crystal growth. If the Lorentz force exceeds a critical value, the convection causes significant asymmetries of the velocity and temperature field in the melt. Grants et al. numerically approximated the instabilities to occur when the dimensionless TMF forcing parameter reached the magnitude of the Grashof number (ratio of the buoyancy to viscous force acting on the melt) [Gra09]. The flow changed from laminar to unsteady. The flow velocities can oscillate or even randomly fluctuate, undesired striations were generated. Cramer et al. [Cra11] investigated the influence of TMF driven flow with respect to tiltings and shifts between the axis of the melt container and the induced magnetic field. They performed numerical simulations and model experiments using GaInSn and ultrasound Doppler velocimetry. They showed that even a small shift of the crucible diameter might eliminate the meridional vortex structure.

Experimental results on growth of GaAs with a utilized TMF are given in the thesis of Lantzsch [Lan09]. A TMF and a combined TMF/DC field, created with an external coil system, was used to influence heat and mass transport during VGF crystal growth. Silicon-doped 3"-GaAs was grown with axial thermal gradients between 3-6 K/cm, with a growth rate 2-3 mm/h and with magnetic flux densities of up to B_{TMF}=3.5 mT and B_{DC}=84 mT. The average concave deflection of the solid-liquid interface $\Delta z/R$ could be reduced from 17% to 13% with a downward directed TMF compared to GaAs:Si grown without a magnetic field. A combined TMF/DC field showed similar or even slightly smaller deflections. The associated reduction of the thermal stress did not result in a significant reduction of the EPD, because even the crystals without magnetic field showed very low values below 200 cm^{-2}. Axial macrosegregation was following Scheil's law for complete mixing with and without magnetic field application. Radial macrosegregation was small in both cases, no concentration peak along the axis was observed. The crystals grown without a magnetic field showed weak microsegregation. Upward- and downward-directed TMF even amplified the generation of the undesired striations. In both cases the melt flow is unsteady. The development of micro-inhomogeneities could be suppressed by the application of a strong DC field of 77 mT.

2.2.2 The KRIST$\widetilde{MAG}$® technology and the heater-magnet module

All the so far described results of the VGF growth utilizing a TMF have been realized with external magnetic coils outside the growth chamber (see Fig. 2.8a). However, such a setup is unfavorable when it comes to an efficient and effective generation of Lorentz force density within the melt. The steel pressure vessel, the insulation, and the side heaters are situated between melt container and the magnetic coils. Due to the skin effect and the large distance, a much higher field than necessary for convection control has to be generated to compensate the losses. Only about 10% of the original flow density will reach the melt [Rud08a]. The rest is lost, which makes the application of non-steady magnetic fields very energy consuming and therefore expensive. This uneconomic disadvantage must be approached when an adaption in industrial VGF growth is aspired.

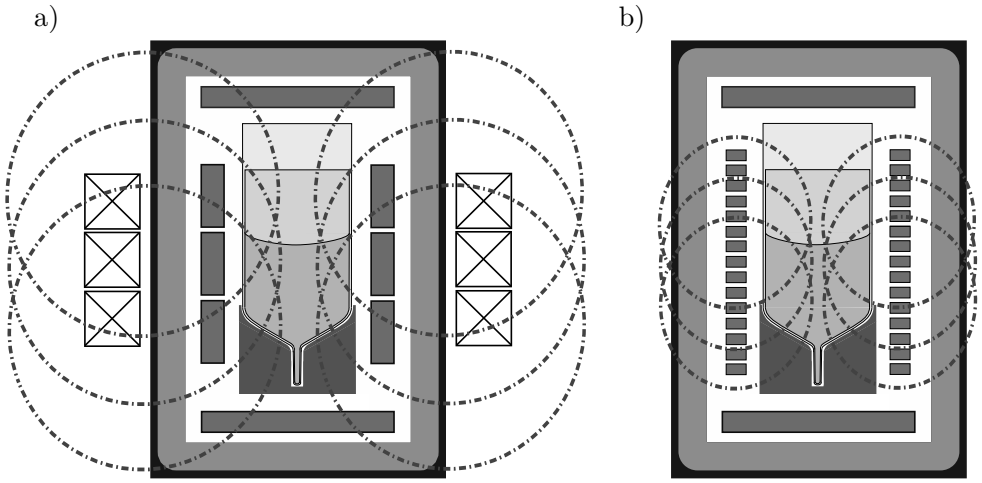

Figure 2.8: Comparison of a) a conventional VGF configuration with additional external coils for the generation of a TMF and a b) VGF setup equipped with a heater-magnet module: The basic structure of the original VGF setup remains, but side heating and TMF are now simultaneously generated

Certainly, metal inductors are not suitable to be placed inside a VGF growth vessel. Therefore, a heater adjustment seems most promising. In a patent of 1970, Fujimori and Ayusawa first described the combination of heater and magnetic coil [Fuj70]. A vertical meander-type graphite heater was fed by a three-phase alternating current. Heating and a RMF, through the phase shift between the three delta-connected heater segments around the melt, were simultaneously supplied. First experimental results with such a setup were shown by Hoshikawa et al. for Czochralski silicon growth with enhanced fluid rotation and an improvement of the oxygen control inside the crystals caused by the RMF [Hos80]. Nevertheless, this growth configuration has major disadvantages. First, the current for the RMF generation is coupled to required heater power, which prevents adjustments in the magnetic field strengths. Second, the RMF efficiency is small, because in the meander-type structure the Lorentz force of opposing current flows neutralizes each other.

Based on the same principle, Mühe et al. [Mue03] presented a heater-magnet setup for combined heating and the generation of a TMF. Three coupled vertically stacked graphite coils are supplied by a three-phase alternating current with a phase shift of 120°. A longitudinal traveling magnetic field is created. However, with the described configuration, it is not possible to choose the phase shift freely. Additionally, the coils are fed by a direct current, which is responsible for the power necessary for heating. But the coils are also coupled, which prevents the independent adjustment of various heater powers for each coil to create the desired thermal gradient field.

Since the start of the KRIST$\widetilde{MAG}$® project (2005-2008) at the Leibniz Institute of Crystal Growth Berlin the idea of combined side heater-magnet has been further

developed (see also [Rud08a] for details). Numerous patents describe improvements of the concept [Zie07, Lan07a, FR07, Bue08, Lan12]. It led to the design of the so called heater-magnet module (HMM). The aim of the development included the possibility to easily upgrade existing conventional VGF, LEC, VCz and DS growth setups. The heater-magnet module is supplied by a newly developed power unit and control system containing an integrated intelligent power system (SKiiP). Hence, at the same time, the graphite coils are fed with direct and alternating currents independent from one another, for the simultaneous generation of heat and traveling magnetic field. The configuration of the additional resistive heaters remains unaffected. An arbitrary phase shift of the alternating current can be set between the coils, amplitude and frequency are individually adjustable. Control of the direct current for each coil allows to adjust desired thermal gradients in the melt. It also leads to the generation of three DC-coupled steady magnetic fields, too. But these fields are very weak and significantly less effective than the TMF. Therefore, their impact can be neglected. The KRIST$\widetilde{MAG}$® concept is also applicable for the generation of other magnetic fields. Bottom heater magnets can induce Carousel magnetic fields (CMF) for effective melt mixing during directional solidification of large silicon ingots for photovoltaics with masses of 700 kg [Dro12b]. For the VGF configuration, the heater-magnet module consists of three vertically stacked star-connected graphite coils, with an integer number of spirally arranged windings, respectively (see Fig. 2.8b). Cross-section, height, and widths of the windings are adapted for optimal stability and resistivity.

Generation of a TMF in a heater-magnet module

Figure 2.9 shows the geometry of the vertically arranged side heaters/magnetic coils in the heater-magnet module which induce the traveling magnetic field. Each of the three side heaters (H2-H4) has an even number of windings N with a height h, an inner diameter D_{in} and an outer diameter D_{out}. With the application of an alternating current with a phase shift ϕ between neighboring coils, an upward or downward directed Lorentz force field will be induced. The phase angle of the current determines the direction of the current flow inside each coil and therefore also the direction of the traveling Lorentz field. Currents up to I=330 A and frequencies in the range of f=10-600 Hz are possible in the heater-magnet module. The phase shift can be set from 0-120°. All parameters in every coil can be set independently from another. This results in a broad range of possible adjustments for different process conditions. The induced axisymmetric traveling magnetic field $\vec{B}$ can be described as a continuous wave and consists of a radial and an axial component with a phase shift of $\pi/2$ [Lan09], using cylindrical coordinates (r, φ, z):

$$\vec{B} = B_z\vec{e}_z + B_r\vec{e}_r \tag{2.32}$$

$$= B_0 \cdot \left(\vec{e}_z \sin(\omega t - kz) - \vec{e}_r \frac{rk}{2} \cos(\omega t - kz)\right) \tag{2.33}$$

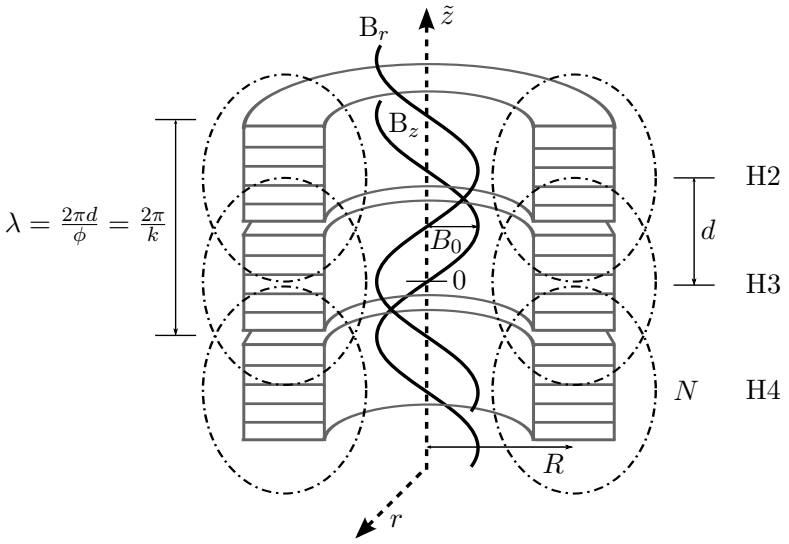

Figure 2.9: Cross section of the heater-magnet module with the three axially arranged heater coils H2-H4, $\tilde{z}$=0 defines the center of the radial symmetric setup, the magnetic induction with axial and radial components B_z and B_r can be described as a continuous wave

The wavelength λ of the traveling magnetic field can be derived with the coil distance d and the respective phase shift of the alternating current between the coils:

$$\lambda = \frac{2\pi d}{\phi} = \frac{2\pi}{k} \tag{2.34}$$

The amplitude B_0 of the field shall serve as a characteristic value of strength of the TMF. It can be approximated using the average radius R, the distance d between two adjacent heather coils, the number of windings N, and their respective phase shift ϕ. With the superposition of each coil component $\tilde{B}$ the magnetic flux density along the inner axis can be derived (see also [Lan07b]):

$$B(\tilde{z}, r = 0) = B_z(\tilde{z}) = \left| \sum_{n=1}^{3} \tilde{B}(\tilde{z} + d(n-2)) e^{\mathrm{i}(n-1)\phi} \right| \tag{2.35}$$

$$= \left| \tilde{B}(\tilde{z} - d) + \tilde{B}(\tilde{z}) e^{\mathrm{i}\phi} + \tilde{B}(\tilde{z} + d) e^{2\mathrm{i}\phi} \right| \tag{2.36}$$

The magnitude of the magnetic field strength of a current-carrying circular conductor loop can be specified using the Biot-Savart law on the symmetry axis perpendicular to the closed conductor loop. When N windings in each coil with the current I lay

close to each other, the total field is obtained by multiplication with N

$$\tilde{B}(\tilde{z}) = N \cdot I \cdot \frac{\mu_0}{2} \cdot \frac{R^2}{(R^2 + \tilde{z}^2)^{\frac{3}{2}}} \tag{2.37}$$

where μ_0 is the permeability of the free space. Combining equations 2.36 and 2.37 the amplitude of the magnetic flux density B_0 in the center of the heater-magnet module $(r, \tilde{z} = 0)$ can now be written as:

$$B_0 = B_z(\tilde{z} = 0) = N \cdot I \cdot \frac{\mu_0}{2R} \cdot \left| \frac{R^3}{(R^2 + d^2)^{\frac{3}{2}}} + e^{\mathrm{i}\phi} + \frac{R^3}{(R^2 + d^2)^{\frac{3}{2}}} e^{2\mathrm{i}\phi} \right| \tag{2.38}$$

The generated temporal changing magnetic field penetrates through the melt and creates opposing eddy currents. The so called skin effect evokes an exponentially decreasing current density from the surface. With increasing frequencies, the penetration depth is limited to

$$\delta = \sqrt{\frac{2}{\mu \cdot \sigma \cdot \omega}} \tag{2.39}$$

where σ is the electrical conductivity and μ absolute magnetic permeability of the melt. Following the model of Grants and Gerbeth [Gra04] the subsequent assumptions are made to analytically determine the induced Lorentz force into the melt. The wavelength of the TMF with typical parameters is much larger than the melt radius $\lambda \gg R_{melt}$ and induced currents in the melt can be neglected assuming that the frequencies are low. In this case, the penetration depth is assumed to be high. Furthermore the flow velocity of the melt $\vec{u}_{melt}$ is supposed to be smaller than the velocity of the traveling field $\vec{v} \gg \vec{u}_{melt}$. Faraday's law of induction

$$\vec{\nabla} \times \vec{E} = -\frac{\partial \vec{B}}{\partial t} \tag{2.40}$$

states that a time varying magnetic flux induces an electric field $\vec{E}$. Due to the fact that $\vec{B}$ has only an axial and radial component, the electric field has only a component in azimuthal direction:

$$\vec{E} = E \cdot \vec{e}_\varphi \tag{2.41}$$

After Ohm's law the electric field induces a current with the current density $\vec{j}$ which has also only a component in azimuthal direction:

$$\vec{j} = \sigma \vec{E} = B_0 \cdot \frac{r\omega\sigma}{2} \cos(\omega t - kz) \cdot \vec{e}_\varphi \tag{2.42}$$

From the induced current and the magnetic field with its perpendicular components the Lorentz force density $\vec{F}_L$ can be derived:

$$\vec{F}_L = \vec{j} \times \vec{B} \tag{2.43}$$

$$= \begin{pmatrix} B_0^2 \cdot \frac{r\omega\sigma}{2} \cdot \cos(\omega t - kz) \cdot \sin(\omega t - kz) \\ 0 \\ B_0^2 \cdot \frac{r\omega\sigma}{2} \cdot \cos^2(\omega t - kz) \end{pmatrix} \tag{2.44}$$

Averaging over one oscillation period through integration results in a Lorentz force density with only a component in z-direction:

$$\vec{F}_L = F_z \cdot \vec{e}_z = B_0^2 \cdot \frac{r^2\omega\sigma k}{8} \cdot \vec{e}_z \tag{2.45}$$

The TMF-induced Lorentz force is mainly upwards- or downwards-directed and decreases radially from the edge of the melt towards the center. In small crucibles with symmetrical boundary conditions, the melt flow can be described by two axisymmetric meridonal vortices with flow direction upwards or downwards near the crucible, respectively. The simplified flow structure is depicted in Fig. 2.7. With larger melt diameters and small asymmetries the vortices are more toroidal.

The force acting on the melt is proportional to the TMF frequency, and to the current and characteristic amplitude of the magnetic field to the power of two, respectively:

$$F_L \sim B_0^2 \cdot \omega \sim I^2 \cdot \omega \tag{2.46}$$

Variation of the current changes the magnitude of the Lorentz force. The phase shift can change not only the magnitude of the force but also their distribution and direction in the melt, e.g. with 120° the generated force is about half of the maximum at around 60°. An alteration of the TMF frequency changes magnitude, penetration depth, spatial distribution, and direction of the Lorentz forces and is therefore the TMF parameter with the main potential for changing of the convective flow.

A combination of various TMF parameters can provide Lorentz force fields with magnetic similarity. The strengths of the used magnetic fields can be quantified using the dimensionless magnetic Taylor number Ta_m with its definition for TMF (given in [FR09]):

$$\mathrm{Ta}_m = \frac{\sigma\pi f R_{melt}^3}{\rho\nu^2 k} B_0^2 \tag{2.47}$$

A comparability of the TMF influence on the melt convection for different parameters is given with this number.

A further advantage of the KRIST$\widetilde{MAG}$® heater-magnet module is that two alternating currents with different frequencies can be superimposed. Each one can have its own phase shift and magnitude. The lower frequency can penetrate deeper into the melt and therefore the force action is distributed in the whole melt con-

tainer. The higher frequency has a reduced penetration depth (see equation 2.39). It induces a force that mainly acts near the crucible walls. Both forces F_{L_1} and F_{L_2} add up. Hence, all of the TMF parameters have to be carefully adjusted to achieve optimal flow conditions and a flat or slightly convex interface shape. Especially the exact control of the flow near the crucible wall is of essential significance, due to the enhanced concave deflection of the solid-liquid interface in particular in this area.

In summary, compared to conventional growth configurations with external coils and previously developed combined heater-magnets, the heater-magnet module offers several advantages. The generation of heat and traveling magnetic fields is very energy efficient and no trade-off between optimal thermal properties and optimal magnetic field properties has to be made. A large variety of variable magnetic field parameters helps to find ideal conditions for convection control, including the freely selectable phase shift. Furthermore, the heater-magnet module can be simultaneously supplied with two different alternating currents with its separate phase shifts, frequencies and amplitudes. Two traveling magnetic fields with different properties develop and interfere with each other.

Previous growth results in the heater-magnet module

The effects of a TMF generated in a heater-magnet module on melt convection were numerically and experimentally studied for various growth systems. In VCz growth experiments with 3"-GaAs a reduced microsegregation and an enhanced radial distribution homogeneity of the dislocation density was detected [Rud08b]. 3"-GaAs crystals were grown with an industrial LEC puller equipped with an internal heater-magnet module [Rud09a], too. The HMM was constructed in a multi-coil design, consisting of three side and two bottom heater-magnets. Compared to crystals grown without an applied magnetic field with well-pronounced irregular striation patterns, with a high frequency TMF only weak residual striations with homogeneous periodicity were observed. Microinhomogeneities did not disappear with low TMF frequencies. There was a slight reduction of the peripheral deflection and a lowering of the dislocation density with a decrease of thermal stress. The incorporation of boron and oxygen from the encapsulant was increased through the TMF-induced enhanced flow velocities towards the melt.

Numerical studies on the application of upwards and downwards directed TMF during the unidirectional solidification of multi-crystalline silicon for photovoltaics showed promising results for enhancement of melt mixing [Dro10]. High flow velocities near the crucible rim can be suppressed by two opposite directed traveling fields with carefully selected parameter sets [Dro11]. Through superposition of the Lorentz force densities the velocities within the central region increases, which is beneficial for melt mixing and process purity. Recently, 640 kg multi-crystalline silicon ingots were successfully grown in a G5 crystallizer equipped with an heater-magnet module [Kud13]. They showed superior properties compared to material grown without a TMF. The morphology of the solid-liquid interface was controlled and stabilized. Incorporation of SiC and Si_3N_4 precipitates was suppressed through improved melt

mixing during the crystallization, no distinct interaction between melt and container was observed.

A heater-magnet module was also used in VGF growth processes. 4"-Germanium single crystals have been grown under the influence of a single downward-directed TMF [FR09]. Before, the interaction between induced Lorentz forces and the buoyancy-driven convection was numerically studied [FR08]. Results were supported by dummy measurements of the Lorentz force densities along the length of the HMM. Consequently, the frequency, amplitude, and phase shift of the TMF was optimized for best possible interface morphologies. Most suitable frequencies were f=20-50 Hz, in case of laminar flow the magnetic flux density was about B_0=2.5 mT. The TMF parameters have been adjusted during growth to ensure a constant shape of the solid-liquid interface with increasing solidified fraction. Without a TMF and with weak magnetic fields the interface shape was concave and weak striations were observed. Strong fields induced an unfavorable w-shape, overcritical TMF conditions gave rise to strong microinhomogeneities. Adjusted magnetic fields led to nearly optimized flat/slightly convex interface shapes. Here, nearly no striations were found, temperature fluctuations were damped. By comparison, in these crystals a somewhat lower EPD was observed and the radial homogeneity of the electrical parameters has been improved. Optimized double-frequency TMF were also applied during 4"-VGF-Ge growth for even better tailoring of the Lorentz force distribution in the melt [FR12]. Ultrasonic vibrations with frequencies between kHz-MHz, transmitted with a horn submerged in the melt, were additionally supplied [Ubb12]. Both fields caused a nearly total removal of the diffusion boundary layer for an effective prevention of solute enrichment at the growing interface. The axial carrier distribution approached the theoretical Scheil curve. The risk of constitutional supercooling was minimized.

Due to the high electrical conductivity of the liquid phase and the low melting temperature (see table 1.1) germanium is a good model substance for the development of the VGF process with the heater-magnet module. But experiments with other materials have not be performed yet. However a numerical study on the influence of a TMF generated in a HMM on the interface deflection for different materials (e.g. BaF_2, CdTe, YAG) with varying electrical conductivities and latent heat of fusion was carried out [Dro12a]. Aim was to test the feasibility of such applications within the given parameter area of the HMM. An optimized downward TMF can increase the convexity of the interface even in low conductivity materials. In these instances higher frequencies are favored.

3 Methodology

3.1 Enhanced VGF growth of GaAs

Process intensification can be defined as a set of often radically innovative principles in process and equipment design. They can bring significant benefits in terms of process and chain efficiency, capital and operating expenses, quality, wastes, process safety, and more[1]. This principle is a well established method in chemical industry (see [Sta00] for an extensive summary) and can also be applied for crystal growth.

The current challenges in growth of a semiconductor material are characterized by an enhancement of the yield and efficiency of a single growth process. Here, a consistently good or even improved quality of the crystal is desired. The efficiency of a growth process is determined by the utilizable single crystal mass grown per time and the associated energy consumption. Process intensification can be achieved, e.g. by up-scaling, growth with larger growth rates, and the growth of several crystals at the same time in a multi-crucible setup [Dro13a]. In chemical industry such parallel processing is often labeled as numbering-up approach [Sch04a]. Every approach has its advantages and disadvantages. They might be emphasized or conquered with the additional application of a TMF. The consolidation of these intensification approaches on a industrial scale using the KRIST$\widetilde{MAG}$® technology shall be tested and evaluated.

First, a TMF parameter study on the impact on solid-liquid interface shapes and crystal properties has to be performed. Improved structural and electronical quality is targeted, suitable optimized TMF parameters need to be transferred to the intensification approaches. The appearance of synergy effects for combined application of TMF and the given intensification approaches shall be examined.

3.1.1 Scale-up method

The approach of scaling-up the process to increase the yield of a growth run may be the most self-evident and prevails in industrial crystal growth. Short 200 mm VGF-GaAs crystals, with an aspect ratio H/D$\leq$1, were reported with structural and electronical features similar to those known for state-of-the-art 150 mm VGF-GaAs [Ste03].

The magnitude of the radial temperature gradients also rises with an increasing diameter. This can lead non-stationary or even turbulent convection. Temperature

[1] Definition taken from the European Roadmap for Process Intensification, 2007

fluctuations cause a worsening of the micro-homogeneity. More latent heat is generated at the solid-liquid interface, unfavorable melt convection gives rise to high interface deflections and thermal stress. This results in increasing EPDs and an increased risk of polycrystalline growth with increasing crystal mass.

In addition to the scale-up approach with increasing crucible diameter, an increase of the melt mass can be performed with a constant diameter, i.e. an aspect ratio H/D>1. Here, a higher fraction of the grown crystal can be used for wafering. Increasing the mass of the feedstock is technologically easily feasible and is in principle only limited by the crucible lengths and the size of the existing growth setup. The crystallization process needs to be prolonged, but the melting and the shut down phase would be very similar compared to the standard process. Labor effort, working gas and cooling water consumption and the growth setup itself were nearly identical for various loadings.

However, increasing the ingot length introduces novel obstacles. If the axial temperature gradient is kept constant during upscaling compared to the standard process, overheating of the melt and arsenic evaporation may occur. The temperature maximum in the melt cannot be increased. Adjustments of the growth recipe and thermal gradients are necessary. A further increase of the crystal size reduces the surface to volume ratio and hinders the heat exchange. The ability to remove enough latent heat per time declines, due to the increase of heat resistance (see the heat flux balance equation 2.1). With steady temperature gradients, heat removal is hampered, and the growth velocity is limited.

The application of a TMF during scale-up may help to improve heat removal, interface morphology, micro-homogeneity, and process stability and thus aid in process intensification.

3.1.2 Speed-up method

Increasing the growth velocity shortens the process time and therefore reduces energy consumption and working hours. However, challenging is the increasing amount of the released latent heat per time, that cannot efficiently be removed (see equation 2.2). The fraction of transported heat through the axial thermal gradients at the interface limits growth, not necessarily the increasing magnitude of latent heat itself. In order to prevent increasing concave interface deflections with rising growth rates, leading to thermal stress and the reduction of crystal quality, a TMF induced change in convective flow may help to reduce the radial thermal gradients.

Dropka and Frank-Rotsch numerically investigated matching TMF parameters in a heater-magnet module for enhanced VGF-GaAs growth velocities from the conventional 2-3 mm/h up to 9 mm/h [Dro13a]. Intended was the best possible interface morphology with respect to the interface shape without the application of a magnetic field. For all growth rates, Lorentz forces were able to reduce the concave bending compared to the pure buoyancy regime, but the shaping efficiency of a TMF decreased with increasing growth velocities.

In this study, these results shall be transferred and compared to actual growth experiments.

3.1.3 Numbering-up method

The simultaneous growth of multiple crystals represents the largest enhancement of the throughput in one growth run. The size of the simultaneously crystallizing area and the ability to remove the latent heat rises proportionally. The obstacle of a limited growth velocity, like in the scale-up method, is avoided. Disadvantages of such a setup may lay in thermal asymmetry effects. They cause a decrease of the radial homogeneity of structural and electronic properties on a wafer compared to the standard process.

Several patents describe varying VGF/VB multi-crucible design layouts. In the setup by Uehara et al. [Ueh00] a number of crucibles within a furnace are heated each with their own resistive side heaters. Thermal insulation between the crucibles prevents thermal interference, the temperature field is symmetric for every heater. However, plenty of insulation material makes the setup thermally inert and energy consuming. In contrast, in the setup described by Eichler et al. [Eic08b], several rotationally symmetric arranged crucibles are comprised by a large circular outer side (magnet-)heater. A second inner (magnet-)heater can also be situated along the inner axis of the furnace. Radial temperature inhomogeneities are minimized using a filling material between the crucibles, which is adapted to the thermal conductivity of the melt. Growth results of a multi-crucible Bridgman furnace with an outer heater have been published for oxide single crystals [Xu04, Wu07]. Here, the results demonstrated the validity of multi-crucible growth for mass production for this material. Frank-Rotsch et al. [FR10] applied the concept of the heater-magnet module to a multi-crucible setup. Thermal asymmetries, which give rise to a inclination of the solid-liquid interface, should be compensated through the application of an inner and an outer heater-magnet module encompassing rotationally symmetric arranged crucibles. Traveling magnetic fields should provide symmetrical mixing for flattening the interface and homogenizing the melt. Disadvantageous is, that the adjustment of homogeneous magnetic fields in each of the crucibles is not possible.

In the patent by Dropka et al. [Dro13c] the approach of a circular (magnet-)heater, which comprises all crucibles and the approach of separate heaters for each crucible is dropped. Instead, a layout of a heater-magnet module is proposed, whose coils are specially arranged to embrace and store several crucibles. The coils windings can take several shapes and are always connected to each other. Advantageous is the generation of almost equal magnetic field in a variety of crucibles. Symmetrical temperature and magnetic fields can be created. Benefits are the multitude of the heater-magnet module parameters, variable phase shift, double frequency and current.

Based on this concept, within the framework of this thesis a multi-crucible VGF setup was built and put into operation. Figure 3.1 shows the used multi-crucible heater-magnet module design. It consists of three vertically stacked graphite coils

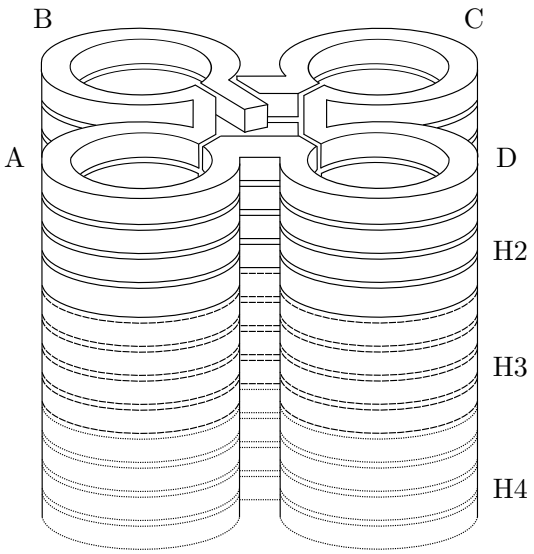

Figure 3.1: Sketch of the multi-crucible heater-magnet module with three coils and cloverleaf-shaped windings with the ability to simultaneously grow four crystals denoted A-D

with cloverleaf-shaped windings embracing all four crucibles (their respective position is denoted A-D). The current is supplied from the center, objective was the most beneficial exploitation of the pressure vessel. Beneficial compared to other multi-crucible setups is that no insulation is situated between the heaters. The temperature responds faster to changes, gradient fields are more easily adjustable and heating and cooling rate are larger. The energy consumption is minimized.

Until now, no growth results of the multi-crucible growth with the application of a non-steady magnetic field were published. It shall be analyzed, whether GaAs single crystals with the same structural and electronic properties compared to standard process can be grown within a multi-crucible setup, how eventual asymmetries can be compensated and the interface morphology, micro-homogeneity as well as process stability can be improved with an applied TMF.

3.2 Numerical simulations

A global 3D numerical model of the single- and multi-crucible furnace and power distributions in heaters mimicked the real setups and parameters used in growth experiments. Simulations were performed for the crucible size of 4" loaded with 5-9 kg of GaAs. For 3D CFD (Computational Fluid Dynamics) simulations, the commercial finite-volume code ANSYS CFX 14.0 was applied. Magnetic 3D simulations were performed using finite elements commercial code ANSYS Emag. All

simulations were conducted by Dr. Natasha Dropka from IKZ Berlin. More details on used simulation parameters are given in [Dro14a].

The results of global furnace CFD analyses provided the boundary conditions for local simulations of the melt flow with and without TMF. Melt flow in case of pure buoyancy was used for initiation of the TMF driven melt flow and as a benchmark for comparison. Prior to and during experiments, simulations on the influence of AC magnitude, frequencies and phase shift on the Lorentz force field in the melt container with respect to intensity, distributions and its direction were performed. Numerical simulations focused on the optimization of the TMF parameters with respect to the shape of the solid-liquid interface. TMF parameters were considered and applied in growth experiments and their impact on the interface shape was compared.

3.3 Methods of characterization

Various characterization methods were applied to characterize structural and electronic properties of the grown Si-doped and SI GaAs crystals. The characterization results were used to evaluate and improve the growth process and TMF parameters (interface morphology, EPD, residual stress), to examine effects of the TMF on segregation (Hall measurements, SIMS), and to investigate the mechanisms of polycrystalline growth starting near the crucible wall in SI GaAs (LST).

3.3.1 Shape of the solid-liquid interface

The knowledge of the shape of the solid-liquid interface is of primary importance to examine the influence of a TMF on the growth process. Therefore, longitudinal sections in <100>- and <110>-directions of the crystals parallel to the growth axis were analyzed. The progression of the growth from seeding position to the crystal end was analyzed.

DSL etching

For the analyses of a large variety of crystal features and defects, both crystallographic and chemical nature, i.e. striations, dislocations, precipitates, facets, and twins, etching with a diluted chromium oxide-fluoric acid mixture under light illumination was applied, also known as diluted Sirtl-like etchant with light (DSL) method [Wey83, Wey86, Gil96]. Etching was performed using a aqueous solution of CrO_3 (33%wt) and HF with the ratio 5:1 diluted with H_2O with the ratio 1:1 under light. The features of the etched surface were examined and assessed with an optical microscope using Nomarski or differential contrast (DIC). The etching procedure was conducted by Dr. U. Juda from the IKZ Berlin.

Especially for doped GaAs, this sensitive method allows to study important crystal features, which give information about the growth process, e.g. interface morphologies, striation distances, glide dislocations, facet sizes and facet breakdowns etc.

In undoped GaAs dislocation cell structures and the formation of low angle grain boundaries are of particular interest. Here, the interface shape cannot be determined due to the lack of quantifiable microscopic charge carrier fluctuations.

Infrared transmission measurements

Infrared transmission (IRT) analysis is a qualitative method to measure contrast variations on the double-sided polished longitudinal cuts both due to IR absorption and variations in refractive index. Thickness of the cuts in <100>- and <110>-direction for GaAs:Si and SI GaAs was 2 mm and 3 mm, respectively. Contrast variations are generated by surface and volume effects like impurity or dopant variations, grain boundaries, etc. The absorption coefficient α is linearly dependent on the net free carrier concentration [Car88], which can be used for the determination of the micro-distribution of free charge carriers in GaAs:Si. Microsegregation effects can be analyzed and the progression of temporal dopant incorporation fluctuations reflect the interface morphology. Naturally, imaging in undoped GaAs is provided only by extinction, through scattering on precipitates and absorption around dislocations and the forming cellular networks. Here, a determination of the interface shape is not possible. Generally, the refractive index varies around dislocation lines. Here, optical contrast is generated analogous to the optical schlieren method and a rough qualitative analysis of dislocation densities and types is possible.

A laser diode with a wavelength of 1125 nm is operated below lasing threshold for a nearly homogeneous exposure of light on the sample. Image acquisition is performed with a lens system and a cooled silicon CCD. Longitudinal crystal cuts are automatically analyzed in sections of 8.60×6.88 mm^2. The measurements were performed by M. Naumann from IKZ Berlin. The contrast of the IRT pictures in this thesis was adjusted for maximum visibility.

3.3.2 Electronic and physical properties of the GaAs single crystals

For characterization of TMF induced changes of electronic and physical properties in the grown crystals, the following measurement methods were applied.

Etch pit density

The visualization of dislocations and the determination of their density was carried out by etching with a KOH melt at 400°C on wafers and half-wafers cut in [001] direction. Here, atoms within the area of tension of surface near dislocations are dissolved. Etch pits are formed, which can be counted using an optical microscope. The determination of the etch pit density (EPD) was carried out according to DIN 50454-1 (test point scheme A) and represents a measure for wafer quality. Measurements were conducted by Dr. U. Juda from the IKZ Berlin.

Residual stress

The thermal stress field during growth and cooling is not only affecting dislocations but also leaves frozen in residual stress after the cooling down of the crystal. With high residual stress structural and electrical properties of the crystals can decline, even cracking during wafer processing can occur. Residual stress at room temperature was measured by M. Naumann at the IKZ Berlin on longitudinal cuts with a scanning infrared polariscope using the effect of stress-induced birefringence.

Hall measurements

Smaller selected samples with 10×10 mm^2 and 5×5 mm^2 cut from different axial and radial positions from the longitudinal sections were analyzed by means of Hall effect measurements after van der Pauw [vdP58]. Specific electrical resistance ρ, charge carrier mobility μ and charge carrier density n were measured. The measurements were carried out by M. Pietsch from IKZ Berlin.

Laser scattering tomography

A spatially resolved qualitative analysis of dislocation densities and types was possible with LST measurements. A Nd:YAG laser (1064 nm, 1 W, cw) is used to irradiate a plane inside a sample. Light is scattered by As precipitates on dislocation lines [Cul80]. Incident laser beam and signal acquisition are perpendicular to each other. Imaging is performed with a Si-CCD matrix camera. Depth integration is applied. While imaging, the irradiated plane is continuously moved into direction of observation. In addition to the scattering signal, in GaAs:Si crystals a photoluminescence (PL) signal at around 1300 nm caused by a $Si_{Ga}V_{Ga}Si_{Ga}$ complex [Lei04] is measured. A quantitative analysis on Si or charge carrier concentrations with the PL signal is not possible. The PL signal has its peak around $n=5\times10^{17}$ cm^{-3} and decreases quickly at lower and higher charge carrier densities [Nau06]. LST measurements were conducted by M. Naumann at the IKZ Berlin. Samples were specially manufactured, at least two crystal planes perpendicular to each other needed to be polished. More details about the method are given in [Nau00].

Secondary ion mass spectrometry

Dynamic secondary ion mass spectroscopy (SIMS) was used to determine the bulk concentrations of the elements carbon, boron, and silicon on different positions inside selected GaAs:Si crystals. Samples of the size 5×5 mm^2 were cut from different axial and radial positions from longitudinal sections. The measurement position was always in the sample center. A focused beam of primary ions is used to sputter the surface of the sample. The subsequently ejected secondary ions can be analyzed by their mass/charge ratios using a mass spectrometer. The determined mass spectra corresponds to the chemical composition of the sample. Quantitative analysis requires a calibration sample with a known concentration for comparison.

Cs and O_2 primary ions have been used with an energy of 14.5 keV and 8.0 keV, respectively. Cesium primary ions enhance the formation of negative secondary ions and were therefore used for silicon and carbon analysis, while oxygen ions increase the formation for positive secondary ions and were used for boron analysis [Yu86]. Depth profiles were measured with depths calculated from the ablation rate. The analysis started deeper in the sample material. Implantation standard samples were already existing. Within a sputtered thickness of 0.5-1.5 µm, 200-500 measurements were performed. The measurements were carried out on a CAMECA ims 4f (B) and a CAMECA ims 4f-E6 (Si and C) SIMS in cooperation with RTG Mikroanalyse GmbH Berlin.

4 Growth experiments

4.1 The VGF growth setups

Two different growth setups were used for the growth of 4" VGF GaAs crystals in this work. The single-crucible setup Kronos was modified for GaAs growth. In this furnace model experiments for Ge growth with a TMF had already been carried out before [FR09, FR12]. The multi-crucible setup ECM was newly built from scratch specially for GaAs growth experiments.

4.1.1 Single-crucible setup

Figure 4.1: Heater-magnet module inside of the commercial VGF growth setup Kronos, (left) closed setup from outside, (right) HMM of the Kronos after removal of the high-pressure vessel and main parts of the insulation

The commercial VGF equipment Kronos from PVA TePla AG was especially designed for the high-pressure growth of compound semiconductors. For the growth with TMF, the standard meander-type side heater was replaced by a heater-magnet module with three side heaters H2-H4 (described in section 2.2.2). Additionally, the size of the bus bars was reduced in order to minimize magnetic field asymmetries [Kas08]. The resistive top and bottom heaters H1 and H5 remained unchanged. All heaters are made of graphite. The insulation material between heaters and steel vessel is made of graphite, CBCF (carbon bonded carbon fiber), and graphite

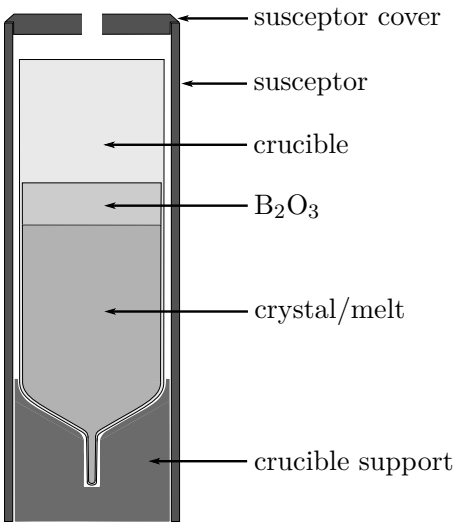

Figure 4.2: Layout of the hot zone with filled crucible, crucible support, susceptor and susceptor cover

felt, which is optimized for the needed thermal gradients and the GaAs growth temperature of 1238°C.

The layout of the hot zone inside the HMM is depicted in Fig. 4.2. It is situated on top of the bottom heater. A susceptor around crucible and crucible support provides additional downwards directed heat flow for the enlargement and homogenization of the axial temperature gradients. Its standard material is graphite. A susceptor cover with a hole for pressure compensation serves as a splash guard. The hot zone with the crucible is loaded into the setup from the bottom. Nitrogen is used as working gas. The setup is equipped with pressure controllers for pressure ramping or keeping at a desired reference value. Seven thermocouples are located inside the furnace at fixed positions: Near the bottom, top, and the three side heaters, at the upper and at the lower seed area close to the crucible wall. All of them are used for process control and observation.

The axial temperature profiles were measured to create the desired vertical thermal gradient field and to develop a suitable growth recipe. A vertically moveable ceramic pipe, containing three thermocouples at a constant distance, was installed at the top of the growth setup. Utilizing a small motor, these thermocouples were pulled upwards to measure the axial temperature from the beginning of the seed up to the top heater. Measurements were performed using a prepared pBN crucible with a hole in the bottom seed area and a crystal-shaped graphite dummy with a drilled hole along the inner axis as a substitution for the GaAs melt. An overpressure of 3 bar was applied, equal to the crystal growth experiments. Temperatures and heater powers for different process steps were adjusted to generate the desired thermal gradient field. Bottom and top heaters were temperature controlled. The

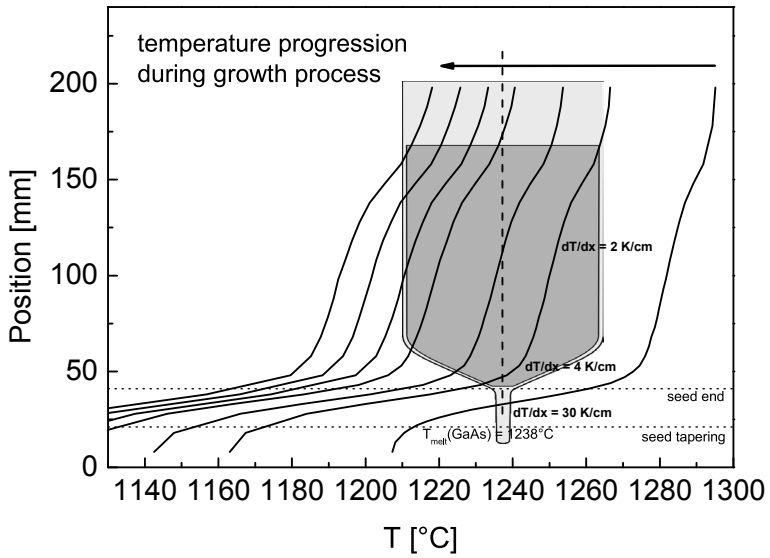

Figure 4.3: Measured axial temperature profile in the Kronos growth setup. The measurement was performed using vertically moveable thermocouples within a graphite dummy with a drilled hole along the inner axis.

side heaters were controlled over the heater powers to ensure enough total current for the creation of the TMF. Suitable values for heater powers and temperatures were chosen, the temperature variation during growth in the Kronos setup is shown in Fig. 4.3.

The GaAs melting point of 1238°C was set for different axial positions representing upwards proceeding interface positions. Emphasis was put on steady gradients in the cylinder area of the crucible and larger gradients in the seed to ensure reproducible seeding. From 30 K/cm at seeding position, the gradients decreased to around 4 K/cm at the beginning of the cone to stable 2 K/cm during the rest of the growth process. The curve in the measurement in the upper cylinder region was caused by the thermocouple exiting the graphite dummy.

A thermal growth recipe was generated on the basis of the temperature profiles with migrating interface positions. The respective heater powers and temperatures for each growing step were loaded into the control software. During growth, the heater powers and temperatures were ramped automatically to the desired values. The offset between dummy measurements and the actual temperature in the melt, obtainable by their analogous interface positions, was determined to be only 5-10°C. This offset was acknowledged during programming of the growth recipe. No differences between the thermal gradients in the graphite dummy and GaAs melt were observed.

The control and adjustment of the TMF parameters was realized through a separate control system. Alterations of the TMF parameters during growth needed to

be made manually. When the TMF was switched on and the alternating current increased, the direct current of the side heaters was automatically decreased to match the needed stable total current for the determined heater power.

Influence of susceptor material on the thermal properties

Graphite is the standard susceptor material. It is economical and homogenizes the axial thermal gradients. However, its large thermal conductivity does not only have advantages. Radial temperature gradients rise and radial heat dissipation is promoted when graphite susceptor, crucible, and crucible support are in direct contact. This can lead to an enhanced concavity of the interface. Furthermore, the small electrical resistance of graphite leads to small penetration depth of the magnetic field due to the skin effect and diminishes the impact of a TMF on the melt flow. Additionally, because of high thermal conductivity, the transfer of temperature fluctuations from the side heaters to the melt may be enhanced. Therefore, the utilization of different susceptor materials was experimentally investigated. The impact of susceptors made from Al_2O_3 felt and isotropic BN on the axial temperature gradients in the single-crucible setup was compared with the standard graphite susceptor. The material data is shown in table 4.1. Both, Al_2O_3 and BN, are electrically insulating, which ensures enhanced TMF effectiveness. Their respective thermal conductivity is markedly reduced.

	Graphite (FU8957)	Al_2O_3 felt	BN (isotropic)
specific heat capacity c [J/kgK]	2424	910	2082
thermal conductivity λ [W/mK]	34	5	14
specific electrical resistance ρ [$\mu\Omega$m]	14	insulator	insulator

Table 4.1: Material data various parts of the hot zone at 1238°C

Measurements of the axial temperature profiles were conducted with identical layout as used before with graphite dummy and BN crucible with a hole in the bottom. First, same temperatures and heater powers were adjusted. Results of the respective temperature gradients as a function of the interface position are shown in Fig. 4.4.

Driven by the high thermal conductivity of graphite, the large thermal gradients in the seeding area decreased rapidly and reached single-digit values shortly after the seeding position. In the cylinder, gradients were stable with 2 K/cm. With the same heater configuration, the Al_2O_3 felt susceptor showed similar seeding gradients, but very small gradients from cone end to cylinder end of 1.2-1.3 K/cm. With the isotropic BN susceptor similar seeding gradients were reached, but they were decreasing more slowly to 1.6-1.8 K/cm in the cylinder. A decreased thermal conductivity of the susceptor resulted in smaller temperature gradients with the same heater adjustments.

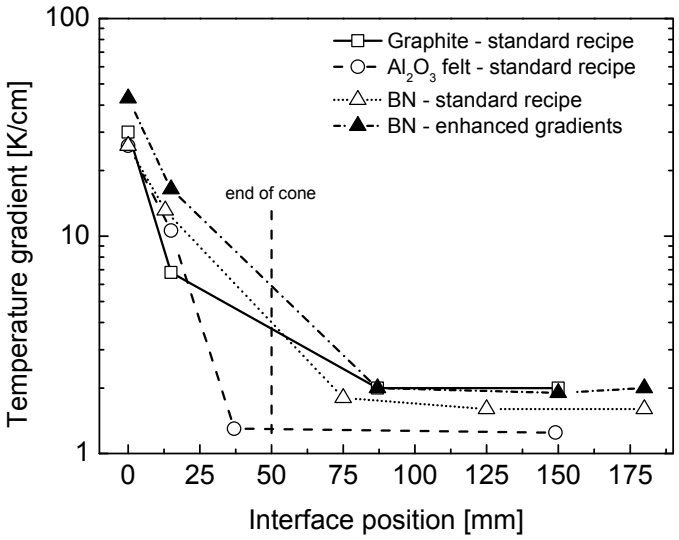

Figure 4.4: Temperature gradients as a function of the interface positions from various axial temperature profile measurements in the single crucible setup with different susceptor materials

The Al_2O_3 felt was not suitable for utilization during growth. Axial temperature gradients were too small for effective heat removal. Furthermore, the material became porous after around 300 hours at growth temperature. In a second measurement, the heater settings were adjusted to increase axial temperature gradients for the BN susceptor. Here, in the cylinder area values were with 2 K/cm same as graphite. Gradients in the seeding channel and cone were enhanced.

Most crystals grown within this work were grown with standard graphite susceptor. A section in chapter 5 is dedicated to the comparison between crystals grown with graphite and BN susceptor with small and large gradients, respectively.

4.1.2 Multi-crucible setup

The multi-crucible VGF growth setup ECM was built and installed based on the numbering-up method to increase the single crystal yield per growth run (Fig. 4.5). Experience from conventional single-crucible VGF growth with TMF helped to optimize this concept. A pre-existing growth setup was converted into a multi-crucible VGF setup, with a heater-magnet module for the simultaneous growth of four 4" GaAs crystals as centerpiece. Beside the three cloverleaf-shaped HMM side heaters H2-H4 (see Fig. 3.1), round resistive top and bottom heaters, H1 and H5 respectively, are located inside the high pressure vessel and cover all four crucible positions A-D. The complete heater setup includes an insulation specfically designed and optimized for GaAs growth. Unlike the single-crucible Kronos setup, the crucibles are mounted and removed from the top of the hot zone. Pressure vessel and top

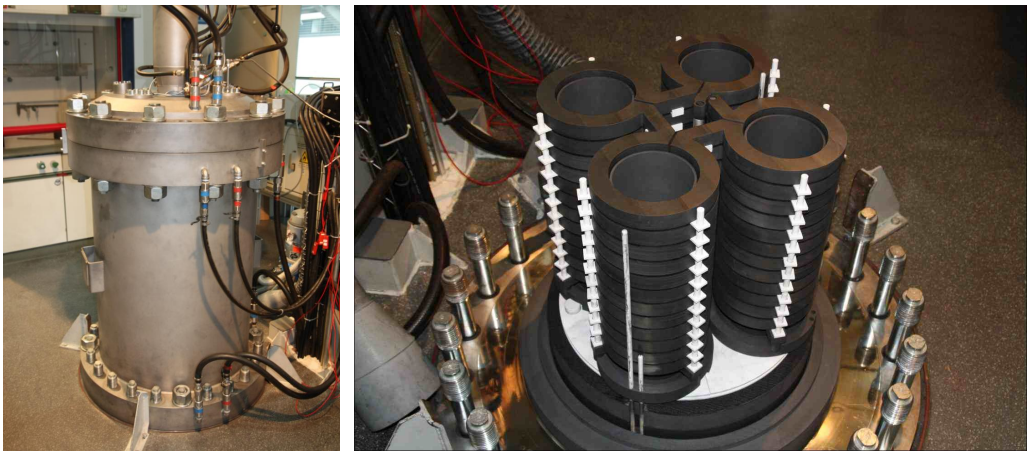

Figure 4.5: Multi-crucible setup ECM with heater-magnet module, with the ability to simulaneously grow four 4" crystals within the cloverleaf-shaped windings of the three side heater graphite coils: (left) closed setup from outside, (right) HMM of the ECM after removal of the high-pressure vessel and main parts of the insulation

heater are lifted in order to do this. The layout of the hot zone is identical to the single-crucible Kronos setup. Only the susceptor is longer for a possible use of longer crucibles to further increase of the GaAs crystal mass.

For the most part, the basic layout of pressure and temperature control was adopted from the Kronos setup, nonetheless a variety of improvements and enhancements were made during installation. GaAs was grown with a nitrogen overpressure of 3 bar. Here, steady pressure was not only achieved by a pressure controller and a gas inlet/outlet. Installed mass flow controllers allowed growth under a constant exchange of the working gas as well. Five thermocouples for each heater and two near the seeding channel at the crucible wall in position A were used for process control and observation. Like in the Kronos setup, bottom and top heater were temperature controlled, the three side heaters were controlled over the heater powers to ensure a steady current supply for the TMF.

Asymmetry effects of temperature distribution and magnetic field in each crucible position A-D must be strongly avoided to ensure good quality of every crystal grown with the numbering-up concept. Therefore, numerical simulations of magnetic flux density B and temperature distribution in the multi-crucible VGF setup under TMF utilization were made. No strong variations of the magnetic flux density B for downwards-directed TMF in every crucible position were observed (Fig. 4.6). Only a slight tilting of B and hence increasing Lorentz force densities towards the center of the HMM inside every crucible was obtained. It resulted from the openings of the coil windings around the center. Under pure buoyancy force the temperature isosurfaces were tilted against the HMM center. Enhanced temperatures in the

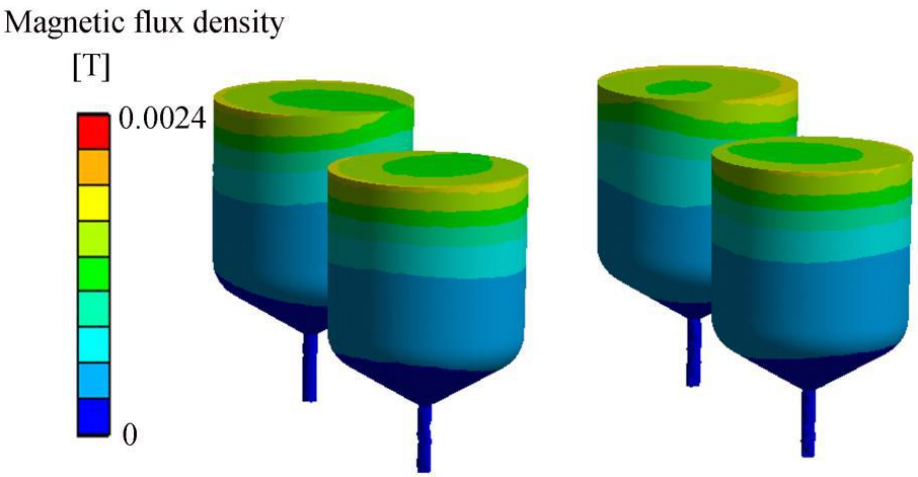

Figure 4.6: Numerical simulation snapshot of the magnetic flux density B of a downward-directed TMF in the multi-crucible VGF setup ECM [Dro14b]

HMM center were reached due to the current supply of the HMM situated along the central axis. The presence of a TMF induced Lorentz force density advantageously counterbalanced the thermal asymmetries (Fig. 4.7). The impact of the TMF on the melt was comparable to the single-crucible setup Kronos.

In addition to numerical studies, extensive experimental characterization of the new growth setup was performed. Here again, the main method was temperature profile measurements. They were applied to investigate differences in the axial temperature profiles of every crucible position and to create a desired temperature field for GaAs growth. The measurements were performed under standard growth conditions using up to two moveable ceramic pipes containing three thermocouples at a constant distance within the inner axis of a crucible. Every crucible position A-D could be arbitrarily chosen for measurement. For this purpose the respective ceramic pipe had to be installed to another suspension, which required opening of the growth vessel. The axial temperature gradients of two different crucible positions were measured in the same run. The axial temperature from the beginning of the seed up to the top heater was measured, again using graphite dummies and pBN crucibles with drilled holes in the seeding channel. Heater powers and temperatures were adjusted to match different process steps and desired thermal gradients.

In Fig. 4.8 the measured standard axial temperature gradients for various growth steps in the ECM setup for crucible position A and C are shown. Specific differences of the respective HMM positions can be seen in the graph, profiles with identical heater settings have the same line pattern next to each other. To ensure a stable seeding position, the temperature gradient in the seeding channel was set to be around one order of magnitude higher than in the cylinder. At the seeding position, the temperature gradient was about 10 K/cm, in the cylinder between 1.2-1.75

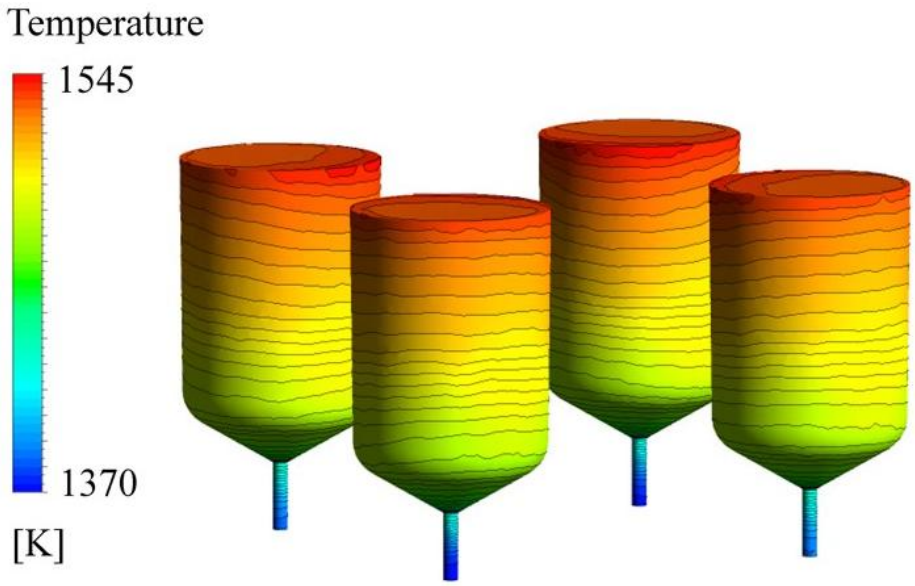

Figure 4.7: Numerical simulation of the temperature distribution in the multi-crucible VGF setup ECM at the beginning of the crystallization of 7 kg of GaAs with an applied TMF [Dro14b]

K/cm. Again, the curve in the upper cylinder region was caused by the thermocouples leaving the graphite dummy. With similar heater power distribution axial thermal gradients were smaller in the ECM compared to the single-crucible setup standard process. This is caused by the altered thermal layout and the modified geometry of the HMM. Different crucible positions showed only minor temperature deviations. In position A, temperatures were somewhat higher, which led to a height difference of the melt isothermal line from 10 mm in the seed up to 19 mm in the upper cylinder. Furthermore, the axial temperature gradients in position C were around 15% smaller compared to position A. These effects were caused by the small holes in the crucible support for the two seed thermocouples in position A and minor asymmetries of current supply and insulation.

Occurring differences in axial temperature profiles can be structurally compensated. The measurements shown in Fig. 4.8 were reproduced after raising the crucible in position C by placing a 15 mm thick graphite disk under the crucible support. This led to the compensation of the melt isothermal line offset in both crucibles in the seed and the lower crystal cone. Alterations of the insulation below the bottom heater resulted in nearly doubled temperature gradients in the seed with the same heater power distribution and therefore improved downwards-directed heat dissipation. Temperature gradients in the cylinder remained stable due to the length of the HMM.

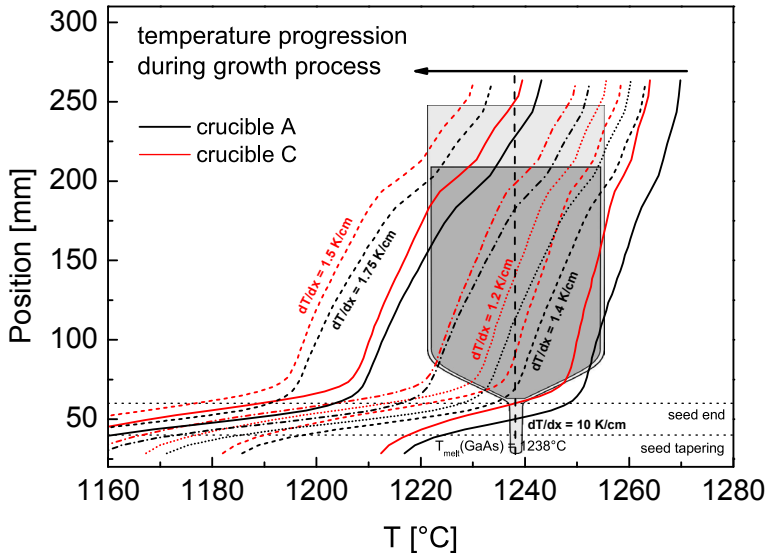

Figure 4.8: Measured axial temperature profile in the ECM growth setup without any structural compensations. Measurements were performed using vertically moveable thermocouples within the inner axis of the crucible positions A and C. A graphite dummy and a crucible with a drilled hole along the axis were used to measure temperature gradients from the seed to the top heater.

The growth recipes were generated on the basis of the temperature profiles. In the ECM setup the not only heater power, temperature, and gas flow is controlled by the predetermined growth recipe, the control of the TMF parameters is also integrated. Therefore, unlike to the single-crucible setup Kronos, predefined growth recipes can simultaneously control the thermal process and match the TMF parameters to the growth process. Interface marking with the TMF (see section 4.2.3) can be automatically performed by the recipe, too. The coupling of TMF and heater control in the ECM control software requires a complete set of parameters in every recipe step even if only a few variables are changed during growth. This leads to about 100 recipe steps for a standard growth process with TMF. Therefore, recipe programming in the ECM was promoted with the help of a self-programmed Python script. Heater settings for every recipe step were calculated after entering desired cooling rates and TMF parameter adjustment steps.

4.2 Experimental conditions

4.2.1 Preparation before growth

For growth experiments 4" pBN crucibles from Shin-Etsu Chemical Co. Ltd. and Momentive Performance Materials Inc. were used. Their multiple reproducible application was possible. The preparation of the pBN crucibles is crucial. Impurities and disruptions at the crucible walls have to be thoroughly removed. Because of the layered structure edges can form after removing the crystal from a previous growth run. They were carefully sanded off before several cleaning steps were applied. First, the crucibles were etched with aqua regia for one hour and then repeatedly rinsed with ultra-pure water. Subsequently, the pBN crucible was oxidized in a muffle furnace to produce a thin B_2O_3 layer inside the crucible. This layer was again removed by boiling in purified water. The whole procedure was repeated several times to ensure a high purity, in the last step the B_2O_3 layer was not removed to best possible prevent the contact of the GaAs with the pBN crucible wall during the growth process. As seeds, LEC and VGF grown GaAs single crystals with <100> orientation with a length of 40 mm and diameters around 10 mm were used. They had a tapering at or below the center to ensure a complete enclosure of the seeding area with molten B_2O_3 [Son00]. The seed crystals were ground to match the form of the seeding channel. Afterwards, they were etched with aqua regia and rinsed before they were loaded into the crucible. Around 400-500 g of B_2O_3 with varying water contents between 200-1000 ppm was utilized per growth run. B_2O_3 has a lower density than GaAs and therefore mainly floats on top of the melt during the growth process. To obtain a complete coating of the melt and the seeding region, a part of the B_2O_3 was loaded into the crucible between seeding channel and polycrystalline feedstock [Son00]. Already cleaned and etched pre-synthesized polycrystalline GaAs feedstock with masses between 5-9 kg was used. The packaging was opened immediately before mounting into the crucible onto the B_2O_3. Upon melting at around 450°C the liquid B_2O_3 encapsulated the seeding area and the solid feedstock. It also wetted the crucible wall. In case of n-doping, a weighed portion of etched and rinsed silicon with a derived initial concentration of 1×10^{19} cm^{-3} was added on top of the feedstock, along with a few grams of fused silica, according to [Son97]. The SiO_2 saturated the B_2O_3 to reduce the loss of silicon through the reaction with B_2O_3 (see section 2.1.3). The rest of the B_2O_3 was added on top to ensure a complete encapsulation during the melting, seeding and growing steps to preserve the stoichiometry of the GaAs. Finally, the mounted crucible was loaded into the growth setup. During loading it was made sure, that the crucible was centered on the crucible support and no tilting of the crucible axis was present.

4.2.2 Features of the growth process

The growth recipes were created based on the measured axial temperature profiles in single- and multi-crucible growth setup, respectively (Figs. 4.3 and 4.8). Starting

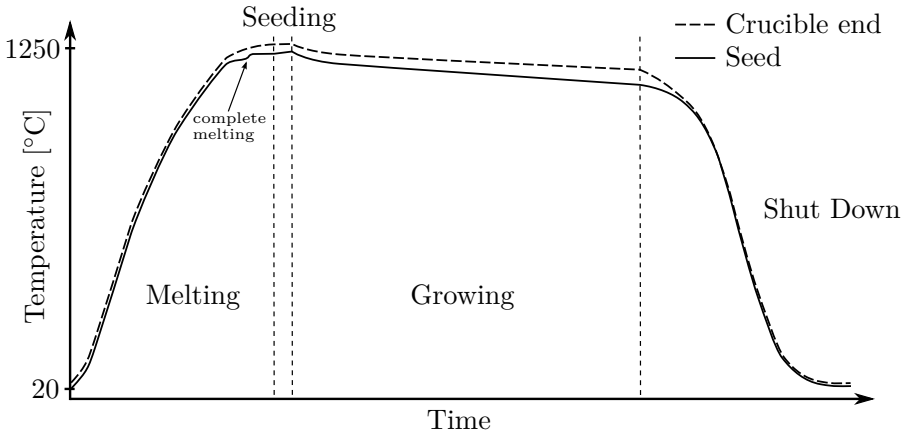

Figure 4.9: Temperature progression for the four steps of growth during a typical process measured by a thermocouple at the upper part of the seeding channel and a thermocouple near the crucible end

with the seeding position and the desired growth velocity, the cooling rate was matched to the measured thermal gradients for the relative interface position. Slight adjustments of the growth recipes were feasible after first growth runs with the help of the TMF marking technique (see section 4.2.3). Melting step and cooling to room temperature was also controlled by the predetermined recipe.

After loading and closing the furnace, the air was pumped out and the vessel was filled with nitrogen. Additional pumping and baking out up to 200-300°C guaranteed the dryness of the graphite parts. The VGF growth process can be divided in four major steps. Figure 4.9 shows the typical temperature cycle measured by the thermocouple at the upper part of the seeding channel and a thermocouple near the crucible end. In the melting step the temperature in the furnace was uniformly raised with a decreasing heating rate. The growth vessel was slowly filled with nitrogen until an overpressure of 3 bar was reached. With approaching of the melting temperature, the TMF was switched on. The complete melting of the feedstock was visible by a temperature peak of a few degrees near the seed. The heat of fusion was absorbed and at the end of melting the temperature rose with constant heater power. Afterwards, the melt was stirred with the TMF for a couple of hours for homogenization.

In the following step, the seeding, the temperature of the bottom heater was increased by 5°C in 5 hours to melt the seed back to the final seeding position. Crystal growth started from here. The growth velocities in the cylinder were, depending on the experiment, in the range 1.5-5 mm/h. The growth velocities in the seed and the cone were around 25% slower compared to the velocities in the cylinder. The parameters of the TMF were adjusted during growth to match the desired experimental targets. The shut down phase followed after crystal growth was completed. First, the axial temperature gradient inside the vessel was suppressed by cooling the

upper heaters (see Fig. 4.9). Then, uniform cooling inside the furnace was applied to minimize thermal stress in the crystal. The TMF was switched off, the overpressure was slowly reduced.

Solidified B_2O_3 tends to stick on the GaAs crystal. This induces stress, which can at worst lead to spalling of the crystal end and a reduced yield. Therefore, a new process step was introduced during cooling. Before the solidification of B_2O_3 at around 450°, a wetting layer of gallium was brought between the solid GaAs crystal and the molten B_2O_3. While loading the crucible into the growth setup, centered above it an ampoule with gallium was installed. After the growth process, this ampoule was mechanically destroyed and the liquid gallium dropped down into the liquid B_2O_3. Due to its higher density it penetrated the B_2O_3, covered the solid crystal and formed a layer on top of the GaAs. Once a furnace temperature below 50° was reached, the growth setup was opened and the crucible with the crystal was removed. The GaAs crystal and upper encapsulation were easily detached from each other. Considerably reduced spalling was obtained in comparison to experiments conducted without a liquid Ga buffer.

4.2.3 Marking of the solid-liquid interface with the TMF

The elimination of striations is highly desired when growing doped GaAs single crystals with a good quality. However, when the application of a traveling magnetic field leads to a reduction of microsegregation or even a full suppression, the effects of the TMF on the interface deflection cannot be measured. Furthermore, the actual growth velocity is difficult to obtain. When steady convection conditions prevent microsegregation, a targeted alteration of the melt flow can artificially induce fluctuations in composition through a temporary variation of the convection and the growth velocity. Hence, the TMF itself is a very effective and efficient tool to mark the interface.

The approach to mark the solid-liquid interface was a temporary alteration of the alternating current shares of the two TMF frequencies. The total alternating current did not change, but the AC ratio between TMF(f_1) and TMF(f_2). In the first step the AC share of the lower frequency TMF(f_1) was abruptly reduced for 15 minutes. Now, with a higher AC share of TMF(f_2), the force acting on the melt instantaneously increased (see equation 2.46). After 15 minutes the AC ratio was raised in around 10 steps back to the initial value before the marking process.

The impact of the marking process on the melt was measured by thermocouples near the crucible, as it is can be seen in Fig. 4.10. The temporary amplification of the downward directed force led to an enhancement of the convergence of melt flow and solid-liquid interface. This resulted in a minor back-melting effect and/or a local radial variation of the growth velocity. Thermocouples in the vicinity of the growth front detected a temporary increase in temperature. The continuously decreasing temperature changes for each marker in the picture were caused by the progressing growth and the increasing distance between thermocouple and interface.

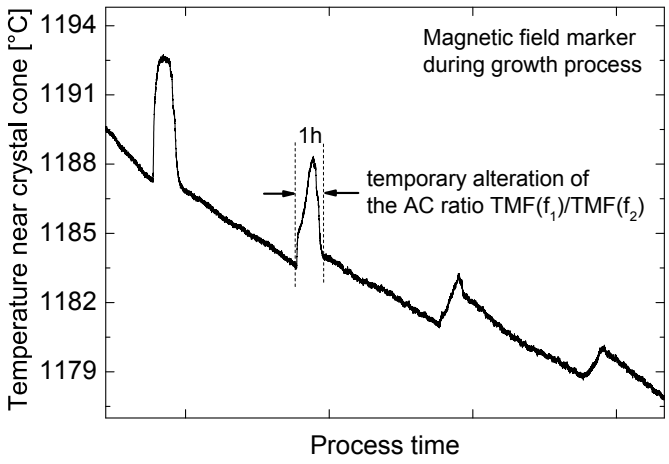

Figure 4.10: The temporary amplification of the downward directed force increased the temperature at the interface and led to back-melting, which marked the shape of the phase boundary

The artificially induced composition fluctuations were visualized by ex-situ analyses with DSL etching or IR transmission measurements on longitudinal cuts in <100>- and <100>-directions taken from the axis of the GaAs:Si single crystals. The resulting structure of such a interface marker is shown in Fig. 4.11. No striations were visible before increasing the Lorentz force. After remelting, the TMF field strength was reduced in 10 steps to the initial conditions. The striations disappeared again when the original TMF parameters were reached and kept steady. A striation stripe remained along the whole width of the crystal, representing the shape of the solid-liquid interface. The TMF markers were also visible on the outer crystal surface and their respective spacings were used for easy process evaluation and determination of growth velocities (see cylinder areas of the crystals in Fig. 5.1). Important TMF and non-TMF related characteristics of the growth process were studied with this marking technique: The deflection of the interface $\Delta z/R$ and the angle β between crucible and interface under steady TMF conditions (beginning of the marker), the change of the interface form with increasing influence of the higher frequency f_2 (change of the marker form), and the growth velocity between two markers. The latter was used to alter and improve the growth recipe.

A magnetic field for marking the interface was also used by Pätzold et al. [Pae02b] for the growth of 2" VGF-GaAs with a rotating magnetic field (RMF). Here, the change of the interface curvature from natural to forced convection conditions was observed with induced striations after switching on a RMF for 30 or 120 minutes, respectively. The strength of the RMF did not change during the marking process. Between the markers the RMF was switched off completely. An interface marker can also be realized with a variation of the heater powers through occasional power reduction or switching off the bottom heater and a back-melting with an enhance-

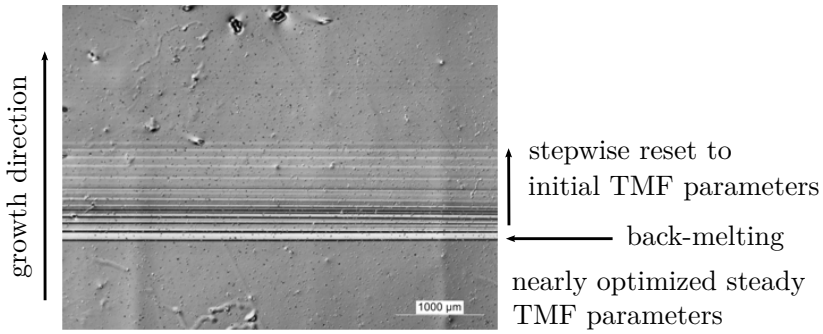

Figure 4.11: Interface marking process: Detail of a DSL etched longitudinal section, showing the back-melting and the stepwise changes of TMF parameters back to the initial values to mark the interface shape

ment of the heater power [Bir00]. But unlike with this technique, a TMF marker does not interrupt the predefined cooling rate itself, which can reduce the danger of disturbances during the crystallization. Using additional external forces, like Peltier cooling pulses, is another possibility to mark the interface, but would distinctly complicate the standard growth setup.

4.2.4 Sample preparation

Methyl alcohol was given on top of the solid B_2O_3 to detach the crystal from the crucible. It partially dissolved it and crept between material and crucible. Consequently, the crystal was knocked out of the pBN container, together with the remaining B_2O_3 and a few layers of BN from the crucible. Often, the seed broke off from the crystal during this procedure and had to be removed separately. The B_2O_3 and the layers of BN were removed from the crystal in a hot ultrasonic bath. The spalling of some parts of the lateral surface at the crystal cylinder and the often clam-shell marked fractures at the crystal ends were a result of the full encapsulation of the grown crystal. Some parts of the GaAs surface were detached after solidification of the B_2O_3 due to local adherence and different expansion coefficients (see Figs. 5.1). Measurements showed that the thickness of the removed areas is only a few 100 µm and that these areas have no influence on the physical crystal properties. The spalling was markedly reduced with the liquid gallium layer between crystal and B_2O_3.

The facets in <110> direction in the crystal cone helped with sample orientation. Longitudinal sections of the crystals were cut in <100> and <110> direction, wafer or half wafer for EPD measurements obviously in direction of growth. Samples were cut with a diamond wire saw, ground with a surface filing machine and if desired single- or double-sided chemo-mechanically polished, depending on the characterization method.

5 Interface shaping in VGF-GaAs growth with applied TMF

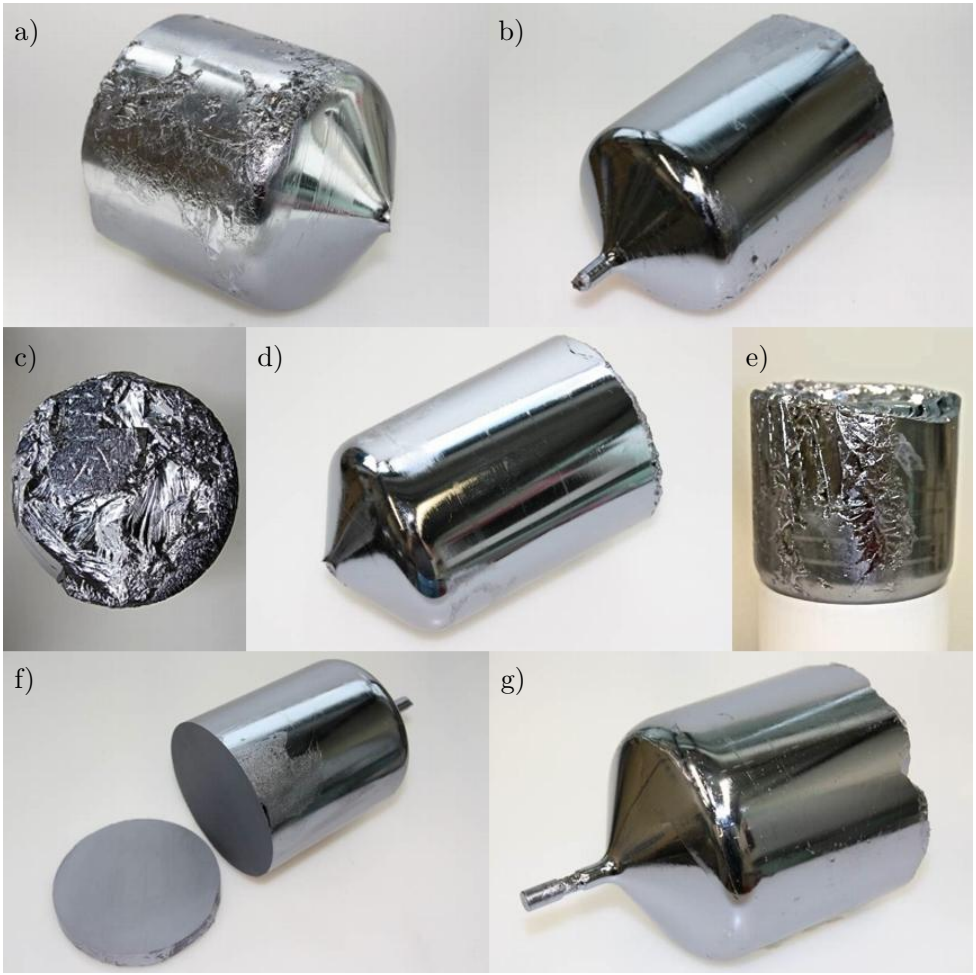

Figure 5.1: VGF-GaAs:Si single crystals grown with TMF with masses of 5-7 kg: facets in cone and crystal end in a) and c), visible interface markers in b), d), e), and g), spalled and glossy surfaces in a) and e), clam-shell marked fractures in c) and e), broken and intact seeds in a), d), and g) and a horizontally cut crystal end in f)

Within the framework of this thesis, 35 Si-doped and 6 semi-insulating 4" VGF-GaAs crystals were successfully grown in the single- and multi-crucible heater-magnet module. Nearly all of them were grown under the influence of double-frequency traveling magnetic fields with different parameters. Conducted GaAs:Si growth experiments focused on the impact of varying TMF parameters on the interface morphology. Here, changes of the interface were easily visualized using the TMF marking technique on multiple positions during solidification (see process description in section 4.2.3). In contrast to GaAs:Si, in SI GaAs the shape of the solid-liquid interface could not be obtained with this method. The approach to enhance SI GaAs growth laid in the optimization of the growth process and the TMF parameters for GaAs:Si first, and subsequent application to the growth of SI GaAs. The features of the VGF growth process of SI GaAs did not differ from the growth of GaAs:Si, obviously except the addition of Si and SiO_2 to the feedstock. Equal interface morphologies are assumed for the VGF growth of GaAs:Si and SI GaAs with identical conventional growth conditions and TMF parameters.

In this chapter, the impact on the interface morphology by applying different TMF parameters is shown. The direction of the longitudinal cuts for analyses of the TMF interface markers with DSL etching and IR transmission measurements was generally chosen according to the largest asymmetry visible from outside. All directly compared crystals were grown under identical thermal growth conditions and growth rates. The utilized parameters of the TMF, respective derived total magnetic flux densities B_0, and magnetic Taylor numbers for each frequency share Ta_m are displayed for every growth experiment. Two parameters were measured for quantitative comparison of the different effects of the TMF on the solid-liquid interface shape. The first parameter was the deflection of the interface $\Delta z/R$. It represents the maximum height difference of one marker along the growth direction in relation to the crystal radius (see sketch in Fig. 5.4). This parameter acts as a measure of overall effects of the TMF on the interface, i.e. thermal stress along the interface is directly linked to the interface morphology. The second parameter was the angle β between crucible wall and interface in the solid (see Fig. 2.3). This angle represents the ability of the TMF to alter the heat flux in the critical region near the triple point. It is mainly influenced by the anisotropic heat conductivity of the pBN crucible. With angles $\beta \rightarrow 90°$ thermal stress is reduced and the formation of a supercooled area is prevented. This supports the aim to avoid polycrystalline growth in this area. A progressive optimization strategy for a continual reduction of the interface concavity with TMF was used. After the thermal characterization of growth setup with dummy measurements, test growth runs with varying TMF parameters were applied. Comparison experiments, where each time only one TMF parameter was altered, were the foundation of the experimental strategy for interface flattening. Additionally, results from basic numerical simulations provided from Dr. Natascha Dropka were considered. After evaluation of the growth process data and the resulting crystal properties, TMF parameters were adjusted and growth experiments were repeated.

5.1 TMF parameter study

In the following, results from parameter studies for TMF frequency, phase shift, and current as well as their respective influence on the solid-liquid interface shape is presented.

5.1.1 TMF frequencies

An alteration of the TMF frequencies changed magnitude, direction and spatial distribution of the Lorentz forces and therefore the interface shape. Results from numerical investigations on Lorentz force density distribution in the melt inside the Kronos single-crucible setup as a function of the TMF frequency are shown in Fig. 5.3. With low frequencies the force direction was nearly perpendicular to the growth front. With rising frequencies the force direction tilted towards the center and flattened. Very large frequencies had a reduced convex interface shaping potential, due to the unfavorable angle of attack near the crucible walls. Furthermore, the magnitude of the Lorentz force density rose linearly as a function of the frequencies and was slightly asymmetrically distributed in the crucible. Therefore, the frequency shares of low and high frequency had to be appropriately balanced for a similar magnitude of force action with the application of double-frequency TMF.

In growth experiments, the sensitive melt reaction with TMF parameter modifications induced artificial striations. This enabled the direct analysis of changing interface morphologies under varying TMF frequencies during growth. A crystal was grown with with a double-frequency TMF(f_1,f_2) with AC of I_{tot}=45 A, an AC ratio of I_1/I_2=0.92/0.08 and a phase shift of 90°. During growth the AC ratios for TMF(f_1) and TMF(f_2), with low frequency f_1=20 Hz and the high frequency f_2=200 Hz, was changed in 10 steps. Fig. 5.2 shows an IRT picture from crystal center to the edge.

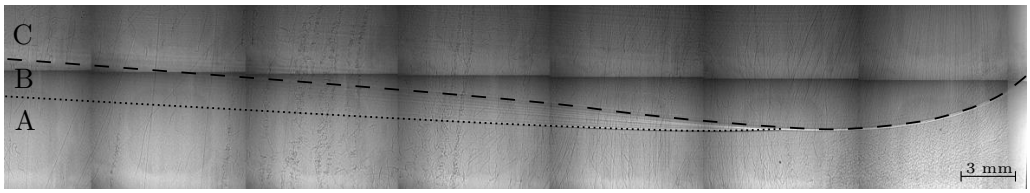

Figure 5.2: IRT picture from crystal center to the edge, the AC ratio of low frequency TMF(f_1) and the high-frequency TMF(f_2) was changed in 10 steps: interface shape of the single high-frequency TMF(f_2) (dotted line), w-shaped interface shape of the double frequency TMF(f_1,f_2) (broken line)

First, growth took place under double-frequency TMF, in the picture marked as area A. Then, for 15 minutes TMF(f_1) was switched off, total AC remained constant, i.e. only TMF(f_2) was acting on the melt. Remelting of the interface

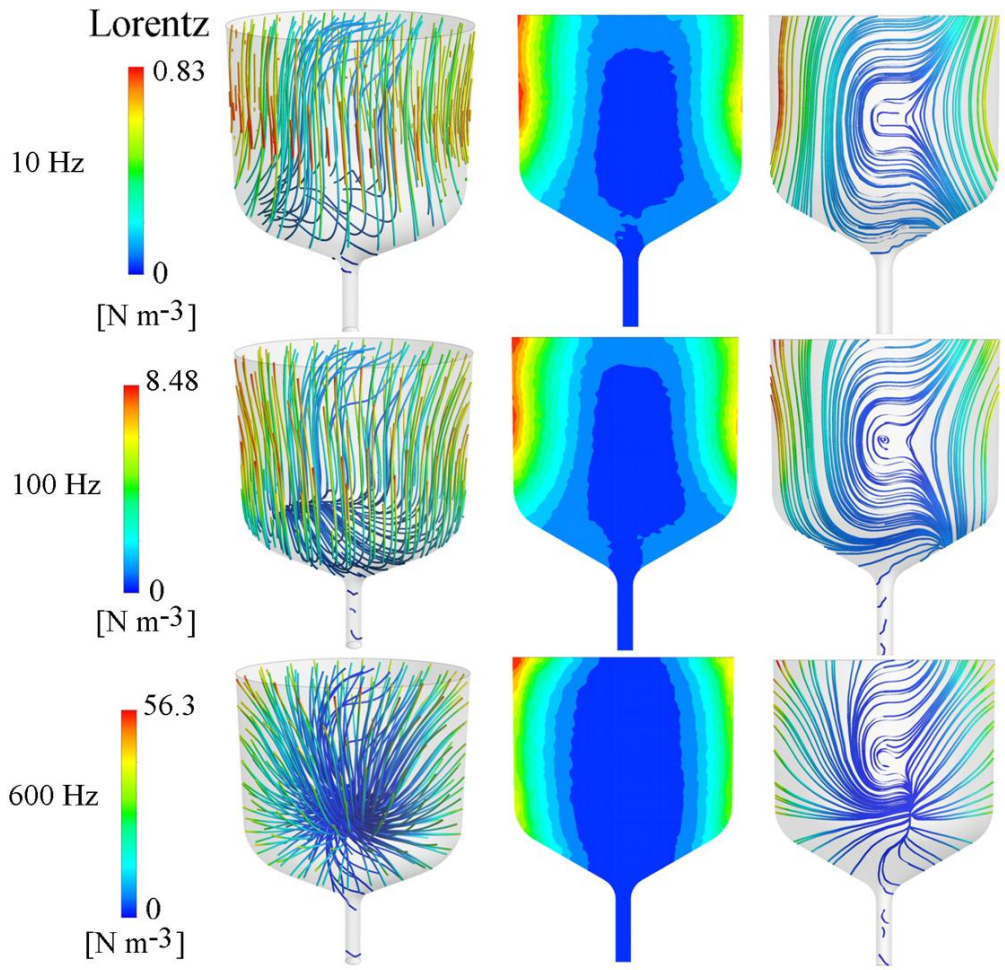

Figure 5.3: Numerical simulation of the Lorentz force density distribution in the melt inside the Kronos single-crucible setup as a function of frequency f for a melt mass of 5 kg and a constant downwards-directed single-frequency TMF: 3D streamlines, 2D contour in central longitudinal cross section, 2D streamlines in central longitudinal cross section [Dro14b]

through the temporary change of convection revealed the interface shape of the single high-frequency TMF(f_2) (dotted line). The stepwise return to the initial double-frequency TMF induced striations and the interface shape changed. Convexity in the center increased, the interface near the crystal edge (area B) was remelted. The bending near the crucible wall for TMF(f_2) could therefore not be visualized. The last visible striation corresponded to the w-shaped interface of the double-frequency TMF(f_1,f_2) (broken line), which remained unchanged after that (area C). The lower frequency TMF(f_1) with its larger penetration depth bended the interface in the center more convex. Here, force action dominated in the central region.

Exp.	I_{tot}	f_1, f_2	I_1/I_2	ϕ_1, ϕ_2	B_0	$\mathrm{Ta}_{m,1}$, $\mathrm{Ta}_{m,2}$
1f	61 A	10 Hz		90°	2.1 mT	6.12×10^5
2f	72 A	10 Hz, 100 Hz	0.84/0.16	80°, 120°	1.8 mT	2.65×10^5, 9.60×10^4

Table 5.1: TMF parameters used for comparison of single- and double-frequency process

Two crystals were grown to compare growth processes with only a single low-frequency and a double-frequency TMF. They were grown under same conventional growth conditions. TMF parameters were constant during growth. They were optimized for best possible interface morphologies for each process (see table 5.1). In Fig. 5.4 interface shapes are compared. The crystal grown with single low-frequency TMF(f_1) has a flat, slightly w-shaped and symmetric interface in the cylinder with a strong rising deflection near the periphery. The second crystal grown with double-frequency TMF(f_1,f_2) had a nearly flat interface in the lower section of the cylinder, with a rising w-shape and slight asymmetry in the upper cylinder section. Fig. 5.5 shows the quantitative comparison of the average deflection and β-angle for both crystals. Although TMF(f_1) was somewhat stronger, the interface deflection was on average larger compared to the crystal grown with TMF(f_1,f_2). Here, distribution of the Lorentz force was better matched to the natural interface shape. In the cylinder area the average deflection was reduced by about 22% with this double-frequency TMF compared to optimized single low-frequency TMF. In particular the important β-angle increased with the employment of a second high-frequency field. Along the whole crystal length the angle increased by an average of 12%.

Only a well-adjusted combination of low and high frequencies reduced the peripheral deflection. To find indications about the optimal ratio between low- and high-frequency TMF induced Lorentz force, two crystals were compared (table 5.2). In the first crystal, only 8% of the current was utilized for high-frequency TMF, in the second crystal it was 20%, resulting in a decreasing $\mathrm{Ta}_{m,1}$ number by a quarter and multiplied $\mathrm{Ta}_{m,2}$ number by nearly six. Total current, phase shift and total magnetic flux density were constant and identical in both cases. Crystal masses were 5 and 7 kg, respectively. Each lower crystal part was grown with reduced I_{tot}.

Fig. 5.6 shows the marked interface shapes of both crystals. The first markers were very similar because of the rather weak field at the beginning. Differences of the

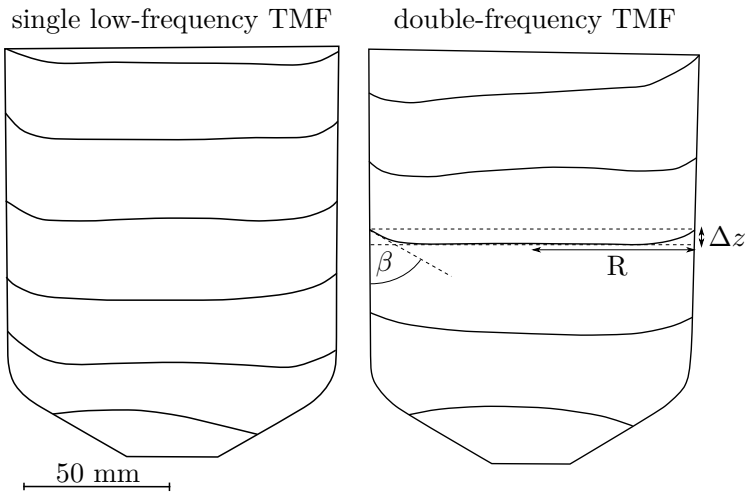

Figure 5.4: Comparison of the marked interface shapes of two crystals grown with single low-frequency and a double-frequency TMF, respectively, in the right picture the interface deflection $\Delta z/R$ and the β-angle are drawn in

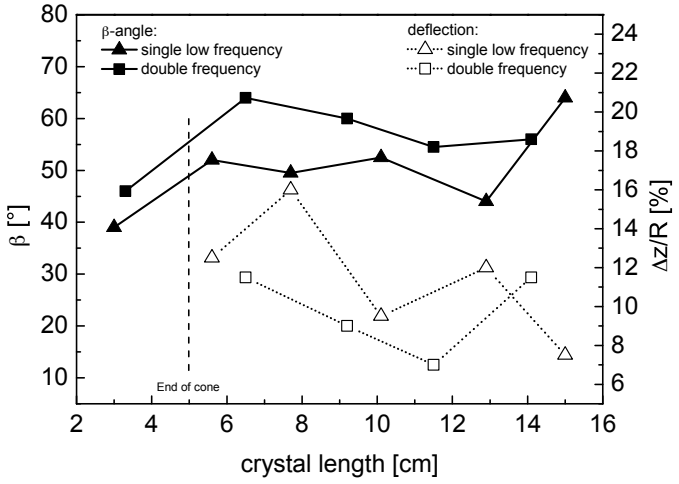

Figure 5.5: Measured values for the average deflections and β-angles for both crystals grown with single low-frequency and a double-frequency TMF, respectively

Exp.	I_{tot}	f_1, f_2	I_1/I_2	ϕ	B_0	$\mathrm{Ta}_{m,1}$, $\mathrm{Ta}_{m,2}$
sm. f_2 share	30 A	20 Hz, 200 Hz	0.92/0.08	90°	1.1 mT	2.51×10^5, 1.90×10^5
	45 A	20 Hz, 200 Hz	0.92/0.08	90°	1.6 mT	5.64×10^5, 4.27×10^5
lar. f_2 share	30 A	20 Hz, 200 Hz	0.8/0.2	90°	1.1 mT	1.90×10^5, 1.19×10^5
	45 A	20 Hz, 200 Hz	0.8/0.2	90°	1.6 mT	4.27×10^5, 2.67×10^5

Table 5.2: Parameters of two crystals grown with small and large high frequency share, but same total magnetic flux density

interface shape became more apparent with increasing AC. The pronounced inner concavity for the small high frequency share and the resulting almost flat w-shape of the interface disappeared with increasing high frequency share. Here, the interface shape had a similar average deflection, but showed enhanced asymmetry.

The consequence of this asymmetry is obvious when the measured deflections and β-angles are compared (Fig. 5.7). The asymmetry of the crystal with the large high frequency share led to slightly smaller β-angles and higher values of the average deflection in the central area of the crystals. The high frequency share had only an apparent positive effect on deflection and contact angle in the rear end of the crystal.

Consequently, strong high-frequency TMF were responsible for asymmetries of the solid-liquid interface. These asymmetries gave rise to one-side increase of deflection and the β-angle, which had unfavorable effects on the crystal properties (see section 6.1.4). The experimentally observed asymmetries were caused by radial and azimuthal deviations of Lorentz force density and temperature distribution in the HMM, which are enforced when high-frequency TMF are used [Kas08]. Their origin lay in the rotational asymmetry of the HMM, i.e. the current supply terminals of the coils.

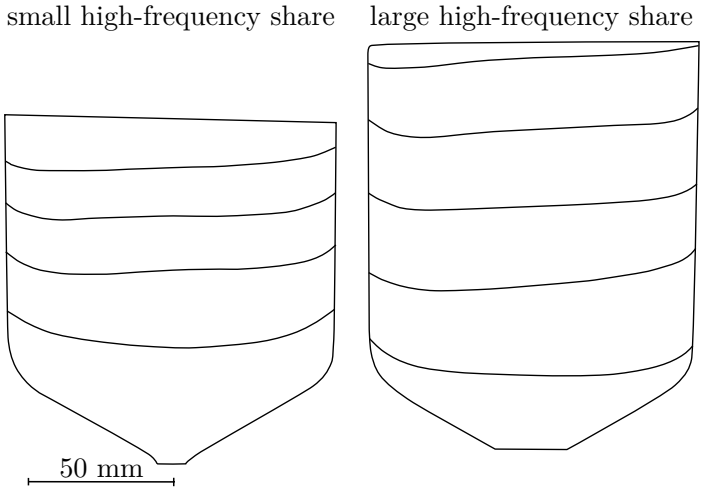

Figure 5.6: Comparison of interface shapes of two crystals grown with small and large high frequency share, but same total magnetic flux density

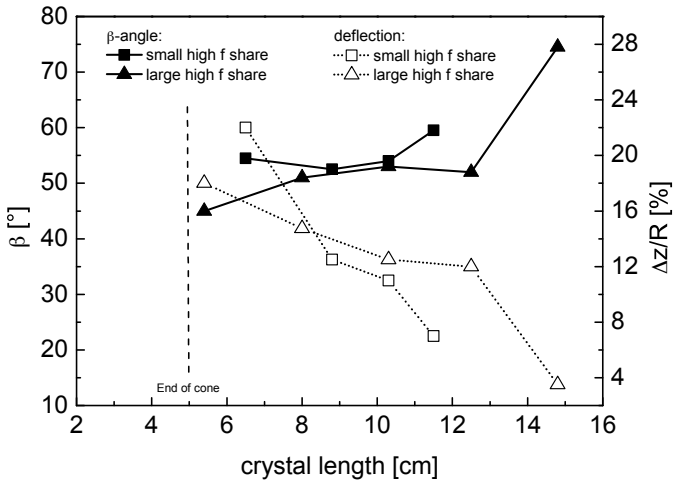

Figure 5.7: Measured values for the average deflections and β-angles for crystals grown with small and large high frequency share with same total magnetic flux density

5.1.2 TMF phase shift

A modification of the phase shift ϕ between the HMM coils changes magnitude, spatial distribution and direction of the Lorentz force in the melt. Results from numerical simulations are depicted in Fig. 5.8. The Lorentz force density distribution in the melt inside the Kronos single-crucible setup was investigated as a function of ϕ for a melt mass of 5 kg and a constant downwards-directed single-frequency TMF. The magnitude of F_L decreased with an increase of phase shift. It more than halved when ϕ changed from 60° to 120°. Spatial distribution and direction of F_L changed just as significantly. While for ϕ=60° the force direction was nearly horizontal to the interface, for ϕ=100° force direction was almost vertical to the growth front. For ϕ=120° the maximum of F_L was displaced to the melt top and its directions strongly varied for different vertical melt positions.

I_{tot}	f_1, f_2	I_1/I_2	ϕ	B_0	$\mathrm{Ta}_{m,1}$, $\mathrm{Ta}_{m,2}$
60 A	20 Hz, 200 Hz	0.92/0.08	60°	3.1 mT	3.35×10^6, 2.53×10^5

Table 5.3: Parameters of the double-frequency TMF for the crystal grown with a phase shift of 60°

A growth experiment was carried out with ϕ=60°. The TMF parameters are listed in table 5.3. The interface was extensively marked to investigate the progression of interface shape change with the altered force direction and to compare it with previous experiments. The result is shown in Fig. 5.9. The interface shape was highly asymmetric and a strong w-shape developed with progressing growth. It led to one-sided very large β-angles. The direction of the Lorentz force needed to be as vertical to the interface as possible to reduce the natural concavity of the solid-liquid interface. Phase shifts around 90-100° were therefore more suitable (see resulting interface shapes of the previous section).

Another possible setting option is the usage of a non-uniform phase shift between the three HMM coils, resulting in a modulated TMF wavelength. Numerical simulations were carried out to compare the impact of non-uniform phase shifts on the Lorentz force density distribution. Fig. 5.10 shows the results for comparison of uniform phase shift (ϕ=100°) and non-uniform phase shift (ϕ_1=80° between bottom coil H4 and center coil H3 and ϕ_2=120° between center coil H3 and upper coil H2) for a melt mass of 5 kg and a constant downwards-directed double-frequency TMF. Distribution and magnitude of F_L changed, while the direction of the Lorentz force was in both cases very similar. The maximum of F_L dropped by about 20% in case of non-uniform phase shift. Furthermore, for a uniform phase shift the position of the maximum was in the center area of the cylinder along the crucible wall. In case of a non-uniform phase shift the maximum was moving to the upper melt rim, preventing strong asymmetries in the central cylinder area.

Consequences of these modifications on the shape of the solid-liquid interface were experimentally studied. Two crystals were grown under identical conventional growth conditions and the same TMF parameters used for the numerical simulations.

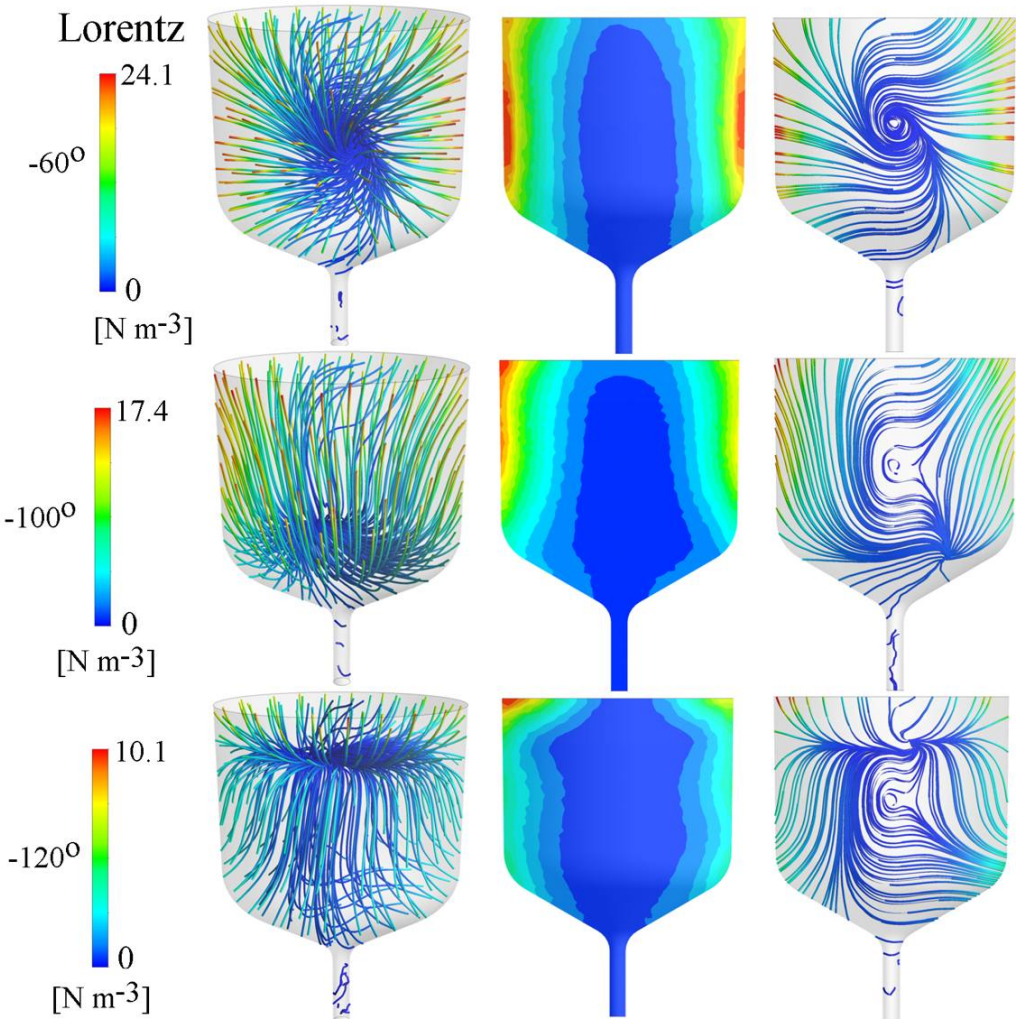

Figure 5.8: Numerical simulation of the Lorentz force density distribution in the melt inside the Kronos single-crucible setup as a function of phase shift ϕ for a melt mass of 5 kg and a constant downwards-directed single-frequency TMF: 3D streamlines, 2D contour in central longitudinal cross section, 2D streamlines in central longitudinal cross section [Dro14b]

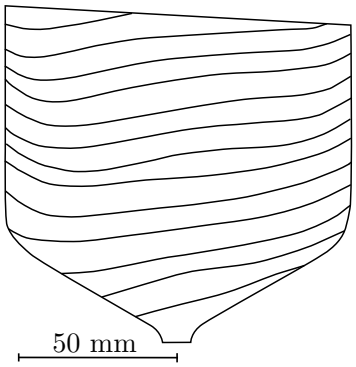

Figure 5.9: Crystal grown with a phase shift of 60°, extensive interface marking shows the progression of the asymmetric interface shape

All TMF parameters were identical except from the respective uniform and non-uniform phase shifts (see table 5.4).

Exp.	I_{tot}	f_1, f_2	I_1/I_2	ϕ_1, ϕ_2	B_0	$\mathrm{Ta}_{m,1}$, $\mathrm{Ta}_{m,2}$
$\phi_1{=}\phi_2$	72 A	10 Hz, 100 Hz	0.84/0.16	100°	2.1 mT	$3.73{\times}10^5$, $1.35{\times}10^5$
$\phi_1{\neq}\phi_2$	72 A	10 Hz, 100 Hz	0.84/0.16	80°, 120°	1.8 mT	$2.65{\times}10^5$, $9.60{\times}10^4$

Table 5.4: Parameters of the TMF used for growth experiments for comparison of uniform and non-uniform phase shift between the HMM coils

Resulting interface shapes of both crystals are shown in Fig. 5.11. The corresponding measured values are displayed in Fig. 5.12. The crystal with the uniform phase shift had somewhat higher interface deflections and a more pronounced w-shaped interface in the upper cylinder region. Here, Lorentz forces were slightly too strong. The w-shape in the second crystal with non-uniform phase shift was less pronounced and the concavity was more regular, resulting in desired higher β-angles. Reason for this was the shift of the maximum magnitude of F_L to the top melt region.

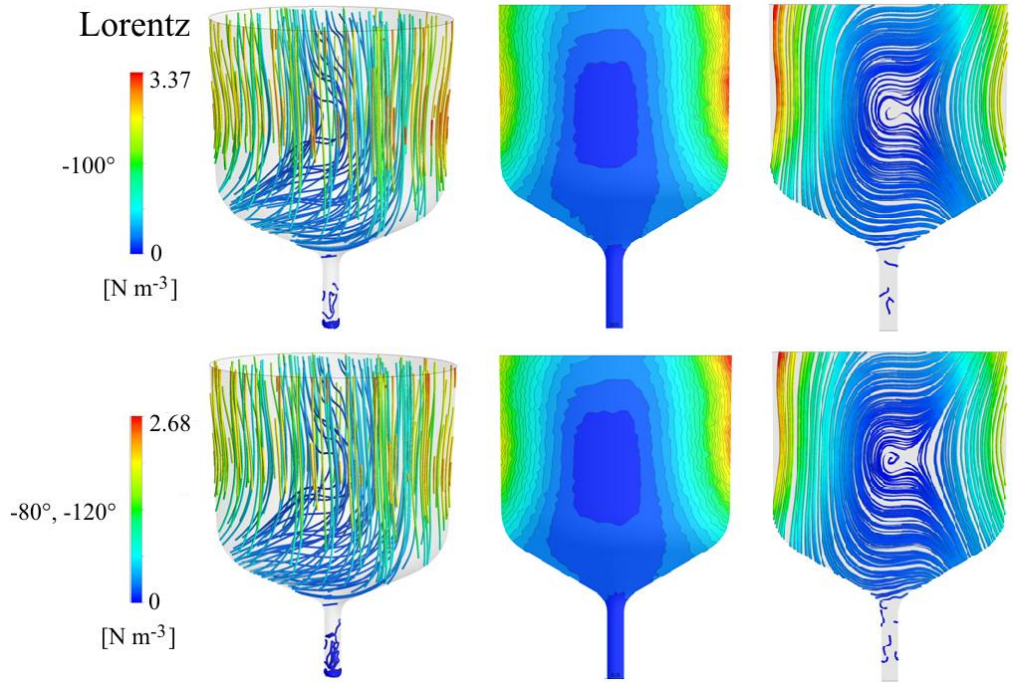

Figure 5.10: Numerical simulation of the Lorentz force density distribution in the melt inside the Kronos single-crucible setup for comparison of uniform phase shift ϕ=100° and non-uniform phase shift ϕ_1=80° between bottom coil H4 and center coil H3 and ϕ_2=120° between center coil H3 and upper coil H2 for a melt mass of 5 kg and a constant downwards-directed double-frequency TMF with I_{tot}=72 A, f_1=10 Hz, f_2=100 Hz, I_1/I_2=0.84/0.16: 3D streamlines, 2D contour in central longitudinal cross section, 2D streamlines in central longitudinal cross section [N. Dropka, IKZ Berlin]

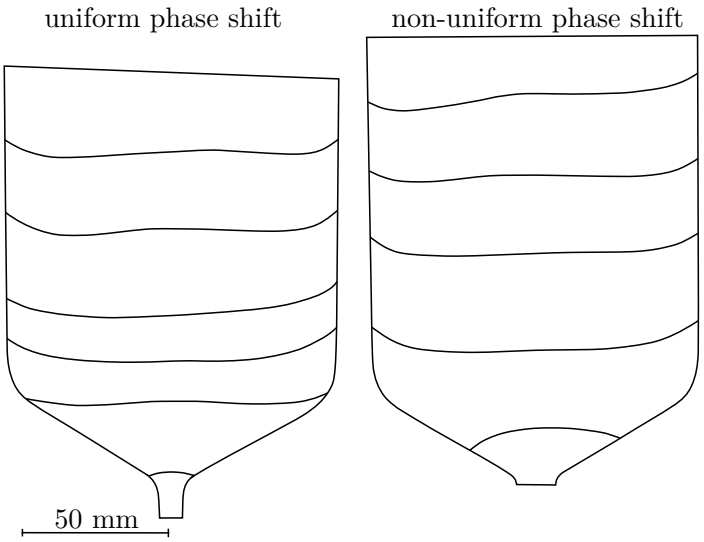

Figure 5.11: Comparison of the shape of the solid-liquid interface of two crystals grown with uniform phase shift of ϕ=100° and non-uniform phase shift ϕ_1=80°, ϕ_2=120° between HMM coils, respectively

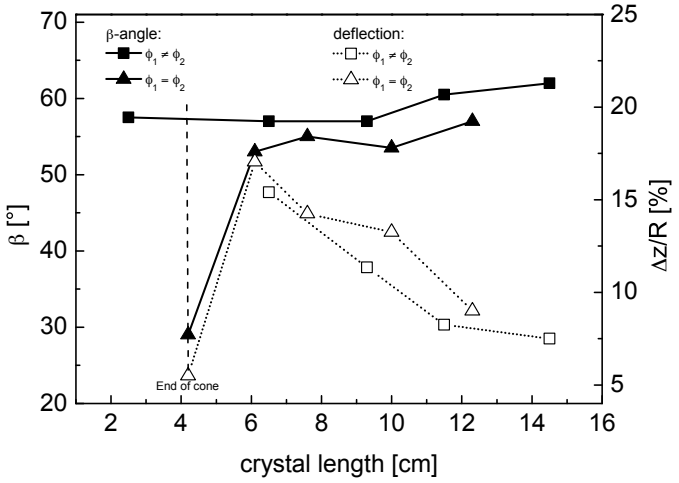

Figure 5.12: Measured values for the average deflections and β-angles for both crystals grown with uniform phase shift of ϕ=100° and non-uniform phase shift ϕ_1=80°, ϕ_2=120° between HMM coils

5.1.3 TMF current

Increasing the AC results in a quadratic increase of the Lorentz force magnitude. The force direction, penetration depth, and spatial distribution do not change. Fig. 5.6 shows not only the comparison between a small and a large high frequency share of a double-frequency TMF, but also the impact of various currents. The respective first marker represents growth with AC of I_{tot}=30 A, the other markers growth with I_{tot}=45 A. The force magnitude more than doubled. The first marker with the small force magnitude showed only a little effect on the interface deflection. Regardless whether high or low frequency current, the magnitude of the Lorentz force needed to exceed a value of around 1.5 mT for an interface shaping potential. Natural concave deflection was not or only slightly reduced when the AC was small.

Step	I_{tot}	f_1, f_2	I_1/I_2	ϕ	B_0	$\mathrm{Ta}_{m,1}$, $\mathrm{Ta}_{m,2}$
1	72 A	10 Hz, 100 Hz	0.84/0.16	100°	2.1 mT	3.73×10^5, 1.35×10^5
2	98 A	10 Hz, 100 Hz	0.62/0.38	100°	2.8 mT	3.76×10^5, 1.41×10^6
3	85 A	10 Hz, 100 Hz	0.62/0.38	100°	2.5 mT	2.83×10^5, 1.06×10^6

Table 5.5: Parameters of the double-frequency TMF for a crystal grown with increasing AC during growth to investigate interface morphologies in the crystal periphery with increasing strength of the high-frequency TMF and critical AC threshold

A crystal was grown to investigate the effects on the interface morphology with further increasing currents and the critical AC threshold for time-dependent melt flow (table 5.5). In particular, the current of the high-frequency TMF was increased to study their ability of flattening the interface in the crystal periphery. The result is displayed in Fig. 5.13 and features distinct interface changes. The first growth step is represented by the first two markers (solid lines). Average well-adjusted TMF parameters led to a slightly convex interface shape in the crystal cone and a reduced concave deflection at the beginning of the cylinder. In step two the current was significantly increased and the AC shares of TMF(f_1) and TMF(f_2) were adjusted. The Lorentz force of TMF(f_1) was held constant and the force of TMF(f_2) was increased by an order of magnitude (see Ta_m numbers). This growth regime is depicted by markers 3 to 6 (dotted lines). Force enhancement resulted in highly asymmetric interface shapes with high concave deflection. The second interface marker even melted back through the strong asymmetric convective flow. Furthermore, the critical Lorentz force was exceeded, the melt flow became time-dependent. Regular striations were observed (see section 6.1.1). The negative TMF influence ultimately led to start of polycrystalline growth. In step 3 (broken line, markers 7 and 8) Lorentz force was reduced for both frequencies by 25%. This resulted in a more symmetric interface shape with a still very high interface deflection. In this area, striations were still visible. The overcritical Lorentz forces were still exceeded.

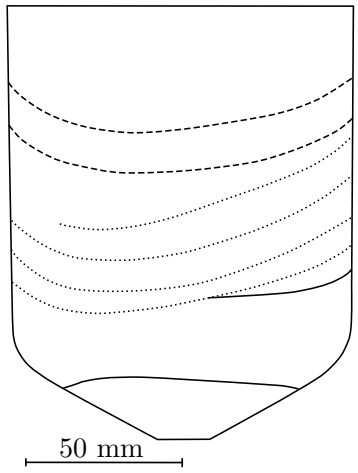

Figure 5.13: Interface shape markers of a crystal grown with three different currents, all other TMF parameters were constant (see table 5.5): solid lines - step 1, dotted line - step 2, broken line - step 3

5.2 Matching of TMF parameters with advancing solidification

As results from conducted experiments with steady magnetic fields during the growth process revealed, the impact of the TMF on the melt flow and the shape of the solid-liquid interface differed with the progression of the solidification. Asymmetries, strong w-shaped interfaces, and time-dependent flow have to be strictly avoided for consistently good crystal quality. A continuous adjustment of the TMF parameters is therefore inevitable. Fig. 5.14 shows results from numerical simulations of the Lorentz force density distribution as a function of progressing solidification. The melt mass was 5 kg and a constant downwards-directed single-frequency TMF acted inside the single-crucible Kronos setup. 2D and 3D streamlines and the 2D contour of the central longitudinal cross section showed changing Lorentz force density distributions with advancing growth. In the crucible cone, the streamlines were mainly horizontal and therefore the generated Lorentz forces only mildly contributed to solid-liquid interface shaping. In the cylinder, streamlines were primarily downwards-directed and therefore the interface shaping potential was high in this area. With progressing growth, the spatial distribution of the F_L was generally preserved in a compressed form, but the magnitude of the Lorentz force distribution slightly increased. Experimental findings of the TMF parameter studies confirmed that the TMF effect on the interface shape in the cone area is weak. Here, the interface morphology was mainly influenced by thermal insulation and crucible support. Furthermore, with decreasing melt volumes in the cylinder area, the shaping effect

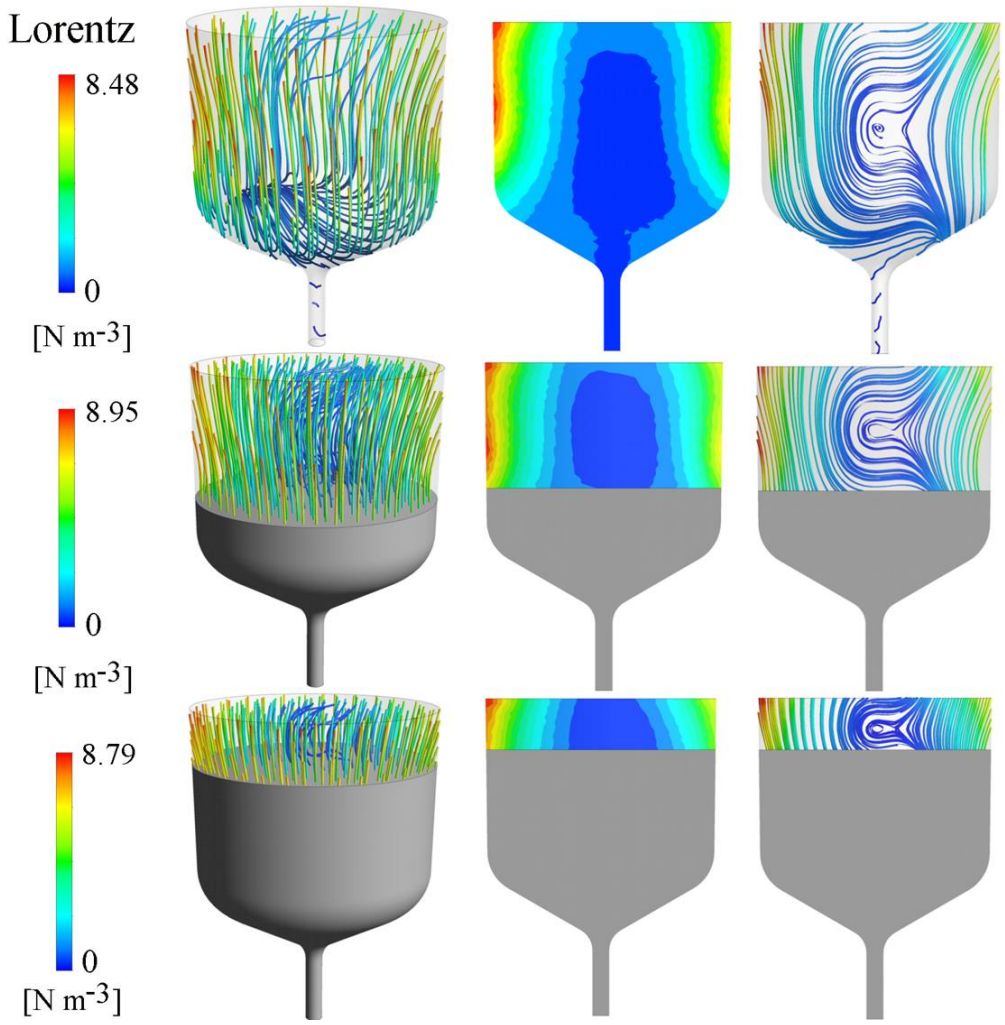

Figure 5.14: Numerical simulation of the Lorentz force density distribution in the melt inside the Kronos single-crucible setup as a function of progressing solidification for a melt mass of 5 kg and a constant downwards-directed single-frequency TMF: 3D streamlines, 2D contour in central longitudinal cross section, 2D streamlines in central longitudinal cross section [Dro14b]

Step	I_{tot}	f_1, f_2	I_1/I_2	ϕ_1, ϕ_2	B_0	$\mathrm{Ta}_{m,1}$, $\mathrm{Ta}_{m,2}$
1	72 A	10 Hz, 100 Hz	0.84/0.16	80°, 120°	1.8 mT	2.65×10^5, 9.60×10^4
2	76 A	10 Hz, 100 Hz	0.84/0.16	80°, 120°	1.9 mT	2.95×10^5, 1.07×10^5
3	72 A	10 Hz, 100 Hz	0.84/0.16	80°, 120°	1.8 mT	2.65×10^5, 9.60×10^4
4	68.7 A	10 Hz, 100 Hz	0.84/0.16	80°, 120°	1.7 mT	2.41×10^5, 8.74×10^4
5	63 A	10 Hz, 100 Hz	0.84/0.16	80°, 120°	1.5 mT	2.02×10^5, 7.35×10^4

Table 5.6: First matching experiment: TMF parameters of the growth-matched double-frequency TMF with adjusted I_{tot}

Step	I_{tot}	f_1, f_2	I_1/I_2	ϕ_1, ϕ_2	B_0	$\mathrm{Ta}_{m,1}$, $\mathrm{Ta}_{m,2}$
1	63 A	10 Hz, 100 Hz	0.73/0.27	80°, 120°	1.5 mT	1.53×10^5, 2.09×10^5
2	63 A	10 Hz, 100 Hz	0.70/0.30	80°, 120°	1.5 mT	1.41×10^5, 2.58×10^5
3	63 A	10 Hz, 100 Hz	0.73/0.27	80°, 120°	1.5 mT	1.53×10^5, 2.09×10^5
4	63 A	10 Hz, 100 Hz	0.76/0.24	80°, 120°	1.5 mT	1.65×10^5, 1.65×10^5
5	63 A	10 Hz, 100 Hz	0.84/0.16	80°, 120°	1.5 mT	2.02×10^5, 7.35×10^4

Table 5.7: Second matching experiment: TMF parameters of the growth-matched double-frequency TMF with adjusted frequency shares and constant I_{tot}

increased with steady TMF, the Lorentz force density was larger in the upper melt region.

Two growth experiments under standard growth conditions were conducted based on the conditions described before for optimization of the interface morphologies with TMF application and the need to match the magnitude of the Lorentz forces to the solidification process. First approach was to use the already well-adjusted steady double-frequency TMF with a non-uniform phase shift (see interface in Fig. 5.11 (right)) and match the total AC current I_{tot} to every growth phase of the five marker areas. Aim was to obtain consistently flat/slightly convex interface shapes. Through adjusting the total current, a Lorentz force with a steady magnitude near the interface should be obtained. The TMF parameters are displayed in table 5.6. Only I_{tot} was adjusted, all other TMF parameters were held constant during the growth process.

As it can be seen in Fig. 5.11 (right), the first and the third marker were already well optimized. The TMF at the second marker was rather weak, and in marker four and five the w-shape was strong and asymmetries arose. Therefore, based on I_{tot}=72 A and the simulated Lorentz force density distribution with increasing values from bottom to top, the AC current was adjusted. Hereafter, in the area of the second marker F_L was increased by 10%, decreased by 10% in the area of the fourth marker and decreased by 25% in the cylinder end in the area of the fifth marker. The AC adjustment always related to the initial 72 A and the respective sum of $\mathrm{Ta}_{m,1}$ and $\mathrm{Ta}_{m,2}$. The adjustment of the current during growth was performed between the markers with an alteration rate of 1 A/h.

In a second approach, the effect of matching the TMF parameters to the growth was analyzed with respect to the aim of further decreasing the local deflection near the crucible wall. Here, a larger current share of the higher frequency compared to the first matching approach was applied. The TMF parameters are displayed in table 5.7.

Frequencies and phase shifts were identical to the first approach in this second matching experiment (table 5.6). But now I_{tot} was held steady and only the respective current shares between 10 Hz and 100 Hz were adjusted in again five steps. The resulting TMF were of magnetical similarity compared to the first matching experiment, i.e. the sum of the magnetic Taylor numbers was identical in both growth experiments. Only the larger current share of the high-frequency TMF should increase the Lorentz force action in the melt periphery in the lower cylinder in the second experiment. The matching procedure of the Lorentz force density to the growth process again followed the same approach, based on the interface of Fig. 5.11 (right). In the area of the second marker F_L is increased by 10%, in the area of the fourth marker decreased by 10% and decreased by 25% in the area of the fifth marker. The adjustment of the current shares during growth was performed within the same timeframe of the first matching experiment.

Fig. 5.15 shows the solid-liquid interface shapes of the crystals grown in the two matching experiments (please note: the frequency-share-matched crystal was polycrystalline in the upper left cylinder due to a non-TMF-related strong excess of gallium in the GaAs feedstock, the interface shape in this area was therefore not accessible). Compared to Fig. 5.11 (right) the asymmetry and strong w-shape vanished in both crystals. In particular the current-matched crystal showed a uniform interface morphology with a flat center. The measured values of average deflections and β-angles of the crystal with steady TMF and both growth-matched crystals are compared in Fig. 5.16. The average deflections for steady and current-matched TMF were nearly identical, while maximum deflection of the frequency-share-matched crystal was higher. Here, the β-angles were on average the smallest, too. An increase of the high-frequency AC share did not have a flattening effect on the interface near the crucible wall. The more vertical Lorentz forces acting in the melt periphery with lower frequencies (see Fig. 5.3) seemed to have a larger impact on the interface morphology than the increase of the Lorentz force density with increasing high-frequency share. An increase of the magnitude of F_L near the crucible wall was only useful if the force direction was vertical to the respective interface shape. Most advantageous was the current-matching of the TMF to prevent asymmetric and w-shaped interfaces, which resulted in comparative large β-angles. However, a further reduction of the crucible-near concave bending was not obtained.

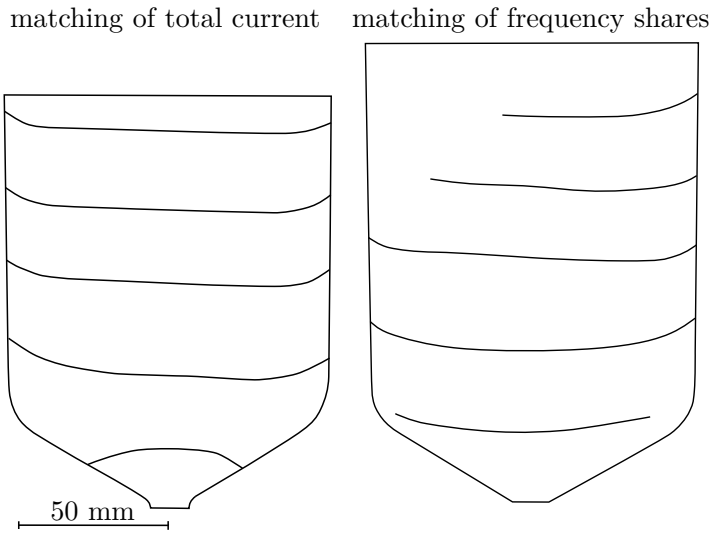

Figure 5.15: Comparison of the two growth-matched crystals: (left) solid-liquid interface of the crystal grown in the first growth-matching experiment with matching of the total current, (right) solid-liquid interface of the crystal grown in the second growth-matching experiment with matching of the frequency shares with steady total current

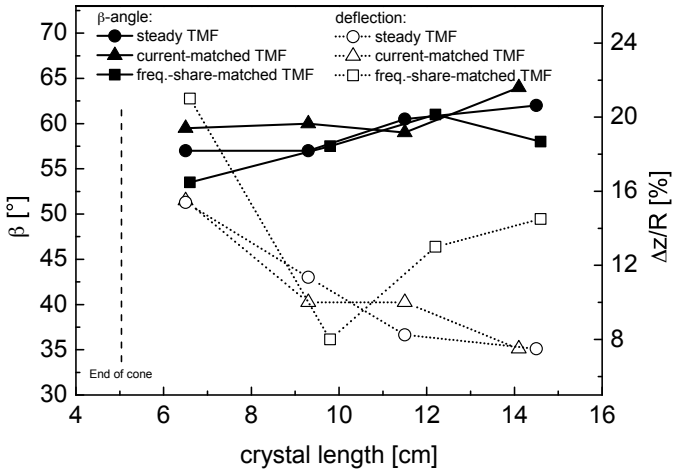

Figure 5.16: Measured values of average deflections and β-angles of the reference crystal with steady TMF parameters, the crystal grown with matching of the total current, and the crystal grown with matching of the frequency shares with steady total current

5.3 Comparison of VGF growth with/without TMF

A crystal was partially grown without the utilization of a TMF. The growth process was a reproduction of the current-matching experiment. The same conventional growth parameters were applied, but the TMF was only switched on five times for 180 minutes each time. During crystallization the magnetic flux density decreased from B_0=1.8-1.5 mT by decreasing the AC with decreasing melt height. In each of the five TMF areas the parameters used in the previous current-matching experiment were used sequentially. Each of the five steps is illustrated in table 5.6 in the previous section. The interface deflection was marked by short 15-minute-remelting

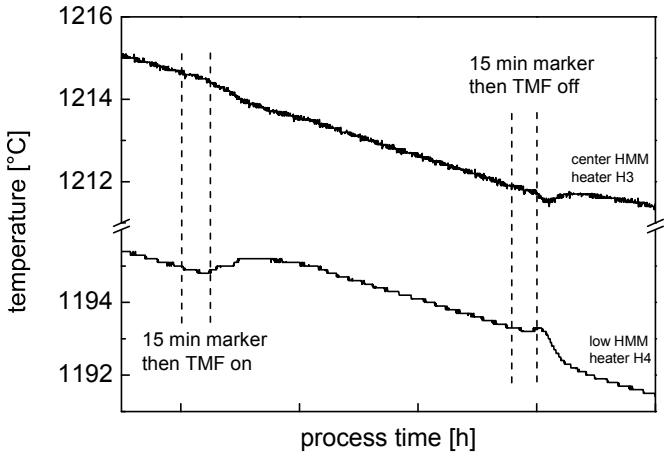

Figure 5.17: Temperature progression measured with thermocouples near the center HMM heater H3 and the lower HMM heater H4 during switching on of the TMF

before and after switching on the steady TMF for 150 minutes. Fig. 5.17 shows the progression of the temperatures near the center HMM heater H3 and the lower HMM heater H4 in the first TMF area. During the short marking time the temperature progression was hardly influenced. After switching on the TMF with steady parameters, the temperature increased at the interface near H4 and decreased in the upper melt region, represented by H3. The downwards-directed Lorentz force led to a constant transport of melt with a higher temperature from the upper region to the interface. Both cooling rates were again comparable to the non-TMF case after about 20-30 minutes of force action, but on a slightly higher and lower temperature level, respectively. Temperature progression behaved inversely after switching off the TMF. After 20-30 minutes of enhanced temperature decrease near the interface and increase in the upper melt, cooling rates were steady again on the same level before the TMF was switched on. Hence, the influence of the TMF on the melt flow with enhanced vertical melt mixing was observed through temperature variations at different thermocouples during growth.

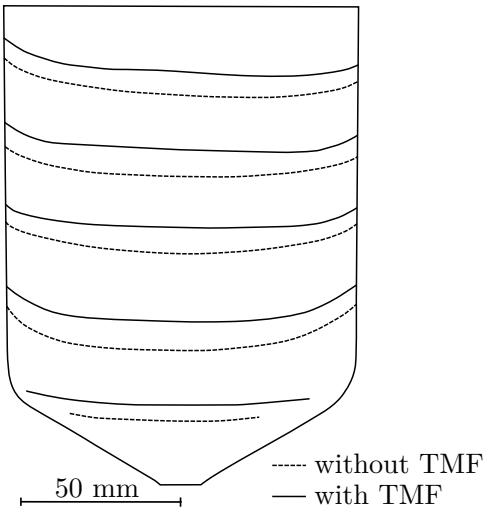

Figure 5.18: Interface shape of the crystal grown partially with a TMF, the dotted line represent the interface morphology without TMF and the solid line with TMF

Fig. 5.18 shows the shape of the solid-liquid interface with and without TMF, respectively. A decrease of the concave deflection along the whole crystal length was observed. Switching-on the TMF intensified heat exchange away from the interface, resulting in reduced radial gradients and hence, decreased deflection of the interface. Growth-matching of the TMF parameters provided a stable interface shape with a flat center and only minor asymmetry. This asymmetry was assumed to be caused by the slightly non-uniform thermal field and not by the TMF, due to the fact that also the interface without TMF was tilted. A minor interface asymmetry was therefore present in all growth experiments in the single-crucible setup, independent from the applied TMF parameters. Corresponding measured values of average deflections and β-angles in the crystal cylinder are depicted in Fig. 5.19. The average reduction of the interface deflection lays in the range of stable 30% along the whole crystal length. The increase of the β-angle was lower with an average reduction of around 10% with the application of a TMF. In all cases, the decrease of the deflection was accompanied by the increase of the crucible contact angle.

In Fig. 5.20 the measured values of deflection and β-angle of two crystals, grown separately with identical conventional growth conditions and a reduced growth velocity of v_{gr}=1.5 mm/h, are compared: A reference crystal grown without TMF and a crystal grown with a steady double-frequency TMF of B_0=0.9 mT. The power distribution inside the furnace differed slightly from the standard process. The reached reduction of interface deflection and the increase of the β-angle lay in the same order with around 30% deflection reduction and more than 10% increased β-angle in the

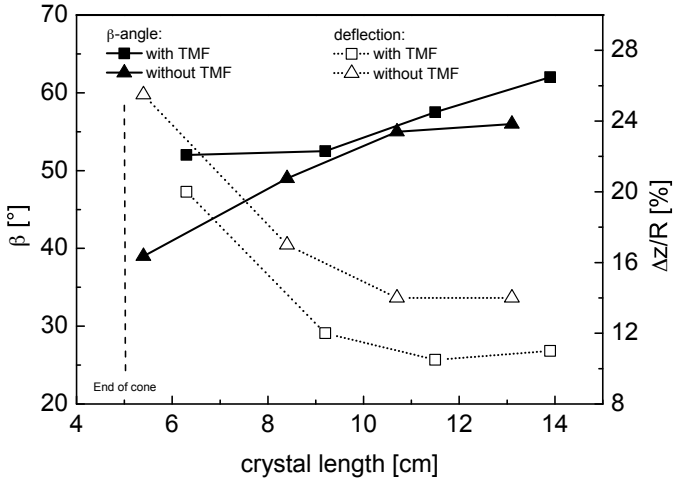

Figure 5.19: Measured values of average deflections and β-angles for the crystal only partially grown with TMF in a standard growth process with v_{gr}=2.5 mm/h

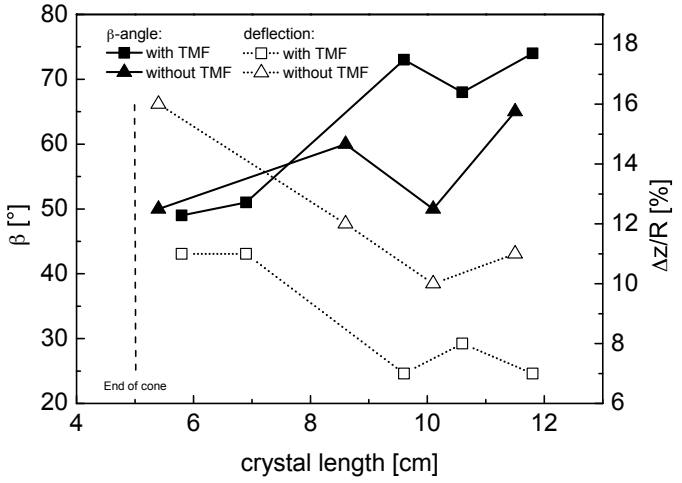

Figure 5.20: Measured values of average deflections and β-angles for the reference crystal grown without TMF and a crystal grown under the same growth conditions with a steady double-frequency TMF of B_0=0.9 mT and respective growth velocity of v_{gr}=1.5 mm/h

upper cylinder region. The progression of the curves was very similar to the other growth experiment.

In summary, the deflection of the interface was reduced and the β-angle was increased under the influence of a double-frequency TMF. However, the best possible interface shape highly depended on global thermal conditions, too. They were adjustable by conventional crystal growth parameters, like growth velocity, thermal insulation, materials, and further on. Striking was the fact, that with the utilization of a TMF an additional tool was provided to reduce the interface deflection even further.

5.4 Utilization of a BN susceptor

The application of a TMF offered a good possibility to minimize the concave deflection of the interface by about 30%. In fact, even flat/ slightly convex interfaces near the crystal axis were possible with well adjusted TMF parameters. However, the area very close to the crucible wall was significantly less influenced with a TMF. With a well-adjusted TMF the β-angle increased within the order of only 10%. The local curvature was mainly determined by the anistropic thermal conductivity of the pBN crucible. A further approach was, to decrease radial heat dissipation and to promote downwards-directed heat flow through the grown crystal with conventional methods. The utilization of a susceptor material with a lower thermal conductivity was tested to reduce the radial temperature gradients along the solid-liquid interface and to improve the local curvature near the crucible wall.

To study the susceptor influence, growth experiments with an isotropic BN susceptor were performed in the single-crucible growth setup. In chapter 4 the application of different susceptor materials and their influence on axial temperature gradients was described. Compared to the standard process with graphite susceptor, a BN susceptor provided enhanced axial temperature gradients in the cone and smaller axial temperature gradients in the cylinder area under identical heater powers and temperatures (see Fig. 4.4). In the first experiment, a standard growth process was conducted, only replacing the graphite susceptor by a BN susceptor resulting in the described axial gradient change. The cooling rate was adjusted to match the growth rate of around 2 mm/h. A steady double-frequency TMF with non-uniform phase shift was applied. It was identical to a growth experiment conducted with standard graphite susceptor (see table 5.4 and the related solid-liquid interface shape in Fig. 5.11). In the second growth experiment, heater settings were adjusted to reach the axial temperature gradients of the graphite susceptor in the cylinder of 2 K/cm. The axial temperature gradients in cone area were larger compared to the standard process. The new heater settings were transferred to the standard growth recipe and cooling rates correspondingly adjusted. A current-matched double-frequency TMF with non-uniform phase shift was applied, identical to a growth experiment conducted with standard graphite susceptor (see table 5.6 and the related solid-liquid interface shape in Fig. 5.15 (left)).

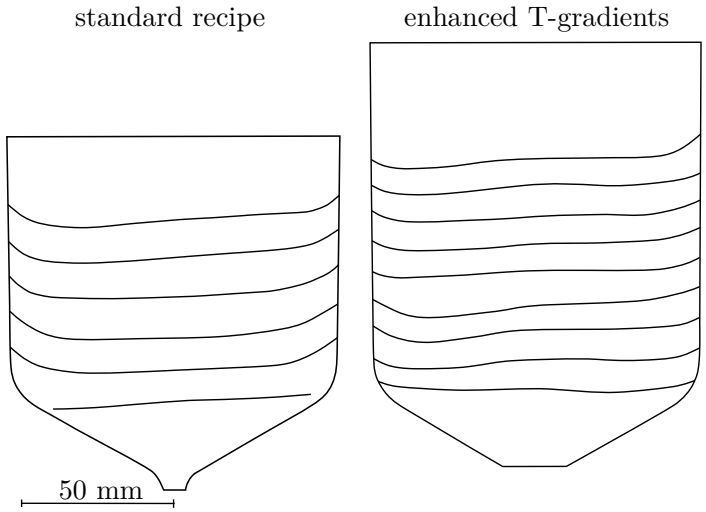

Figure 5.21: Comparison of two crystals grown with a BN susceptor: (left) crystal grown with standard recipe with slightly enhanced gradients in the cone area and reduced gradients in the cylinder compared to the graphite susceptor, (right) crystal grown with altered recipe with further enhanced gradients in the cone and identical gradients in the cylinder compared to standard graphite susceptor application

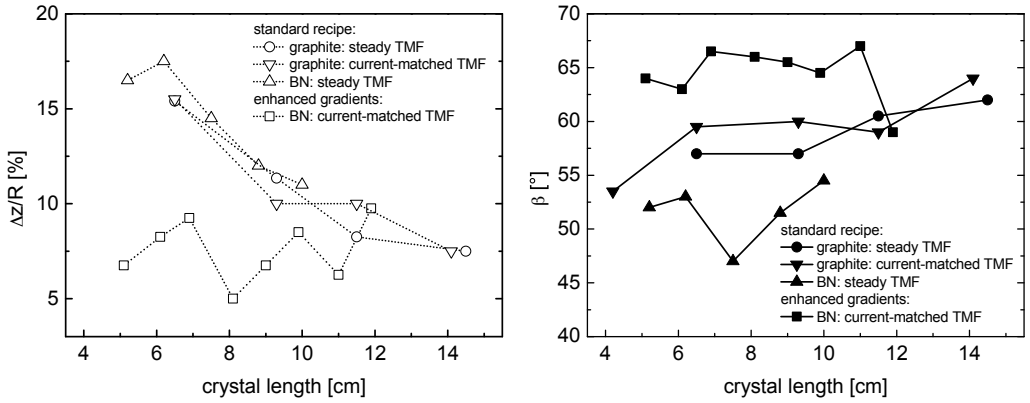

Figure 5.22: Measured values of average deflection and β-angles of the crystals grown with BN susceptor compared to grown crystals with respective TMF parameters and graphite susceptor utilization with standard growth recipe

The resulting interface shapes from both experiments are depicted in Fig. 5.21. Due to the adjustment of the growth recipes with the use of BN susceptors, in both crystals the measured growth rate was somewhat smaller with 1.7-1.9 mm/h compared to standard processes with the use of graphite as susceptor material. The crystal grown with standard recipe and steady TMF parameters was characterized by a regular flat interface in the center and a pronounced increase of the deflection towards the crucible walls. No distinct w-shape or asymmetry was found. The second crystal, grown with enhanced gradients and current-matched TMF, showed a slight w-shape and partial asymmetry in the lower and upper cylinder area. This was not detected in the relating crystal grown with standard graphite susceptor. It was caused by the enhancement of the TMF impact through the lack of shielding with the isolating BN susceptor. The solid-liquid interface shape in most areas was characterized by slightly convex center and pronounced reduction of the deflection near the crucible wall.

The measured values of the average deflections and β-angles of the crystals grown with BN susceptor are compared in Fig. 5.22. Additionally, the values for the respective crystals grown with standard graphite susceptor and identical TMF parameters are shown. The maximum deflection was not reduced through the utilization of the BN susceptor in the standard recipe with steady TMF. Values of deflection were nearly identical to the crystal grown with graphite susceptor. Furthermore, the replacement of the graphite susceptor had even a negative effect on the β-angle. Measured angles were significantly larger with BN susceptor. This was attributed to the reduced axial temperature gradients and associated decreased axial heat dissipation. The enhancement of axial temperature gradients to values of the standard process with graphite susceptor was accompanied by a drastic reduction of the deflection. In the cylinder center almost flat interfaces were achieved. The average deflection values were constantly smaller compared to all so far grown crystals, in particular in the lower cylinder area. The β-angles also exceeded the values of the other crystals.

The utilization of the new axial temperature gradient profile and the BN susceptor provided enhanced axial heat dissipation, especially in the cone and lower cylinder. The deflection near the crucible wall was further reduced. The Lorentz force provided by a well-adjusted and growth-matched TMF was better able to act more vertical to the interface. It resulted in a flat solid-liquid interface growing into the cylinder.

5.5 Process intensification combined with TMF application

In the following section, the application of TMF in combination with intensification approaches is described. First, scale-up and speed-up growth experiments of GaAs:Si with TMF were conducted in the single-crucible HMM. Preliminary findings from the TMF parameter study and growth-matching experiments were applied. Subsequently, the multi-crucible VGF setup was put into operation for the numbering-up approach. Parameter studies in the multi-crucible HMM were conducted. Results

on the simultaneous growth of two 4" VGF-GaAs:Si single crystals with an applied double-frequency TMF are shown.

5.5.1 Scale-up

The previous studies showed, that the application of a double-frequency TMF helps to efficiently remove heat from the interface and to reduce radial thermal gradients. This is of upmost importance for the growth of large GaAs single crystals, where the dissipation of latent heat with progressing growth through the increasing heat resistance of the growing crystal is the central issue. In the following, the effects of TMF application in a VGF-GaAs growth process with enhanced melt height are evaluated.

Again, numerical simulations were conducted. In Fig. 5.23 Lorentz force density distributions of a constant downwards-directed single-frequency TMF in the melt inside the Kronos single-crucible setup are shown as a function of the initial feedstock mass of 5 kg, 7 kg, and 9 kg, respectively. An increase of the feedstock load resulted in a significant change in Lorentz force density distribution, even if TMF parameters were kept constant. The magnitude of F_L significantly changed, while the spatial distribution was generally sustained in a stretched manner. F_L increased by 20-25% by increasing the melt mass. However, in the top melt region of a 9 kg load the influence of the TMF substantially weakened, due to the melt emerging out of the range of HMM.

These results were regarded in a growth experiment with a GaAs feedstock mass of 9.15 kg. Growth was conducted with the application of a BN susceptor and standard axial temperature gradients. The standard growth recipe was correspondingly prolonged, the cooling rate was kept steady. The growth rate was steady during growth with 1.8-2.2 mm/h. The growth process with a current-matched TMF oriented itself on the so far best experimental results from a 7 kg crystal with the lowest interface deflection and highest β-angles (see Figs. 5.21 and 5.22). The TMF parameters are shown in table 5.8. Increasing Lorentz force densities with increas-

Step	I_{tot}	f_1, f_2	I_1/I_2	ϕ_1, ϕ_2	B_0	$\mathrm{Ta}_{m,1}$, $\mathrm{Ta}_{m,2}$
1	72 A	10 Hz, 100 Hz	0.84/0.16	80°, 120°	1.8 mT	2.65×10^5, 9.60×10^4
2	68 A	10 Hz, 100 Hz	0.84/0.16	80°, 120°	1.7 mT	2.36×10^5, 8.56×10^4
3	60 A	10 Hz, 100 Hz	0.84/0.16	80°, 120°	1.5 mT	1.84×10^5, 6.67×10^4

Table 5.8: TMF parameters of the scale-up experiment with adjusted I_{tot}

ing melt mass were recognized, in addition to current-matching due to progressing solidification. To prevent asymmetries in the lower cylinder, current was not increased above 72 A. Current was first decreased to 68 A (compared to 68.7 A in the other current-matched experiment) and then further to 60 A (compared to 63 A beforehand). Current was not again increased in the upper cylinder area. Reason was the unclear effect of rising asymmetries for enhanced melt heights, although the

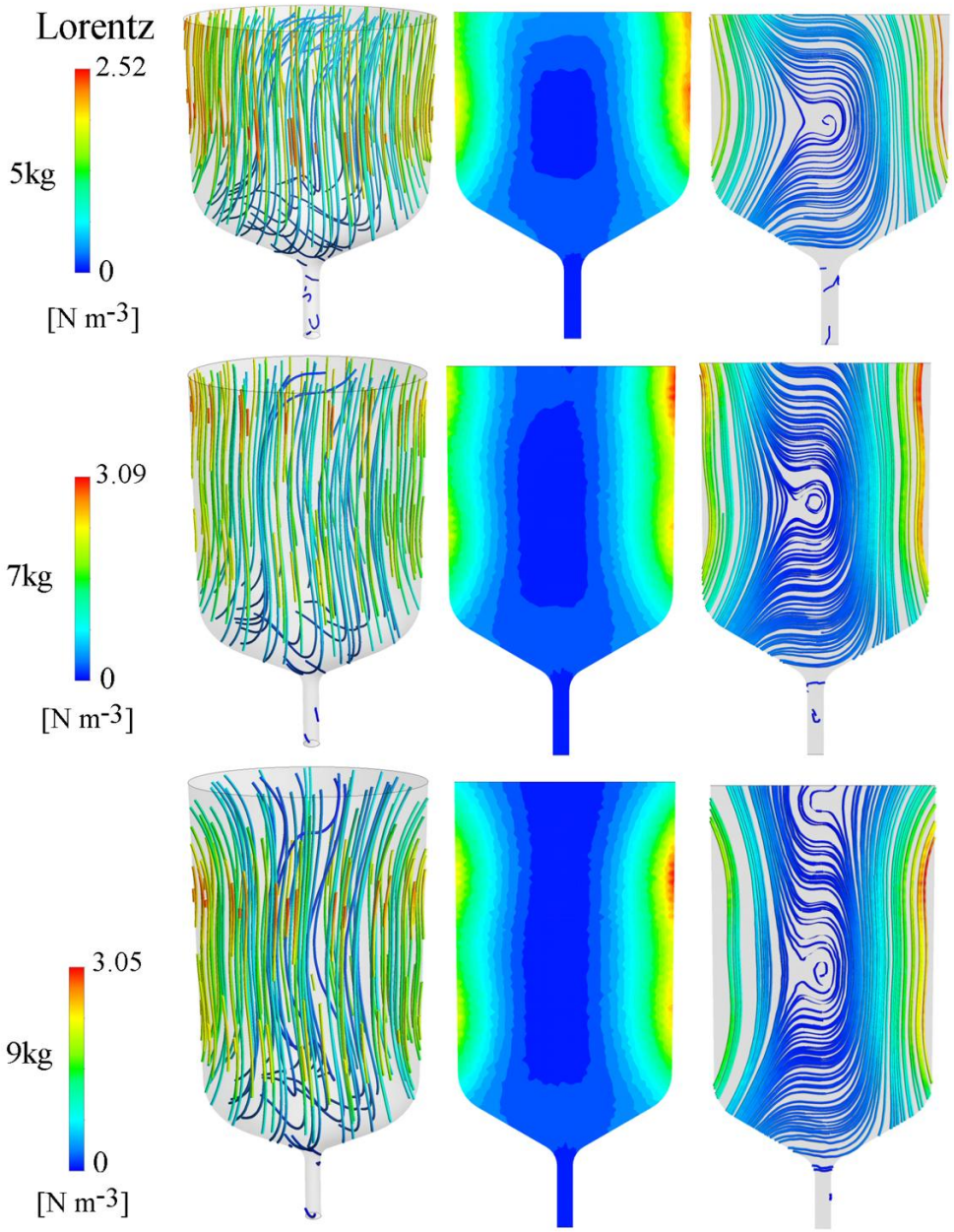

Figure 5.23: Numerical simulation of the Lorentz force density distribution in the melt inside the Kronos single-crucible setup as a function of the initial feedstock mass and a constant downwards-directed single-frequency TMF: 3D streamlines, 2D contour in central longitudinal cross section, 2D streamlines in central longitudinal cross section [Dro14b]

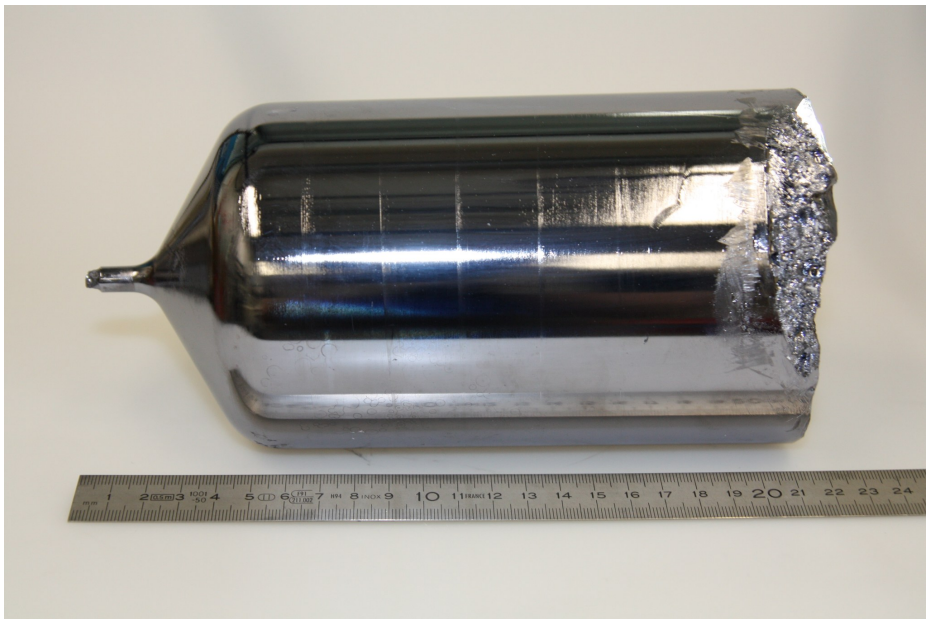

Figure 5.24: Picture of the 9 kg VGF-GaAs:Si crystal grown with utilized TMF, facets in the cone and several interface marker are visible on the crystal surface

results from the simulation showed decreasing Lorentz force densities in the upper melt region.

Fig. 5.24 displays the grown 9 kg VGF-GaAs:Si crystal. Nearly symmetric equidistant TMF markers were visible on the surface. The crystal was almost entirely monocrystalline, only in the rear crystal end polycrystalline grains developed in the crystal periphery. Compared to a 7 kg crystal, the enhancement of the crystal mass resulted in a nearly 4 cm increased crystal length with full 4" diameter.

Fig. 5.25 shows the shape of the solid-liquid interface, analyzed by DSL etching of a longitudinal cross section in <100>-direction. In Fig. 5.26 the respective values of deflection and β-angles are depicted. These values are compared to the so far best results from a 7 kg crystal standard growth process with identical conventional growth conditions, but with not yet optimized TMF parameters (see Figs. 5.21 and 5.22). The TMF markers in the cone, lower and center cylinder show almost continuous flat interfaces with only a minor asymmetry and w-shape. The lowest average measured interface deflections with around 4% and largest β-angles with on average 80° from all conducted growth experiments were achieved. In particular the deflection in the crystal periphery was significantly reduced through the optimum adjustment of TMF parameters. Enhanced tilting of the interface developed when crystallization proceeded towards the end of the HMM in the upper cylinder. In the area of the two last markers, the growing interface was situated at the end of

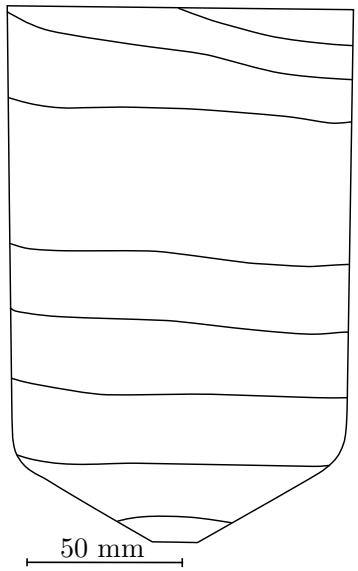

Figure 5.25: Interface shape of the 9 kg GaAs crystal grown within the scale-up approach with a nearly optimized set of TMF parameters

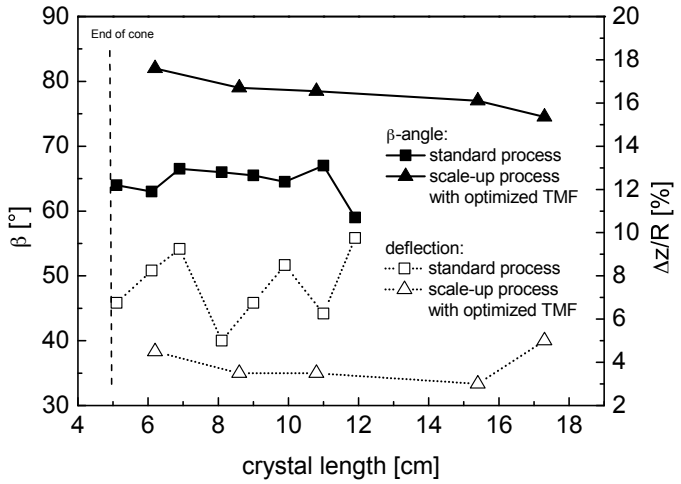

Figure 5.26: Comparison of the average measured values of deflections and β-angles of a 7 kg and 9 kg GaAs crystal, both grown with an optimized growth-matched TMF and with identical conventional growth conditions, asymmetries are neglected

the upper HMM coil. With the sudden decrease of the TMF impact on the melt, rising thermal asymmetries towards the top heater could not be compensated, which ultimately led to polycrystalline growth in this area. No decrease of the growth velocity or stagnation off the growth was observed in this scale-up process.

5.5.2 Speed-up

In this section it shall be evaluated, if convection generated by a TMF can remove accumulated heat from the interface to enable higher growth rates. Crystals shown previously indicated that an increase of the growth velocity requires TMF parameter adjustments.

While previous growth experiments were mainly conducted with growth velocities between 1.5-2.5 mm/h, within the speed-up intensification approach growth velocities up to 5.0 mm/h were reached. Three crystals were grown for comparison with v_{gr}=2.0-2.6 mm/h, v_{gr}=3.0-4.0 mm/h and v_{gr}=4.0-5.0 mm/h under identical thermal conditions, all with applied graphite susceptor. In contrast to the standard growth recipe, in speed-up experiments the cooling rate was accordingly increased, while axial thermal gradients were kept constant. The same TMF parameters were applied to examine the effects of the enhanced growth velocity (see table 5.9). A steady double-frequency TMF with B_0=2.1 mT was used.

I_{tot}	f_1,f_2	I_1/I_2	ϕ	B_0	$\mathrm{Ta}_{m,1}$,$\mathrm{Ta}_{m,2}$
72 A	10 Hz, 100 Hz	0.84/0.16	100°	2.1 mT	3.73×10^5, 1.35×10^5

Table 5.9: Parameters of the used double-frequency TMF for the speed-up growth experiments

Fig. 5.27 shows a qualitative comparison of the solid-liquid interface shape from the three grown crystals. The single crystal grown with maximal 2.6 mm/h showed a flat to slightly concave interface with a amplifying w-shape with progressing growth (same crystal was used for comparison of uniform vs. non-uniform phase shift in section 5.1 and is depicted here again for convenient comparison). The TMF in the upper crystal part was slightly too strong. The second single crystal grown with up to 4.0 mm/h showed a similar deflection with an enhanced interface asymmetry. The w-shape vanished, the central area near the crystal end was flat. This implies, that the TMF strength during that growth stage was better matched to the growth velocity. However, the rising asymmetry near the crystal end has to be avoided. The last crystal grown with up to 5.0 mm/h showed consistent very high deflections with its peak in the lower crystal cylinder. The TMF was by far to weak to create a convective flow that efficiently removes the excessive generated latent heat under these growth conditions. Polycrystalline growth started in the center area of the cylinder as a result of the strong concavity.

The qualitative impressions are supported by the measured values for the average interface deflections and β-angles for these crystals, seen in Fig. 5.28. Note that the

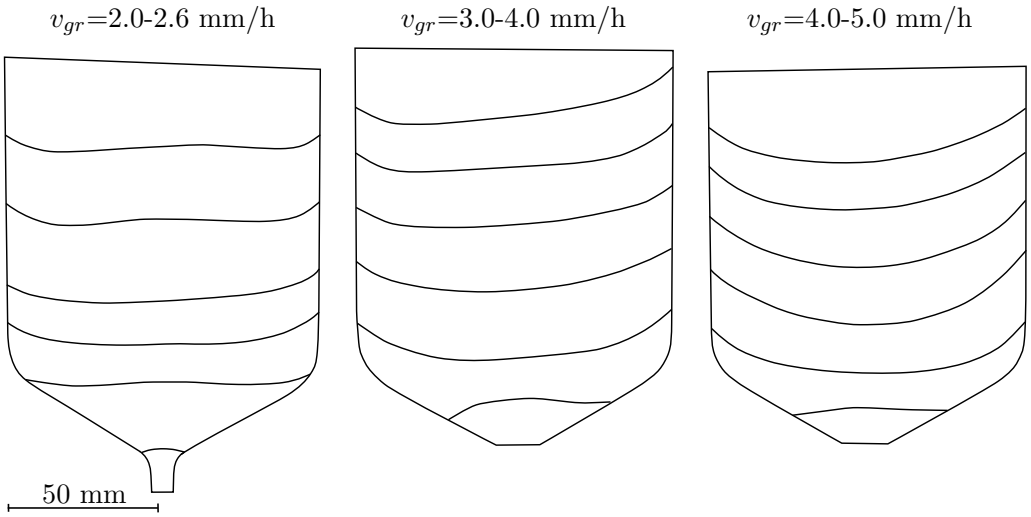

Figure 5.27: Shape of the solid-liquid interface of three crystals grown with identical TMF parameters, but increasing growth velocities

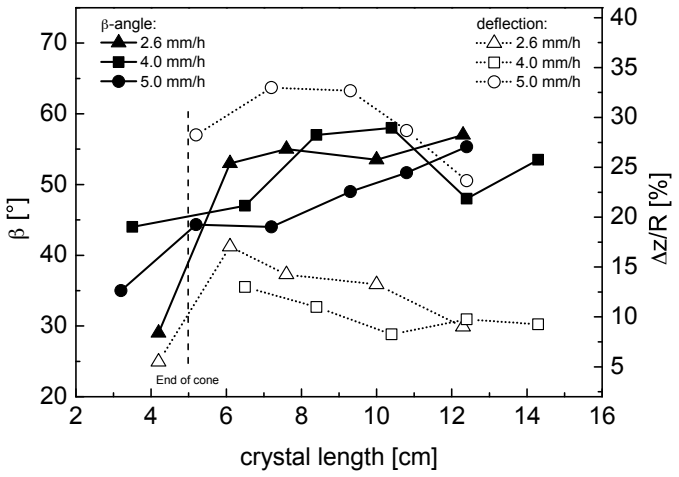

Figure 5.28: Measured values for the average deflections and β-angles for crystals grown with identical TMF, but different growth velocities

interface asymmetries are not considered in this picture. Deflection of the fastest grown crystal was almost three times larger compared to the others and showed also the smallest β-angles. A growth-matched and stronger TMF is necessary to improve the deflection for higher growth rates. Further, the application of a BN susceptor while maintaining axial temperature gradients should lead to a reduced concavity in speed-up experiments. In addition, according to the heat flux balance (see equation 2.1), heat dissipation can be improved by increasing axial thermal gradients. In this case, conventional growth parameters and design of growth recipe must be altered, too.

Experimental findings were comparable to a study based on numerical simulations on accelerated GaAs growth with utilized TMF by Dropka and Frank-Rotsch [Dro13a]. The melt flow near the solid-liquid interface was intensified with TMF, which resulted in a flattening of the radial thermal gradients in the melt and a reduced concavity of the interface shape. The efficiency of the TMF influence decreased with increasing growth velocity. The reason for this was the increasing natural interface concavity. Here, the impact of the downward-directed Lorentz force weakened because the angle between force and interface was diminished.

5.5.3 Numbering-up

In this section, results of the first growth experiments in the multi-crucible VGF setup are presented. Emphasis was put on the the investigation of thermal and TMF symmetry and the positive influence of the TMF driven melt flow on the interface shape during the simultaneous growth of several crystals.

Parameter studies

Exp.	I_{tot}	f_1, f_2	I_1/I_2	ϕ	B_0	$\mathrm{Ta}_{m,1}$, $\mathrm{Ta}_{m,2}$
1	90 A	20 Hz		90°	2.9 mT	3.80×10^6
2	98 A	20 Hz, 200 Hz	0.92/0.08	90°	3.1 mT	3.81×10^6, 2.90×10^4
3	90 A	20 Hz, 200 Hz	0.84/0.16	90°	2.9 mT	2.67×10^6, 9.72×10^4

Table 5.10: TMF parameters used for crystal growth experiments in the multi-crucible setup ECM

First crystal growth experiments in the new multi-crucible ECM setup were characterized by testing of the growth setup, of the control software, and the adjustment of seeding position and growth recipe. To save resources, test growth runs were conducted only with material in crucible position A. The other three crucible positions were filled with crystal-shaped graphite dummies for an enhancement of thermal symmetry in the HMM. Only GaAs:Si was grown to evaluate the interface shaping potential with TMF application. Applied growth velocities were in the range of 1.3-2.6 mm/h. The used susceptors were made of graphite. A steady TMF was applied

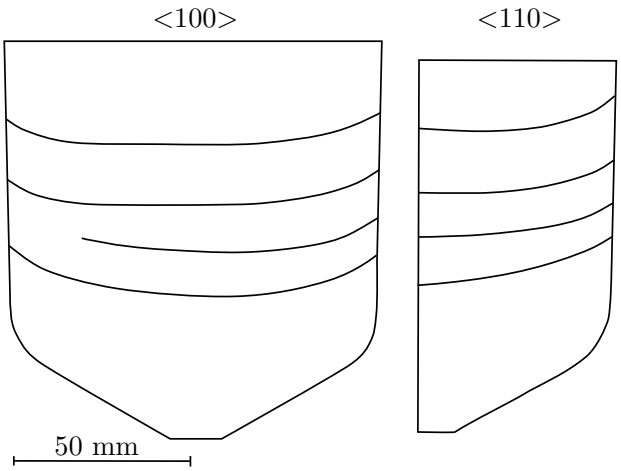

Figure 5.29: Interface shape in <100>- and <110>-direction of a crystal grown in in the multi-crucible setup where only crucible position A was loaded utilizing a single-frequency TMF

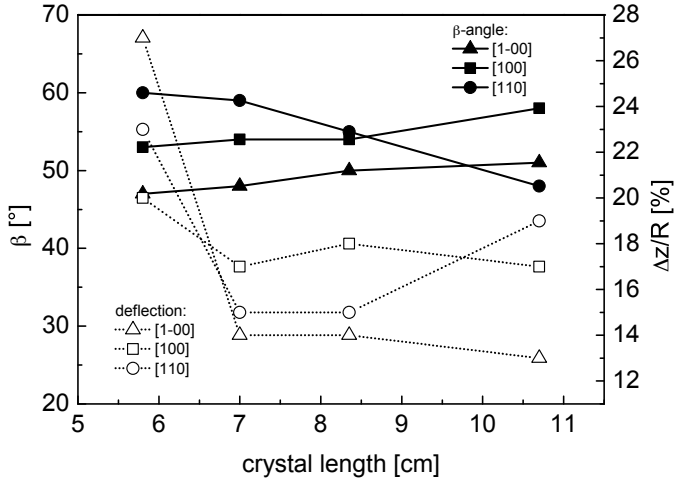

Figure 5.30: Comparison of the measured values of deflection and β-angle on the longitudinal cross section in <100>- and <110>-directions of the crystal grown with a single-frequency TMF

in every experiment. Utilized TMF parameters for all conducted growth runs are shown in table 5.10.

At first, only a steady single-frequency TMF was applied during growth for analysis of the thermal symmetry within a crucible position and to exclude asymmetries caused by the high frequency share. Fig. 5.29 shows the marked interface shapes taken from longitudinal cross sections in <100>- and <110>-direction of a crystal grown in crucible position A with a single-frequency TMF (table 5.10, Exp. 1). In Fig. 5.30 the corresponding values of deflection and β-angles are depicted. Deviations of the solid-liquid interface deflection and β-angles in different radial directions were in the range of 15-30%, which was slightly lower compared to crystals grown in the single-crucible setup. Reason for this was the location of the current supplies of the HMM coils in the center of multi-crucible setup. Thermal asymmetries were reduced compared to their arrangement on the outside in the single-crucible setup.

The influence of steady double-frequency TMF on the interface shape was analyzed in two separate growth experiments in crucible position A. Compared to the previous growth experiment with applied single-frequency TMF, the power distribution in the furnace and the growth recipe was slightly modified to improve axial heat dissipation. The TMF parameters for Exp. 2 and Exp. 3 are again depicted in table 5.10, identical conventional growth conditions were applied. Interface shapes and corresponding measured values for average deflections and β-angles of both crystals are shown in Figs. 5.31 and 5.32, respectively.

The application of a steady double-frequency TMF and the adjustment of the growth recipe led to a reduction of interface deflection with progressing solidification. The interface of the crystal grown with a small high-frequency share was flatter and partially w-shaped around the crystal axis, while the crystal grown with reduced low-frequency and enhanced high-frequency share showed a more regularly reduced concavity. The β-angles in both crystals were nearly identical, values of maximum deflection were somewhat lower in the crystal grown with larger high-frequency share. These findings were again comparable to the single-crucible setup (see Fig. 5.6). The radial interface asymmetry was low with values similar to the single-frequency TMF growth experiment in both crystals.

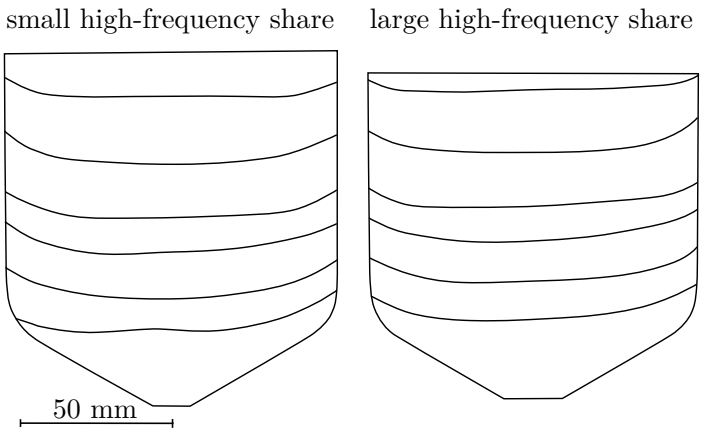

Figure 5.31: Comparison of interface shapes of two crystals grown in the multi-crucible setup in position A with small and enhanced high-frequency share

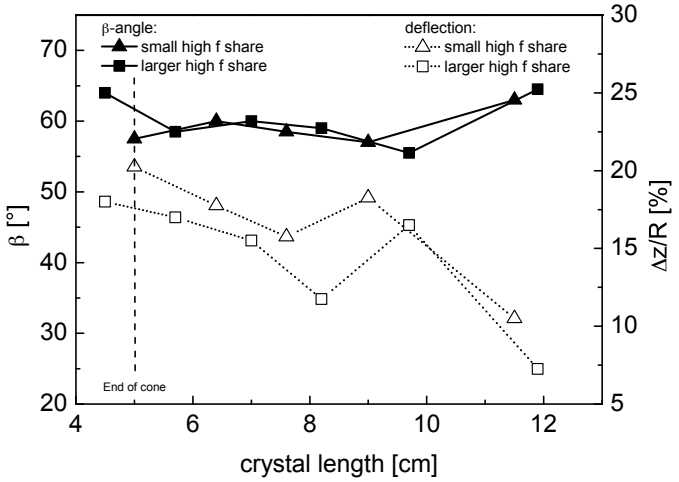

Figure 5.32: Measured values for the average deflections and β-angles for crystals grown with small and enhanced high-frequency share in the multi-crucible setup

Simultaneous growth of two GaAs crystals

Figure 5.33: Picture of the two simultaneously grown VGF-GaAs:Si single crystals with utilized TMF, facets in the cone and interface marker are visible on the crystal surface: (left) crystal from crucible position A, (right) crystal from crucible position C

Two GaAs:Si single crystals were simultaneously grown under the influence of a TMF. Used crucible positions were opposite A and C, positions B and D were again filled with graphite dummies. The growth experiment was conducted before axial heat dissipation was improved and before deviations in axial temperature profiles of the crucible positions A and C (see Fig. 4.8) were compensated. The results of this growth experiment should represent analysis on the differences in growth in both crucible positions without structural modifications. A steady double-frequency TMF was applied (see table 5.10, Exp. 2). Material masses of GaAs, B_2O_3, Si, SiO_2 etc. were identical in both crucibles, growth velocities were in the range of 1.5-2.0 mm/h. Here, too, interface marking provided knowledge about the progression of the growth of both crystals. When the crystals were taken out of the growth setup after the growth process, their position was marked with respect to the HMM central axis. Both grown crystals were monocrystalline (see Fig. 5.33). Longitudinal cross sections were produced, representing a complete length cut through the multi-crucible HMM from position A to C.

Fig. 5.34 shows the two marked interface shapes and their alignment towards the HMM central axis. Both interface shapes were uniform and symmetric, nearly no distinct tilting towards the HMM center was present. This confirmed the results from numerical simulations shown in section 4.1.2. Only minor differences in deflection and β-angle were noticed. They were associated to the measured variations in the

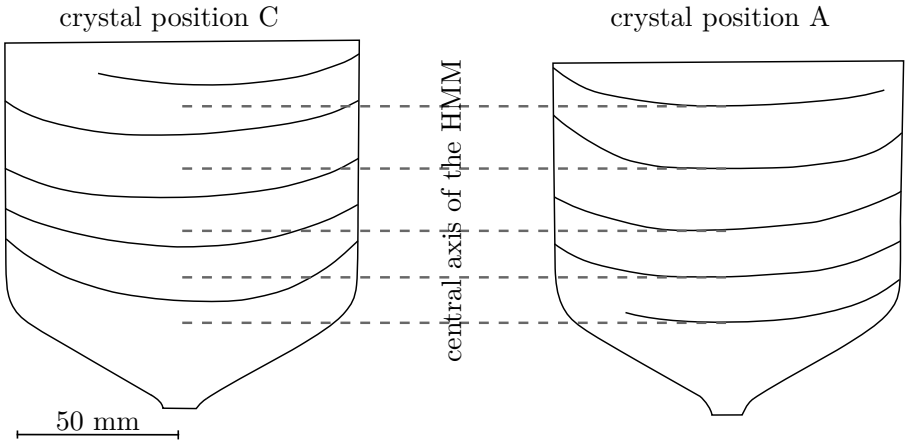

Figure 5.34: Interface shapes of simultaneously grown crystal A and C aligned towards the central axis of the HMM

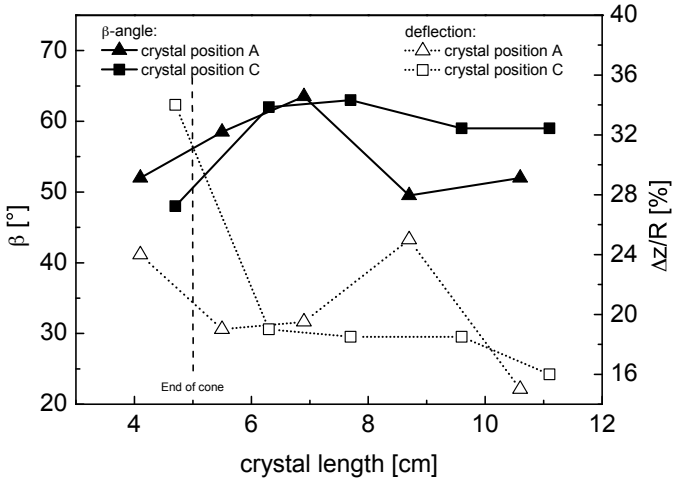

Figure 5.35: Measured values for average deflections and β-angles for simultaneously grown crystals A and C

axial temperature gradients in crucible position A and C (as depicted in Fig. 4.8) and differences in the radial heat dissipation. The marked interface positions in crystal A were around 15 mm below crystal C, which is in good agreement with the measured offset of the melt isothermal line of 10-19 mm in the temperature profiles. This small offset still enabled stable seeding. Furthermore, offset, identical cooling rate, and the about 15% smaller temperature gradients in position C compared to position A provided an increase of the growth velocity in position C by about 8-10%. The higher growth velocity in the cone area led to an enhanced deflection and a smaller β-angle in crystal C (measured values are depicted in Fig. 5.35). Growth velocities equalized in the cylinder of both crystals, leading to more similar deflections. Here, the β-angles in crystal A were smaller than in crystal C, in particular in direction towards the HMM center, where the minor asymmetry was most pronounced.

Generally, obtained values of deflections and β-angles in all crystals grown in the multi-crucible HMM were comparable to results from the single-crucible setup with applied graphite susceptor. It can therefore be assumed that, with further enhancement of the axial temperature gradients and the application of BN susceptors, it is possible to approach further reduced interface concavities. The axial crucible positions with respect to the HMM can be altered to compensate the interface offset in different crucible positions measured in dummy and growth experiments. Furthermore, an enhanced TMF impact in the lower melt area may be introduced by shifting the crucibles further into the HMM. In summary, the numbering-up approach showed a superior yield-to-energy process efficiency compared to the other intensification concepts. Labor effort, working gas and cooling water consumption in the multi-crucible HMM only marginally differed from the standard process in the single-crucible HMM. The yield multiplied with the number of simultaneously grown crystals, the specific energy consumption per grown crystal was markedly reduced.

6 Properties of 4" VGF-GaAs crystals grown with TMF

TMF induced changes in structural and electronic properties as well as micro- and macrosegregation in the grown VGF-GaAs:Si single crystals were investigated. SI GaAs crystals were grown with the aim to obtain best possible crystal properties and to reduce the tendency of polycrystalline growth.

6.1 Gallium arsenide doped with silicon

6.1.1 Suppression of microsegregation

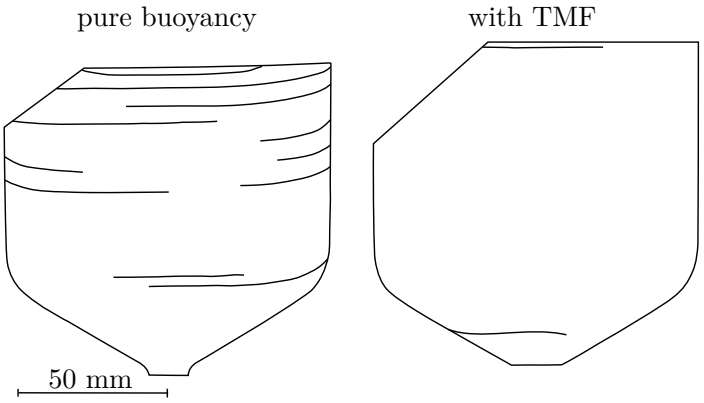

Figure 6.1: Comparison of the visible striations of two DSL etched <100> longitudinal sections of 5 kg GaAs single crystals grown (left) without TMF and (right) with the application of a TMF with B_0=1.2 mT in the single-crucible HMM

Fluctuations in composition are highly undesired during industrial growth of GaAs, especially for the aim of growing larger crystals. Disturbances of the convection and temperature variations at the interface are more likely to occur in higher melt volumes. The impact of TMF on microsegregation was therefore an important part of this study. A 5 kg reference crystal, grown in the heater-magnet module without the influence of a TMF with a growth rate of about 1.5 mm/h and an initial Si-concentration in the melt of c_0[Si]=1.3×10^{18} cm^{-3}, revealed striations along the whole crystal length with the typical concave interface bending. The left picture

in Fig. 6.1 shows a sketch of the DSL etched <100> longitudinal section. The weak striation pattern with irregular distances was enhanced towards the end of the cylinder due to increasing silicon incorporation with the progression of the growth process. The distances among the striations fluctuated between 25-70 µm. This corresponded to an oscillation period of about 60-170 s (see Fig. 6.2 (left)). Minor temperature fluctuations due to the heater controllers and the nitrogen inlet were responsible for these growth variations. With decreasing temperature during growth, the overpressure of 3 bar dwindled. The growth vessel was periodically refilled with gas which caused a temperature drop of about 3°C at the top heater. The temperature controller needed some time to regain the original value and to stabilize, respectively.

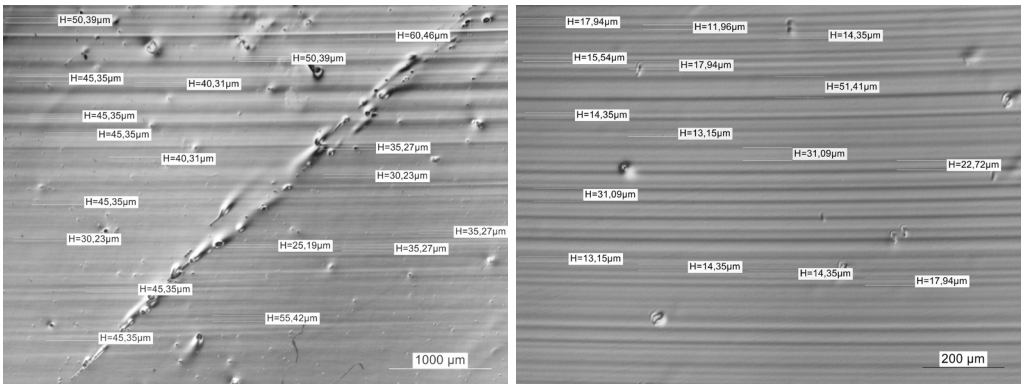

Figure 6.2: Sections from the DSL etching pictures from the upper cylinder regions of (left) the crystal grown without TMF with fluctuating striation distances between 25-70 µm and (right) the crystal grown with applied TMF with more regular distances from 15-50 µm of the residual striations at the crystal end

The crystal shown in in the right picture of Fig. 6.1 was grown under identical conventional growth conditions and Si-concentration, but with an applied double-frequency TMF with B_0=1.2 mT. Nearly no microsegregation was found with DSL etching technique and IR transmission measurements. The Lorentz forces induced a steady melt flow near the solid-liquid interface, which counteracted buoyancy force, equalized temperature fluctuations, and improved the mixing of the melt. The formation of striations was suppressed in most crystal areas. In other GaAs:Si crystals, grown under double-frequency TMF with induction strengths between B_0=0.9-3.0 mT, with growth rates between 1.5-2.6 mm/h, with varying Si-concentrations in the melt of c_0[Si]=1.2-4.9×10^{18} cm^{-3}, and with masses up to 9 kg, a severe reduction of microsegregation was detected. This observation was made in both the single- and the multi-crucible growth setup. Both simultaneously grown single crystals grown within the numbering-up intensification approach showed almost no striations.

There were two areas in all crystals grown with TMF where weak growth striations were noticed in almost every experiment: The lower crystal cone near the seeding area and the rear end of the crystal. In the lower area of the crystal cone the impact of the TMF was rather weak, since the induced convection was not able to reach this area. Irregular striations with varying distances were often observed. Visible striations with applied TMF at the crystal end significantly differed from striations in the cone. Here, the TMF had an impact on the melt, but the residual melt amount was insufficient to create stable convection rolls. Additionally, small fluctuations were easier accessible with IRT measurements and DSL etching, due to the increase of the concentration of the dopant Si with progressing growth. The residual striations had more regular reduced distances between 15-50 µm, which corresponded to a 35-120 s oscillation period at the applied growth velocity of 1.5 mm/h (see Fig. 6.2 (right)).

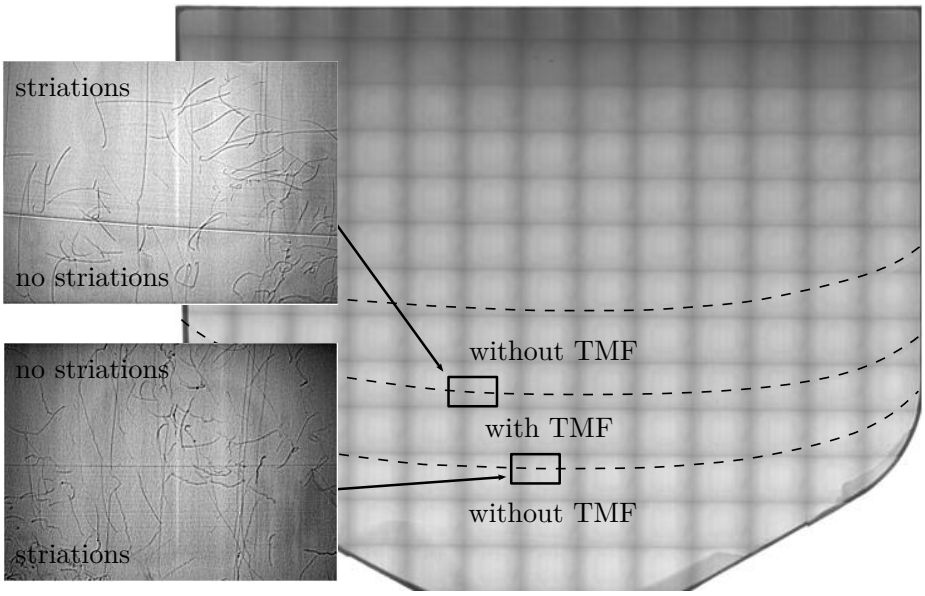

Figure 6.3: Assembled IRT picture of a <100> longitudinal section from a crystal grown partially without TMF with enlarged sections, the instant disappearance/appearance of striations with switching the TMF on/off is clearly visible

Figure 6.3 shows an IRT picture of a 5 kg crystal with an initial Si-concentration of c_0[Si]=3.3×10^{18} cm^{-3}, which has been grown with and without an applied steady double-frequency TMF. The growth velocity was 1.5 mm/h. In the respective areas the magnitude of the magnetic field was B_0=2.3 mT. The whole <100> longitudinal section was scanned in sections of 8.6×6.88 mm^2 an then put together. The instantaneous transitions between the different areas can be seen very clearly in the enlarged pictures. The microsegregation almost instantly disappeared when the

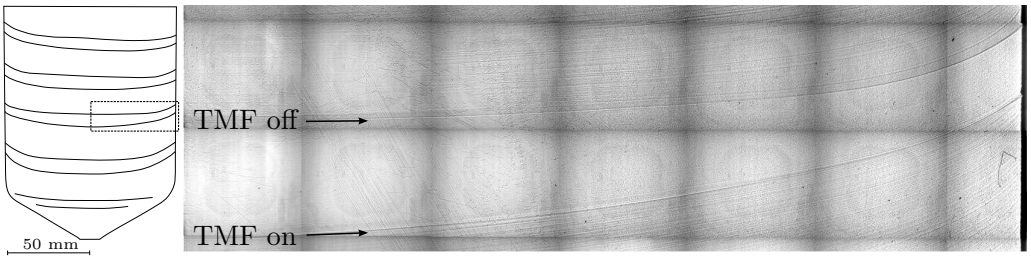

Figure 6.4: IRT picture and respective interface shape taken from a longitudinal cut in <100> direction of a 7 kg GaAs crystal grown partially with an optimized double-frequency TMF, IRT picture with view from the center to the rim, assembled from sections of 8.60 × 6.88 mm^2

TMF was switched on and vice versa. At the same time the shape of the solid-liquid phase boundary was detected because the switching on/off was marking the interface. As it can be seen in the picture, there was only a barely noticeable flattening of the interface with the TMF. It did not have ideal parameters for minimizing the deflection, because of the applied TMF phase shift of 60°.

Fig. 6.4 shows an IRT picture of a 7 kg GaAs crystal, which was partly grown with and without an optimized set of double-frequency TMF parameters for concavity reduction and an initial Si-concentration c_0[Si]=5.3×10^{18} cm^{-3} (see section 5.3). The magnetic field strength varied between B_0=1.5-1.8 mT, the growth velocity was enhanced to 2.0-2.5 mm/h. A <100> longitudinal cut of the grown crystal was scanned in sections of 8.60 × 6.88 mm^2 with IRT. The picture shows a segment from the center of the crystal cylinder, from the axis to the rim. The transition between the different areas can be seen very clearly. An irregular striation pattern was visible when the TMF was switched off during growth. Microsegregation almost instantly disappeared with the utilization of a double-frequency TMF.

6.1.2 Partial appearance of striations and critical flow conditions

Except for the already described visible striations in the crystal cone and in the rear crystal end, under certain conditions small areas with weak striations were observed when a TMF was applied. Different reasons causing the partial appearance of micro-inhomogeneities were found.

Fig. 6.5 (left) shows an IRT picture of a section taken from a crystal grown with steady TMF parameters. Here, periodic and nearly equidistant striations with distances >100 µm were observed in the crystal cylinder area around the half radius. In the remaining parts of the crystal most of the temperature fluctuations were suppressed through the induced steady convective flow. The source of these partially emerging micro-inhomogeneities was attributed to local enhancements of the growth velocity evoked by partially unsteady flow conditions. The locally emerging micro-inhomogeneities were mainly observed when a steady TMF was applied. Here, the

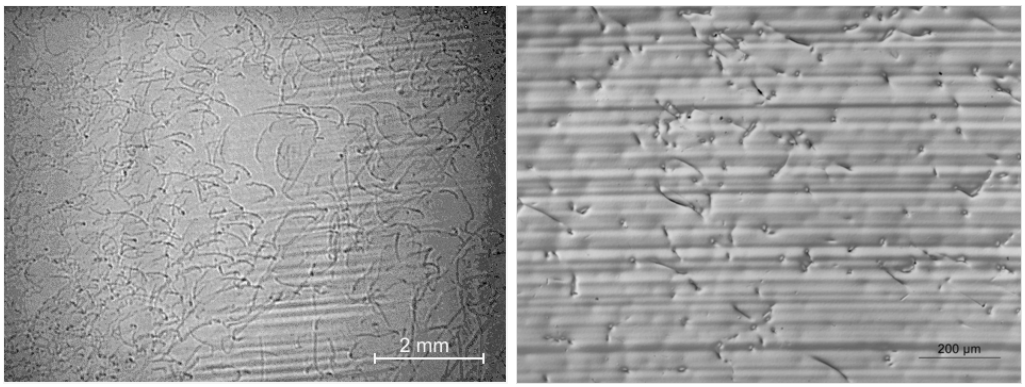

Figure 6.5: Details of IRT measurements and DSL etching pictures of GaAs:Si single crystals: (left) IRT picture of a crystal grown with not optimized steady TMF parameters, (right) DSL etching picture of a crystal with overcritical TMF parameters

TMF had a significant influence on the growth process, i.e. a modification of the interface shape, but was not matched to every growth step during solidification. Adjustments of the TMF strength to match different phases of the process resulted in a mostly striation free crystal.

If a certain critical strength of the Lorentz force was exceeded, the melt flow became time-dependent and regular striations with equal distances around 15-30 µm were induced (see Fig. 6.5 (right)). In that case, the interface shape became highly asymmetric with a large concave deflection, too (see corresponding interface shapes in section 5.1.3). It was observed, that this effect of time-dependent flow was triggered by TMF with large AC, a high frequency, and a magnetic Taylor number $\mathrm{Ta}_m > 1{\times}10^6$. Numerical results showed that the HMM winding shapes and the bus bar arrangements cause a slightly three-dimensional asymmetric magnetic field distribution, which are enforced when high-frequency TMF are used [Kas08]. The application of an enhanced high-frequency TMF led to increasing force density variations and to resulting time-dependent asymmetric flow fields.

Furthermore, the modification of conventional growth conditions reintroduced microsegregation. The partial appearance of striations with applied TMF was observed in crystals grown with enhanced growth velocity within the speed-up process intensification approach. The left picture in Fig. 6.6 shows a DSL etching picture taken from the center of a <100> longitudinal cross section of the crystal grown with v_{gr}=3.0-4.0 mm/h, the right picture a section of the lower crystal cylinder taken from an IRT measurement of a <100> longitudinal cut of the crystal grown with v_{gr}=4.0-5.0 mm/h. In both cases, striation patterns with irregular intensities and distances were observed. Striations were more distinct along the axis along the whole crystal length. Here, TMF induced convection was to weak to compensate setup-specific temperature fluctuations, which increased with higher cooling rates.

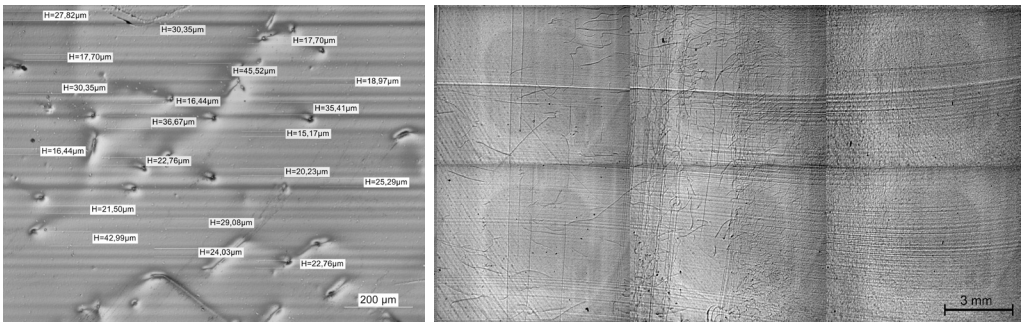

Figure 6.6: Irregular striation pattern with enhanced growth velocities: (left) DSL etching picture of the center of a <100> longitudinal slice of the crystal grown with v_{gr}=3.0-4.0 mm/h, (right) assembled IRT picture of a <100> longitudinal cut of the lower cylinder center from the crystal grown with v_{gr}=4.0-5.0 mm/h

6.1.3 Modification of macrosegregation

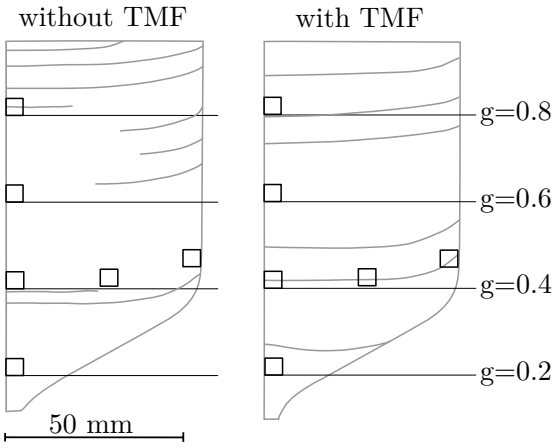

Figure 6.7: Axial and radial positions of the SIMS samples taken from crystals grown with identical conventional growth conditions with and without TMF, respectively

Two Si-doped crystals are compared to analyze the influence of the magnetic driven flow on dopant incorporation. The first one was grown without a TMF in the HMM and was used as a benchmark. The second one was grown with a steady double-frequency TMF with B_0=0.9 mT. The conventional growth conditions were identical: mass of initial GaAs feedstock, mass of dopant Si, B_2O_3 in mass and water content, mass of the added SiO_2, and the computer-controlled growth recipe with a growth velocity of 1.5 mm/h. The concave interface deflection of the crystal

grown with TMF was reduced by about 30% (see comparison of measured values for deflection in Fig. 5.20).

The incorporation of dopants was examined by Hall effect and SIMS measurements. Samples for Hall measurements were taken from longitudinal cuts along the central axis and in radial wafer geometry. The SIMS samples were taken from longitudinal cross section, too. In Fig. 6.7 the SIMS sample positions are depicted. Beforehand, the interface shape was obtained by DSL etching. In addition to axial samples taken from g=0.2-0.8, radial samples were cut from the lower crystal cylinder along the interface. The aim was to analyze radial dopant incorporation variations along the solid-liquid interface during growth.

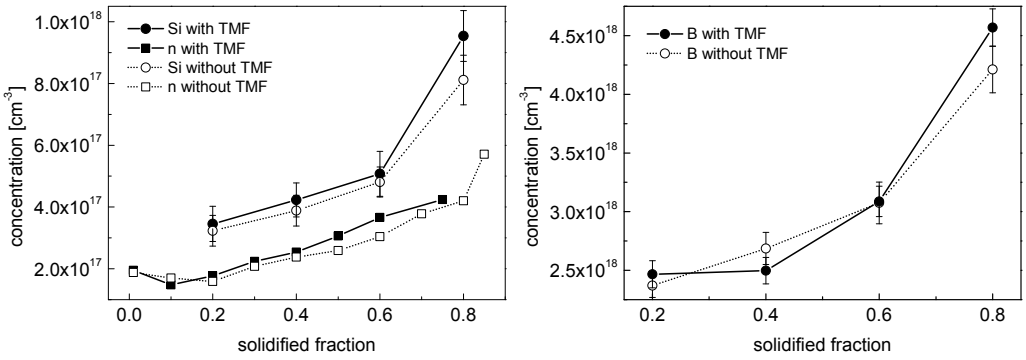

Figure 6.8: Comparison of two identical crystals grown with and without TMF, respectively: (left) axial charge carrier densities and axial concentration profiles of Si, (right) axial concentration profiles of B

Results from Hall and SIMS measurements along the crystal axis are shown in Fig. 6.8. The axial charge carrier density and the related Si content was continuously somewhat higher when the melt was exposed to a TMF. This effect was not observed near the seed, where TMF impact was small and facets with higher Si content might have influenced the measured charge carrier concentrations. In both crystals, the charge carrier densities corresponded to around 50-70% of the actual Si content. Compensating defects appeared to be equally responsible in both crystals. Self-compensation of Si can be excluded, as this should not occur for Si concentrations below $<5\times10^{18}$ cm^{-3} [New94]. The B content in both crystals rose from around 2.3 to 4.6×10^{18} cm^{-3} between g=0.2-0.8. In the crystal grown with applied TMF, the B concentration was stable in the lower cylinder and increased stronger towards the crystal end, compared to the reference crystal, where a more steady increase of the B concentration was observed. The measured concentrations of C slightly increased towards the end in both crystals with concentrations smaller than 1.0×10^{16} cm^{-3}. Therefore, carbon is disregarded in the following investigation.

The liquid-encapsulated VGF growth of GaAs:Si is a non-conservative system, where reactions of Si and B_2O_3 have significant influence on dopant concentrations in the crystals. The effective distribution coefficient of Si changes during growth un-

der varying growth conditions, e.g. solute reactions with the encapsulation material, changing growth velocities or convective flow. The axial concentration profiles from SIMS and Hall effect measurements from Fig. 6.8 (left) were fitted using Czapelski's approach (see equation 2.24) to analyze the reaction between the GaAs melt and the B_2O_3 cover and the impact on Si incorporation. Convection dependent effective distribution coefficients k_{eff} of Si were calculated as a function of the solidified fraction (see equation 2.25). The initial Si concentration c_0 in the melt was calculated from measured values near the seeding region with Scheil's equation and the value k=0.15 for the Si distribution coefficient in VGF-GaAs with B_2O_3 encapsulation [Bir02]. In Fig. 6.9 the results are plotted. Both SIMS or Hall effect measurements demon-

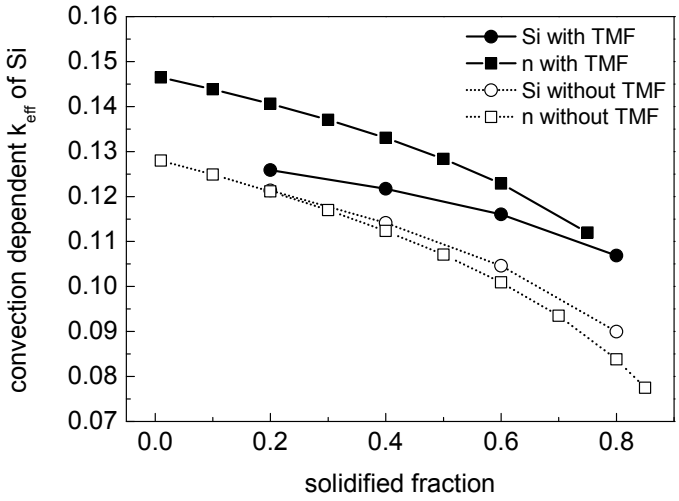

Figure 6.9: Calculated convection dependent effective distribution coefficients of Si in VGF-GaAs with and without TMF based on Hall measurements and SIMS data

strate that the applied TMF provides a higher effective distribution coefficient along the axis. Additionally, Si incorporation dropped with progressing growth. This was noticed for both crystals grown with and without TMF. The slope of the curves was very similar. Continuous reaction of Si with B_2O_3 was assumed, although the SiO_2 concentration was stabilized in the encapsulant through the addition of fused silica. The decrease of the convection dependent effective distribution coefficient with progressing growth was observed in all other measured crystals, independent from conventional growth conditions and TMF parameters. The slope of the progression differed in each case, values of the determined k_{eff} at the beginning of the growth processes varied between k_{eff}=0.11-0.16.

The B_2O_3 encapsulation served as a B reservoir, activated through the reaction with Si. In particular with respect to the literature value of the distribution coefficient of B in GaAs, often reported as k_{B}=2.1 [Kor99], the enrichment of B in the

growing crystals through increasing reactions between Si and B_2O_3 with progressing process time, was apparent. More B was released into the melt than the growing crystal withdrew through the segregation process [Bir03]. Generally, the enhanced incorporation of B in GaAs:Si should be avoided, because it acts as an efficient scattering center in GaAs [Wal79] which can reduce the mobility. Crystals grown with a reduced amount of B_2O_3 showed higher electron mobilities as a function of electron concentration compared to crystals grown with larger B_2O_3 masses. This may be evidence for increasing B incorporation with enhanced B_2O_3 mass.

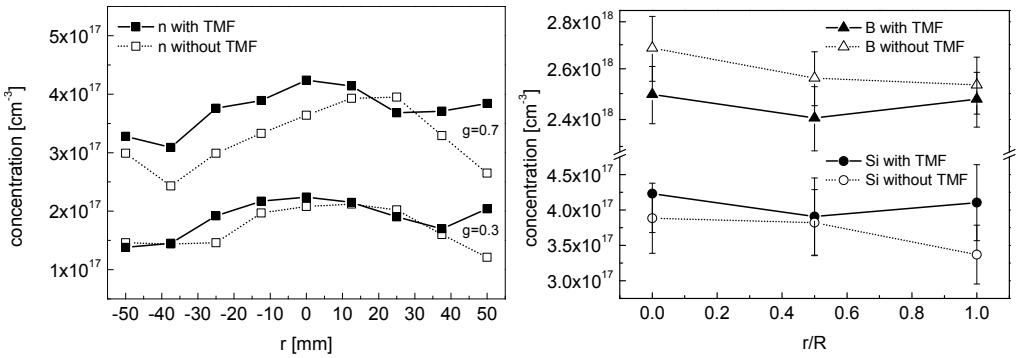

Figure 6.10: Comparison of two identical crystals grown with and without TMF, respectively: (left) radial charge carrier densities in wafer geometry taken from the lower and upper crystal cylinder, (right) radial B and Si incorporation along the solid-liquid interface taken from the lower crystal cylinder

The radial charge carrier distribution in wafer geometry flattened with the reduction of the interface deflection with an applied TMF (see Fig. 6.10 (left)). In particular in the periphery, an enhancement of the charge carrier density was observed. The radial incorporation profiles became more w-shaped. Fig. 6.10 (right) shows radial B and Si concentrations measured with SIMS along the concave interface. The B and Si concentrations in the crystal grown without TMF had their minima near the crystal edge with increasing concentration towards the center. The crystal grown with TMF showed their minimal radial B and Si concentrations around the half crystal radius. The radial distribution of dopants along the solid-liquid interface was modified with applied TMF. Therefore, the flattening and increasing w-shape of the radial charge carrier distribution in wafer geometry can be attributed to the reduction of the interface concavity and the modification of radial macrosegregation with the use of a TMF.

Both axial and radial concentration profiles indicated, that with a utilized TMF not only the Si distribution inside the crystal was altered, but also the total content of Si was slightly enhanced. For further investigation, the dependency of the axial charge carrier densities on convective flow was investigated on a crystal where a current-matched double-frequency TMF (with B_0=1.5-1.8 mT) was switched on and

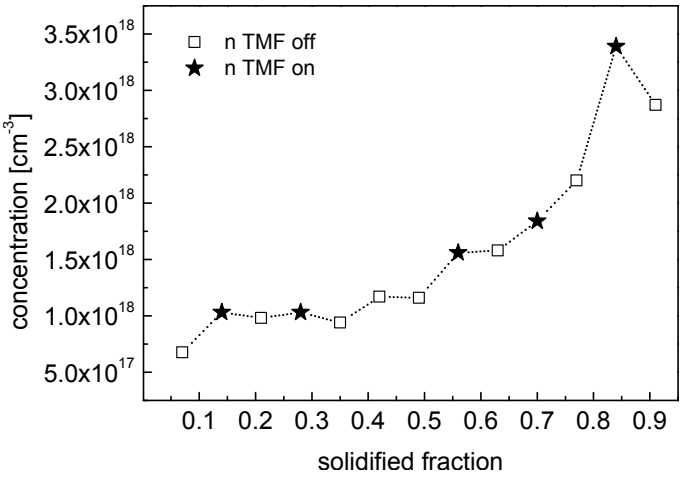

Figure 6.11: Measured charge carrier densities of a crystal grown partially with current-matched double-frequency TMF

off several times. Aim was to eliminate all possible conditions, which might disturb the comparability of the solute incorporation with and without magnetic driven flow. The experiment was accompanied by numerical simulations on melt velocities and temperature distribution for pure buoyancy and double-frequency TMF cases. Fig. 6.11 shows the measured axial charge carrier densities as a function of the solidified fraction. Here, the behavior indicated a slight increase of axial solute incorporation when the TMF was switched on. Figs. 6.12 and 6.13 show results from numerical simulations of this specific growth process for a solidified fraction of g=0.5 for pure buoyancy and g=0.55 for TMF case with respect to experimental results. In case of pure buoyancy flow temperature distribution in the melt was slightly asymmetric. Several meridional vortices developed, with differing flow directions dependent on the axial positions. Highest flow velocities were found in the upper melt region. The downwards-directed Lorentz forces induced by the applied double-frequency TMF generated a melt flow opposite to the natural buoyancy driven convection. Results were a convex temperature distribution in the melt and a downwards-directed flow near the crucible walls. Flow velocities decreased compared to the pure buoyancy case. The concave deflection of the interface was reduced. With TMF two meridional vortices situated around 2/3 of the melt radius were dominant near the interface. In the melt center one azimuthal vortex was dominant. A minor asymmetry due to the specific HMM design was noticeable. With the application of a TMF the melt flow was more homogeneous and melt was constantly transported from the upper melt region to the interface. The enhancement of Si incorporation with TMF was due to the reduction of flow velocities in the melt. Maximum velocities in the melt decreased, from 1 cm/s to 0.2 cm/s with TMF application.

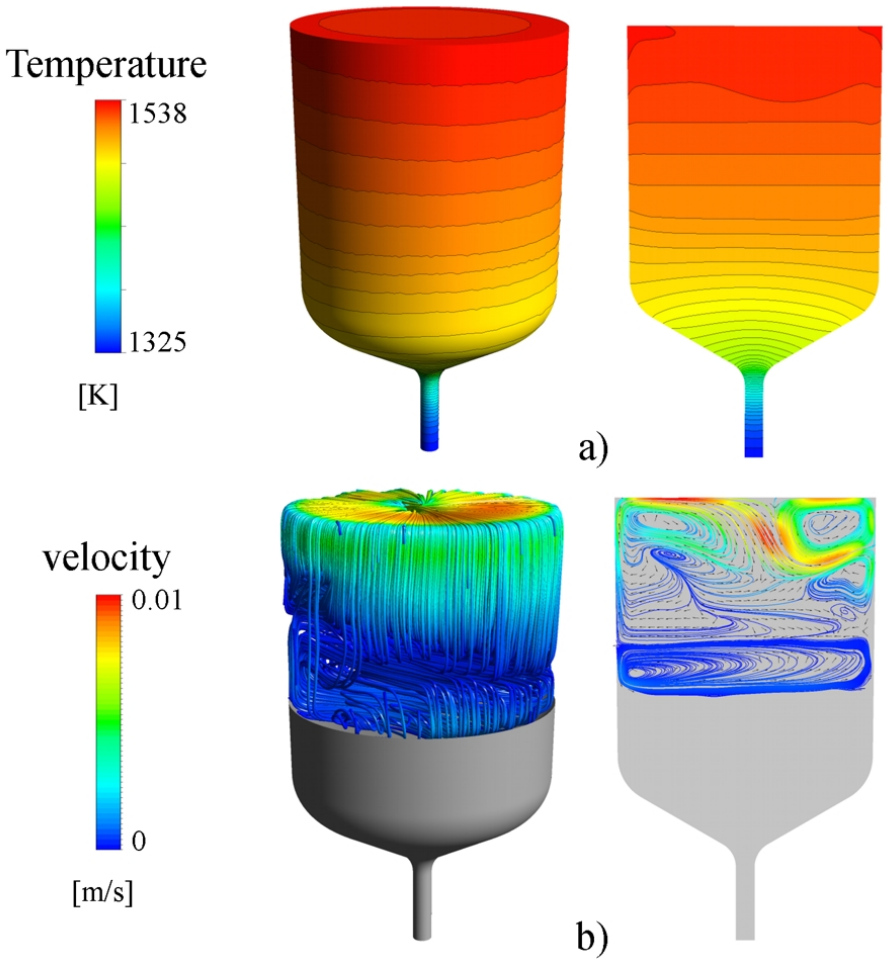

Figure 6.12: 2D and 3D numerical simulation in 7 kg GaAs for pure buoyancy case: a) temperature distribution, b) streamlines and vectors [N. Dropka, IKZ Berlin]

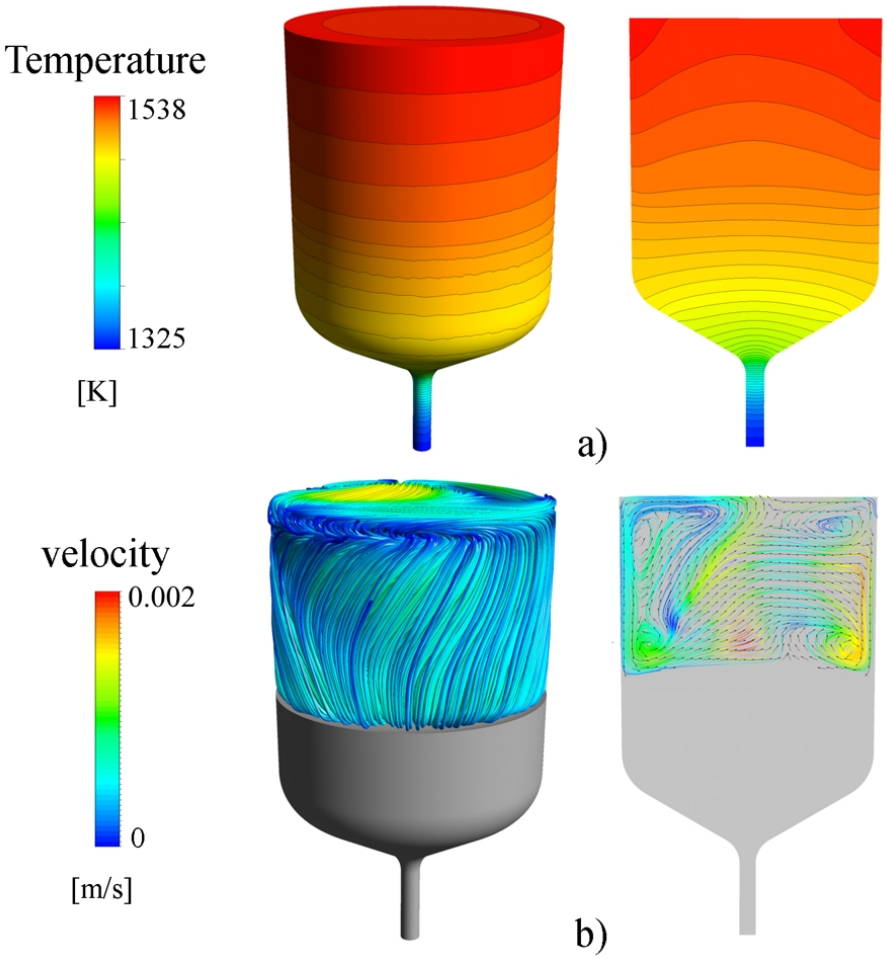

Figure 6.13: 2D and 3D numerical simulation in 7 kg GaAs for applied double-frequency TMF with B_0=1.8 mT and with an interface position near the center of the crystal cylinder: a) temperature distribution, b) streamlines and vectors [N. Dropka, IKZ Berlin]

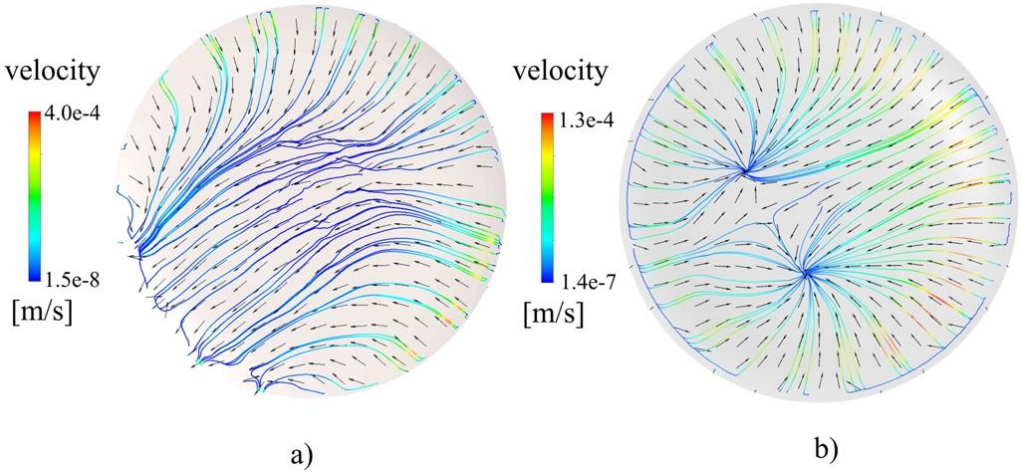

Figure 6.14: Calculated flow velocities and flow direction at the solid-liquid interface for interface positions in the center of the crystal cylinder: a) pure buoyancy case with concave interface, b) for applied double-frequency TMF with B_0=1.8 mT with slightly w-shaped interface [N. Dropka, IKZ Berlin]

The melt flow at the solid-liquid interface was most important for investigation on the axial and radial dopant incorporation profiles. Simulated melt velocities are depicted in Fig. 6.14. Generally, flow velocities at the interface were higher without applied TMF. Here, flow directions and flow velocities were asymmetrically distributed with highest flow velocities near the crucible walls. The large dominating meridional vortex at the interface provided a mainly aligned flow in one direction. With applied TMF, the flow along the interface was radial-symmetric with highest flow velocities located at 2/3 of the radius in the area of the dominant meridional vortices. Flow velocities around the axis lay in the same order of magnitude with and without TMF. But with TMF, the flow from the periphery towards the center was converging, leading to divergence of melt flow and interface around the crystal axis. This contributed to the experimentally observed enhancement of the Si incorporation. According to theoretical investigations for vertical Bridgman growth, converging melt flows in direction of the center at the solid-liquid interface cause a radial segregation profile with peaking concentration along the crystal axis [Pri05].

The enhanced steady w-shape of the radial incorporation profiles (Fig. 6.10) observed in wafer geometry and along the interface in the crystal grown with TMF might be amplified by the small flow velocities in the center and in the melt periphery, together with the high flow velocities around 2/3 of the radius. Here, the diffusion boundary layer had a decreased thickness, resulting in a diminished dopant incorporation. A combined use of TMF and ultrasonic vibration may help to reduce the diffusion boundary layer thickness along the axis to further flatten the radial

incorporation profile [FR12]. Increasing incorporation in the crystal periphery with applied TMF helps to flatten charge carrier densities on a wafer, even if the solid-liquid interface has a concave bending.

6.1.4 Further properties of grown GaAs:Si crystals

In addition to effects on micro- and macrosegregation, a TMF-induced change of the solid-liquid interface shape and the melt flow had significant influence on further GaAs:Si crystal properties.

Facets

The formation of facets was usually observed at the outer crystal surface of the cone area (see Fig. 5.1). It served as a first distinctive feature of a grown single crystal (at least in this area). The length of the facets is directly proportional to the magnitude of supercooling. Hence, small and regular facets are desired for a reduction the probability of twinning. For analyses of facet growth longitudinal cuts in <110>-direction were prepared. Faceting was analyzed with DSL etching and IRT measurements. Different etching behavior and contrast variations were caused by enhanced Si incorporation due to the different incorporation kinetics in the facets. Due to the angle between crucible and interface, faceting was mainly found in the cone area.

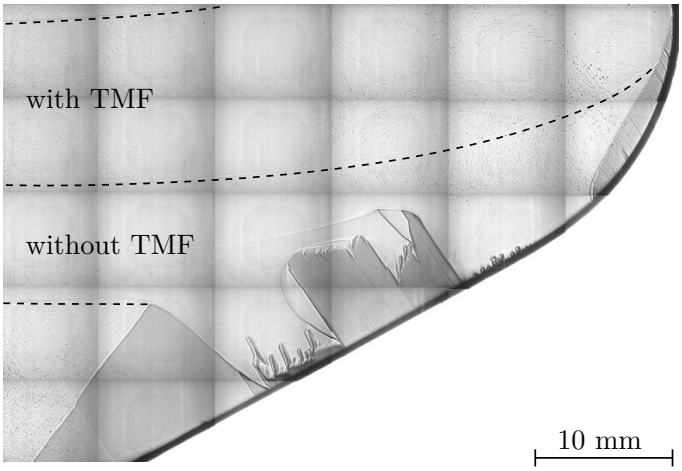

Figure 6.15: IRT picture of the half cone area of a longitudinal cut in <110>-direction from a crystal grown partially without a TMF shows unstable facets when no TMF is applied

Fig. 6.15 shows an assembled IRT picture of the half cone area of a longitudinal cut in <110>-direction from a crystal grown partially without a TMF. The switching off and on of the TMF was marked by weak induced striations. They are drawn into

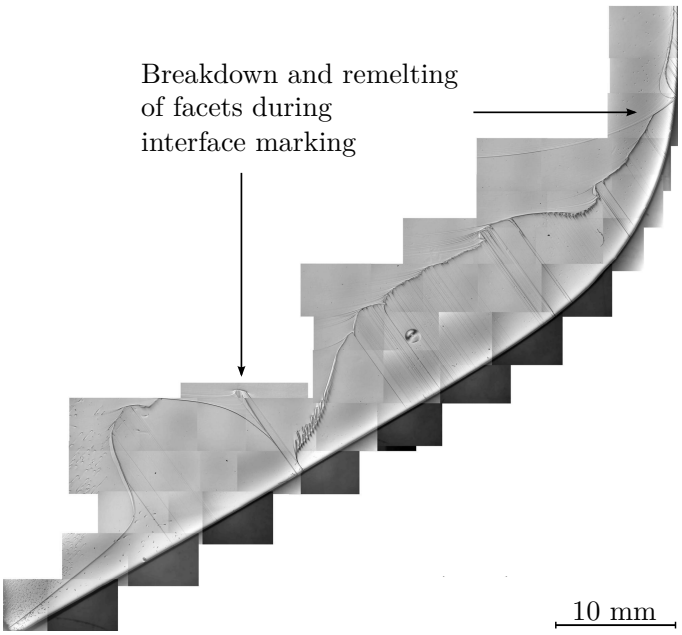

Figure 6.16: Assembled DSL etching picture of the cone area of a longitudinal cross section in <110> of a crystal grown with TMF

the picture to guide the reader's eye. While facets were stable under steady flow conditions with a double-frequency TMF, with its deactivation facets instantly broke down. Their re-establishment was noticed to be irregular and intervened by further complete breakdowns. Unsteady flow conditions, also causing striations, seemed to be responsible for fluctuations of the facet growth. Facets in a crystal grown with a continuous double-frequency TMF are shown in Fig. 6.16, an assembled DSL etching picture of a longitudinal cross section in <110>-direction. As long as the TMF parameters were not changed, facets were usually stable with rather constant length. When the interface was marked by TMF parameter variation, the change in convection led to a breakdown of the facets. Sometimes even a slight remelting of the facets was observed, due to the increasing downward-directed flow (see upper marker in Fig. 6.16).

Facets in the cylinder on longitudinal cross sections were observed only in crystals with very small β-angles. Fig. 6.17 shows a section from the cylinder center of a DSL etched longitudinal cut in <110>-direction from a crystal grown with strong asymmetric interface shape (see full morphology in Fig. 5.9). In this area, the angle between solid-liquid interface and crucible was only in the range of 35-45°. This values were only little higher than usual contact angles in the crucible cone. The formation of stable and very small facets was observed, only disrupted by interface marking. Cylinder facets were not observed with DSL etching and IRT measurements in longitudinal cross sections of other crystals with more symmetrical interface

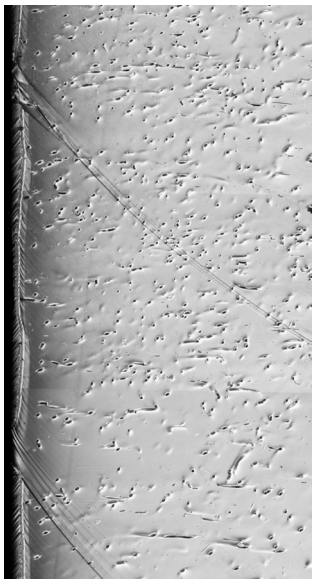

Figure 6.17: DSL etched longitudinal cut in <110>-direction of a crystal with small crucible contact angle showing small and stable facets in the cylinder area

and reduced deflection. One has to consider, that by taking crystals out of the crucible, cutting, grinding, and polishing, few 100 µm of the outer surface are lost. It stays unclear if reduced deflections in the crystal cylinder suppressed faceting or if facets were to small to be observed. Nevertheless, twinning was successfully nearly completely avoided. In all GaAs:Si growth experiments, a twin emerging from a facetted region was observed only once.

Dislocations

Focus of the following investigation is put on the analysis of changes in dislocation densities, their distribution and progression induced by TMF application, and the subsequent change of the interface shape. The formation of dislocations was qualitatively investigated with DSL etching and IRT measurements on longitudinal cross sections of the grown crystals. Quantitatively, the EPD was measured in many crystals on half-wafers taken from different axial positions in the crystal cylinder.

Dominating dislocations in the majority of the grown single crystals were glide dislocations starting near the crystal edge and proceeding far into the crystal. They were induced by thermal stress and lay in the $\{111\}\frac{1}{2}<110>$ glide system (see Fig. 6.18). No distinct decrease of the dislocation density of a crystal grown with steady double-frequency TMF was obtained compared to the reference crystal grown under the same thermal conditions but without TMF (see their comparison in microsegregation in Fig. 6.1). Here, TMF parameters and thermal growth conditions were

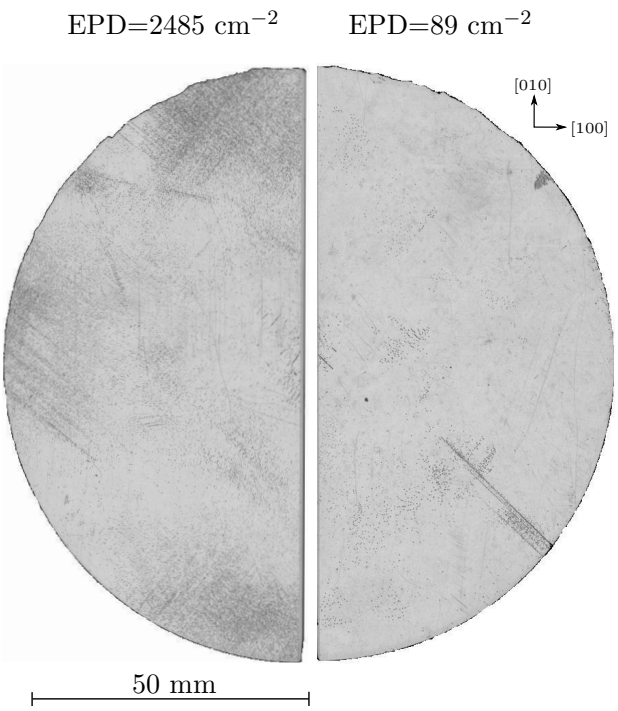

Figure 6.18: KOH etched half-wafers for determination of the EPD: (left) from crystal grown with steady double-frequency TMF and graphite susceptor with a large number of glide dislocations, (right) from crystal grown with a current-matched double-frequency TMF and a BN susceptor

not yet optimized, average EPD values were in both cases in the range of 3000-4700 cm^{-2} with decreasing values towards the end of the cylinder due to increasing Si incorporation. A significant EPD reduction was observed with the application of the improved standard growth recipe with v_{gr}=2.0-2.6 mm/h and further optimized double-frequency TMF parameters. A direct comparison of two crystals grown under identical thermal conditions, but exposed to various TMF, i.e. single-frequency TMF and double-frequency TMF (see comparison of the interface shapes in Fig. 5.4), showed not only an average reduction of the concave interface deflection in case of the double-frequency TMF in the cylinder area by 22%, but also nearly a halving of the EPD value. While the crystal grown with steady single-frequency TMF had measured average EPD values between 3300-5600 cm^{-2}, the crystal grown with steady double-frequency TMF showed values between 2300-2600 cm^{-2} (see left half wafer shown in Fig. 6.18).

A severe reduction of dislocation densities was achieved by modifying conventional growth parameters and/or TMF parameters. For example, a reduction of the growth rate to about 1.5 mm/h led to EPDs from 700-1700 cm^{-2}. The reduction of radial thermal gradients with simultaneous promotion of the axial heat dissipation through

the replacement of the standard graphite susceptor with a BN susceptor resulted in a significant EPD reduction, too. The application of a current-matched double-frequency TMF (see interface shape in Fig. 5.21 (right) and values of deflection and β-angle in Fig. 5.22) led to an interface shape with slightly convex center and a pronounced reduction of the deflection near the crucible wall. Thermal stress was reduced in this crystal and the measured average EPDs were 89 and 108 cm^{-2} in the lower and upper cylinder, respectively. These values were comparable to EPDs of 3" VGF-GaAs:Si grown under optimized thermal conditions [Bir03] and even below published average EPD data for industrially grown 4" VGF-GaAs:Si [Bue01]. In Fig. 6.18 the KOH etched half-wafer is depicted. The generation of glide dislocations was nearly suppressed with the application of BN susceptor and current-matched TMF parameters. They were observed only in one direction, caused by minor interface asymmetries. Residual dislocations were mostly uniformly distributed.

Process intensification within the single-crucible setup led to increasing EPD values. An increase of the dislocation density was observed within the scale-up intensification approach and a crystal mass of 9 kg. The average value of 5430 cm^{-2} in the crystal cylinder was higher compared to crystals with standard length. Especially a large number of glide dislocations was observed. With decreasing TMF influence on the interface shape near the crystal end, rising thermal asymmetries caused the enhanced generation of dislocations. The average EPD in the crystal grown with v_{gr}=3.0-4.0 mm/h and graphite susceptor were in the range of 12470-1260 cm^{-2}, with decreasing values with increasing crystal length. A large amount of glide dislocations was observed in the lower crystal cylinder, while the EPD from the upper cylinder was comparable to other crystals grown with standard growth rates and graphite susceptor due to the increasing dopant incorporation. Comparatively low average EPD values were obtained in simultaneously grown single crystals within the numbering-up intensification approach. The single crystal A showed a reduced

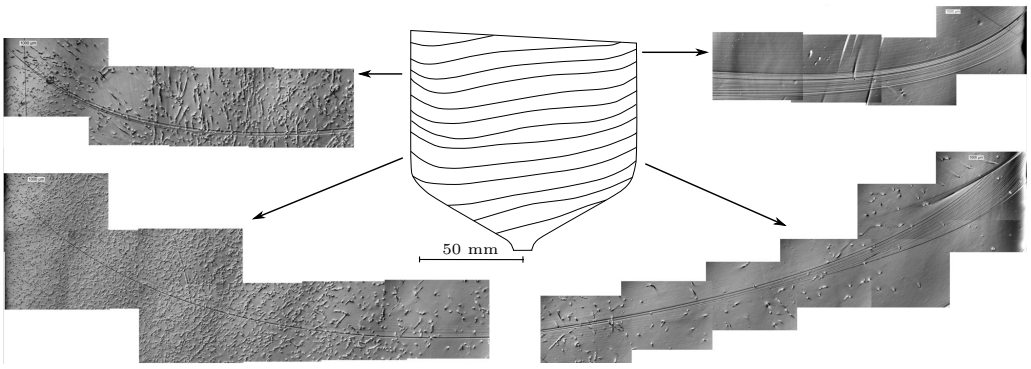

Figure 6.19: Assembled DSL etching pictures of different crucible-near positions on a longitudinal cross section in <100>-direction of a crystal grown with a strong asymmetric interface shape

dislocation density compared to crystal C due to the more uniform and slightly smaller growth velocity and the resulting reduced deflection in the lower cylinder. Measured EPD of crystal A in the upper cylinder was 470 cm^{-2}, in crystal C at the same position 1050 cm^{-2}.

The concavity of the interface was reduced with an applied TMF, even w-shaped interfaces with a convex center and asymmetric interface were obtained. In particular, interface asymmetries affected the radial dislocation distribution. Fig. 6.19 shows assembled DSL etching pictures from the upper and lower cylinder of a single crystal grown with a strongly asymmetric progression of the interface deflection (see also section 5.1.2). While on the right side, where the interface was tilted but relatively flat, a low dislocation density was observed, it significantly increased on the left side. Here, the deflection near the crucible was amplified, resulting in increasing thermal stress and the formation of dislocations. The decreasing magnitude of the deflection and the increasing Si incorporation with progressing growth were responsible for the overall decrease of the dislocation density towards the crystal end.

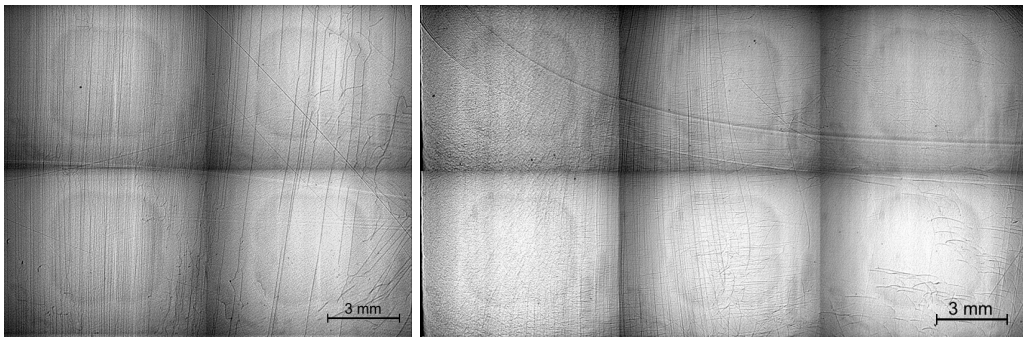

Figure 6.20: Behavior of grown-in dislocations with changing interface morphologies: (left) IRT picture taken from the center area of a <100> longitudinal section, with a slightly convex interface (see TMF marker in the center), (right) IRT picture taken from the rim area of a <110> longitudinal section

By affecting curvature and thermal stress along the interface, a TMF had an indirect influence on dislocation distribution and density. Furthermore, a changing behavior of grown-in dislocations with modified interface morphologies was observed. Fig. 6.20 (left) shows a section from a longitudinal cut in <100>-direction of a crystal with a slightly convex solid-liquid interface (visualization through TMF marking technique) in the crystal center. The grown-in dislocations proceeded nearly perpendicular to the interface, whereby the dislocations fanned out. The dislocation lines followed the progression of the interface shape through gliding and climbing processes. Fig. 6.20 (right) shows the rim section of a longitudinal cut in <110> direction of a crystal with a flat interface in the center and large deflection near the

crucible wall (again visualized by TMF marking). With such an interface shape the dislocation density in the periphery was around one order of magnitude larger than in the center, due to rising thermal stress near the crucible wall. Here, grown-in dislocations, also followed the progression of the interface. The concave deflection in the crystal periphery led to a focusing effect of grown-in dislocations. With a strong decrease of stress-induced dislocations, the potential of distributing and growing out residual grown-in dislocations with convex interfaces gains on importance for further dislocation reduction and their favorable arrangement on a wafer.

Residual stress

The residual stress of grown crystals plays a significant role during material processing. The risk of substrate breakage and slip generation during wafering and device fabrication processes has to be avoided. Residual stress remains inside the crystals after thermoelastic stress relaxes due to the formation of dislocations during cooling of the crystal. The residual stress distribution at room temperature indicates the properties of the thermal field during growth and cooling. Results from residual stress measurements are not straightforward to interpret. Many growth and non-growth related factors influence their magnitude and distribution. This is why only crystals with the following properties are compared: identical conventional thermal setup, same feedstock masses and identical thermal conditions during growth and cooling to room temperature. Only the TMF parameters during growth differed.

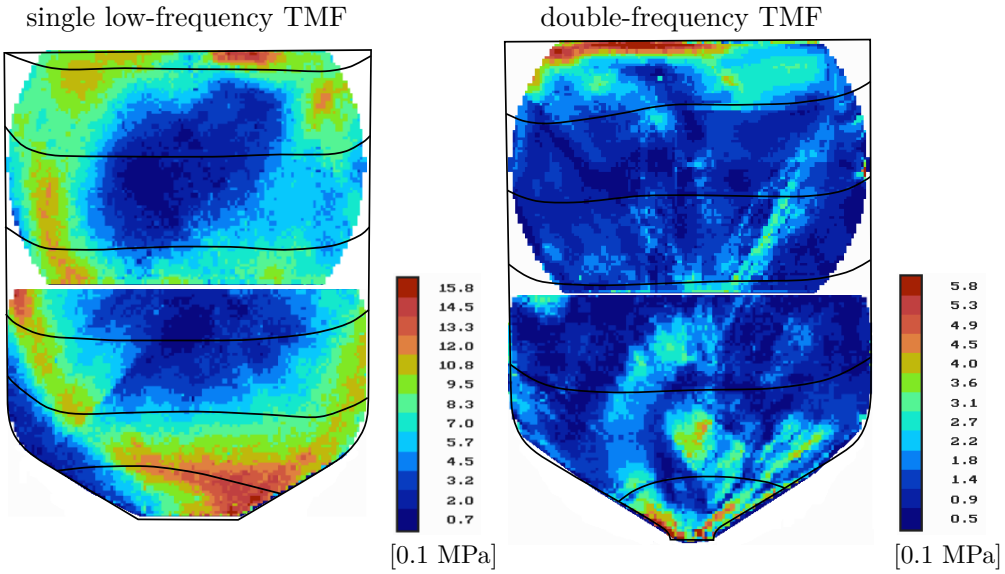

Figure 6.21: Measured residual stress distribution of two crystals grown under identical thermal condition but with different TMF parameters

The residual stress distribution in as-grown GaAs crystals with EPD values between 3300-7100 cm^{-2} was measured on subdivided longitudinal cross sections. In Fig. 6.21 the favorable influence of a steady double-frequency TMF with enhanced symmetry, diminished w-shape of the solid-liquid interface, and reduced bending near the crucible is demonstrated. In the picture the residual stress distribution of a crystal grown with a single low-frequency and a double-frequency TMF is compared. Additionally, the shape of the interface is drawn into the picture. Please note that the measurement equipment can only measure samples up to a diameter of 4 inch. That is the reason for missing parts of the crystal cylinder.

The crystal grown with the single low-frequency TMF showed an asymmetric interface shape in the crystal cone with an enhanced deflection near the crucible, leading to a large unequally distributed residual stress of up to 1.5 MPa in the as-grown crystal. Compared to this, the application of a double-frequency TMF led to a reduced concavity near the crucible with a more symmetric interface in the lower crystal part and subsequently reduced residual stress in the range of about 0.3 MPa. Rising asymmetry in the upper cylinder region caused an enhancement of residual stress. The measured EPD values of this crystal were slightly higher compared to the crystal grown with single-frequency TMF. Fig. 6.22 shows the measured residual

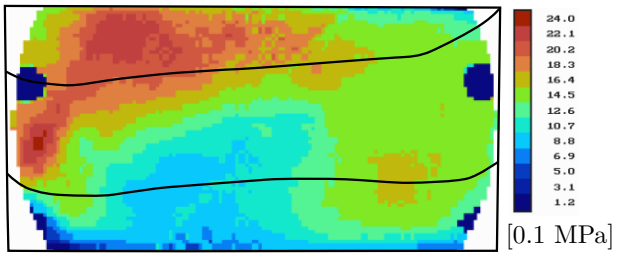

Figure 6.22: Measured residual stress distribution of a crystal grown with a steady double-frequency TMF, rising asymmetries of the interface shape in the upper region led to increasing residual stress values

stress distribution of the cylinder from another crystal grown with a steady double-frequency TMF. EPD values were lower in the range of 2300-2600 cm^{-2} compared to the upper crystals. The overall level of residual stress value was higher compared to the other crystals. Again, the rising asymmetry of the interface seemed to be responsible for the asymmetrical increase of the residual stress in the upper cylinder region. Values up to 2.4 MPa were reached.

Generally, the following observations were made: Asymmetric interfaces and interfaces with enhanced deflection near the crucible walls showed higher residual stress in these areas. Crystals grown with small growth velocities showed a decrease of residual stress values compared to standard growth conditions. Increasing dislocation densities provided relief of stress in the longitudinal cross sections.

Precipitates

The influence of TMF on precipitation was analyzed using LST/PL measurements on an as-grown GaAs:Si crystal, partially grown with and without TMF. No annealing steps were applied after growth. Precipitation of As occurs during cooling of the grown crystals at around 900° [Sch92]. Precipitates decorating dislocation lines form due to heterogeneous nucleation. Assembled LST/PL and IRT pictures of the crystal cone region are compared in Fig. 6.23. The transitions from growth with and without TMF were visible through interface marking.

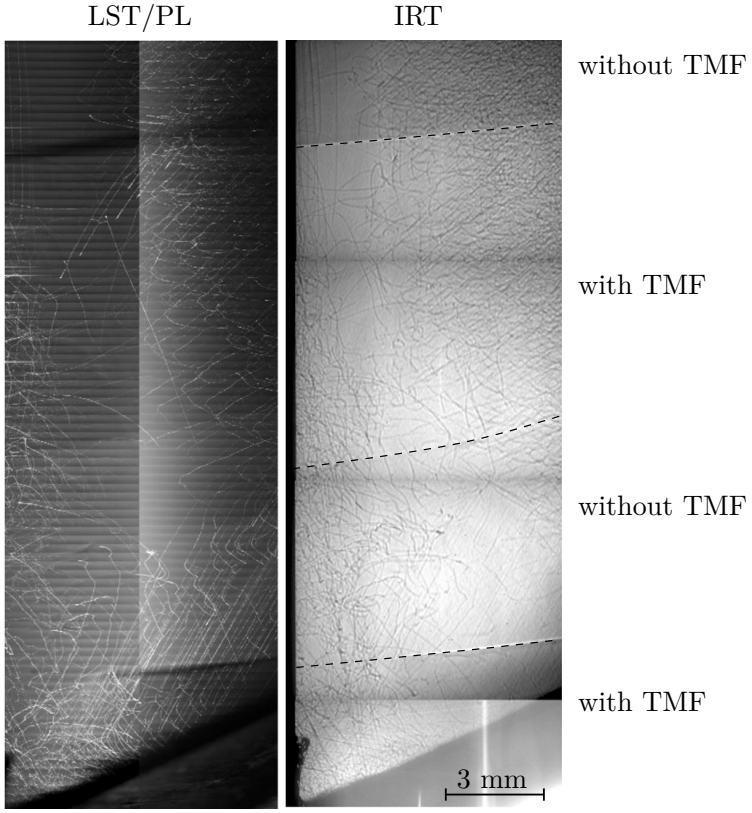

Figure 6.23: Comparison of assembled LST/PL and IRT pictures of the cone region of a crystal grown partially without TMF, the sample had a thickness of 15 mm (LST/PL measured with integrated depth of 5 mm)

The defect PL signal in the background of the LST/PL picture showed a varying concentration of the Si-V-complex through interface marking and in the facets. Dislocation lines were visible through scattering on decorating precipitates. In the IRT picture the progression of visible dislocations was identical. No differences in decorating precipitates between crystal areas grown with and without TMF were observed. Reason was the apparent agglomeration of As along dislocations during

cooling process. The TMF only affected the growth process, i.e. the shape of the solid-liquid interface. An influence on decorating precipitates is only possible via influencing dislocations itself, e.g. the precipitate size increases with decreasing dislocation density [Rud99]. No direct impact on the progression and generation of dislocations was detected when the TMF was switched on or off.

Small precipitates were also found in the crystal matrix with increasing crystal length. The number of decorating precipitates was reduced while number of matrix precipitates increased, correlating to enhanced Si incorporation with progressing growth [Nau06]. With a reduction of the dislocation density with progressing growth in GaAs:Si, diffusion length of As might be insufficient to reach dislocations and agglomerated on silicon in the crystal matrix.

6.2 Semi-insulating gallium arsenide

Figure 6.24: Pictures of two SI GaAs crystals grown with TMF: (left) steady double frequency TMF, (right) current-matched double frequency TMF

The occurrence of polycrystalline transition areas starting near the crucible wall significantly limits crystal length and process yield in VGF GaAs growth [Jur05]. This phenomenon is in particular often observed in VGF growth of SI GaAs, while it is by far less significant in VGF-GaAs:Si processes. The difficulty of the analysis of this phenomenon lies in the microscopic size of the crystal-crucible contact area. By taking the crystals out of the crucible, cutting, grinding and polishing, few 100 µm of the outer surface are lost. Therefore, the direct observation of alleged polycrystalline triggers like the Gibbs-Thomson effect, crucible disruptions, Gallium droplets, facet fluctuations, or the reduced B_2O_3 wettability of the crucible in the cylinder rim area, as reported in literature, is difficult.

In GaAs:Si growth experiments with applied TMF, steady flow velocities near the interface, a reduced dislocation density with a flattened solid-liquid interface, stable facets, and an increasing magnitude of the contact angle β were observed. Therefore, its positive influence on polycrystalline growth starting near the crucible wall might be anticipated. Furthermore, process-related issues were optimized as

far as possible. Before and after every growth process, the inner crucible surfaces were thoroughly examined for scratches and disruptions. Arsenic loss in the grown crystals was generally below <0.5‰ of the GaAs total mass.

6.2.1 TMF parameters applied for SI GaAs growth

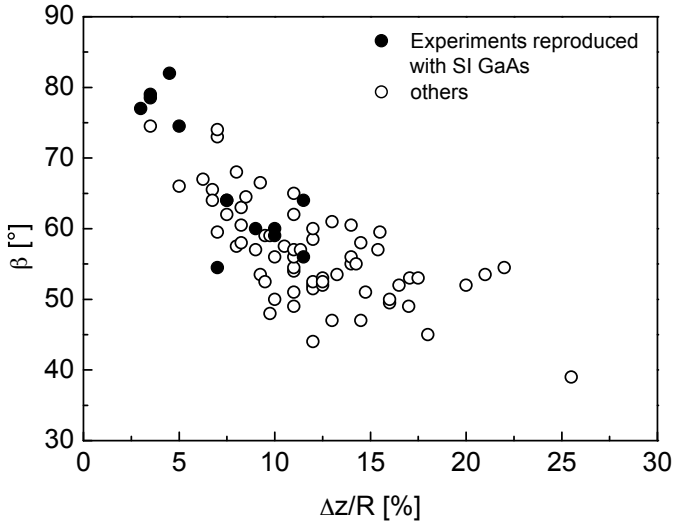

Figure 6.25: Measured values of average β-angles as a funcion of their corresponding interface deflection for different interface positions, taken from GaAs:Si single crystals grown in the single-crucible HMM setup for different TMF parameters and conventional growth conditions, filled circles represent GaAs:Si processes with optimized interface shapes which have been reproduced with undoped material

Two SI GaAs reference crystals were grown without TMF, one in the single-crucible HMM, the other in the multi-crucible HMM. Four SI GaAs crystals were grown in the single-crucible HMM as a reproduction with utilized TMF parameters and conventional growth conditions already applied in GaAs:Si growth experiments. In Fig. 6.25 the average values of β as a function of the associated interface deflections for conducted GaAs:Si growth experiments with various TMF parameters are summarized. Despite asymmetries and w-shaped interfaces, the minimization of the interface deflection was on average accompanied by an increase of β. In the picture, filled circles represent interfaces of GaAs:Si single crystals grown with optimized TMF parameters with small interface deflections and large contact angles. These growth experiments have been reproduced with undoped material. No marking of the solid-liquid interface was conducted during growth of SI GaAs. Aim was to supply steady and consistent flow conditions to avoid temperature fluctuations near the interface and to ensure stable growth conditions.

Pictures of two 7 kg SI GaAs crystals grown with a double-frequency TMF in the single crucible HMM are shown in Fig. 6.24. Crystals were hardly distinguishable from GaAs:Si from outside, except from the less pronounced facets in the crystal cone.

6.2.2 Properties of grown SI GaAs crystals

Figure 6.26: Typical polycrystalline triangle-shaped area of a SI GaAs crystal after sanding off a few microns of the surface: (left) overall image of a whole crystal cylinder, (right) detailed view of a polycrystalline transition area

Both SI GaAs reference crystals grown without TMF in the two different growth setups were not entirely monocrystalline. Polycrystalline growth started in the crystal cylinder. Four triangle-shaped polycrystalline areas were observed in both crystals, respectively, always developing near one of the <110>-directions in similar cylinder positions. No correlation between the polycrystalline starting areas and crucible defects were observed. Global basic growth conditions in both setups were not sufficient to prevent polycrystalline growth near the crucible walls. Noticeable was, that polycrystalline growth in the multi-crucible VGF setup started in the lower cylinder, while polycrystalline growth in the crystal grown in the single-crucible setup started later during the process in the center of the cylinder. Hence,

thermal growth preconditions in the growth setups had a major influence on development of polycrystalline areas. Presumably, due to the somewhat enhanced interface concavity in the multi-crucible setup, polycrystalline growth developed earlier.

Polycrystalline growth was not suppressed with the application of double-frequency TMF in the SI GaAs growth experiments. The achieved reduction of the interface deflection and the accompanied enhancement of the crucible contact angle were not yet sufficient to fall below the overall critical conditions for polycrystalline growth. The first transition area always developed within the same area of the crystal cylinder with and without applied TMF and independent from used TMF parameters. Therefore, the thermal asymmetry of the heater setting or hot zone layout was assumed to be on of the major triggers of this process. However, in some crystals grown with TMF, the number of polycrystalline areas was reduced to three and some polycrystalline areas developed later with progressing growth, further in the direction towards the crystal end. The surface of the crystals usually did not indicate any polycrystalline areas after taking the crystal out of the crucible (see Fig. 6.24). After sanding off a few microns, the surface showed radially spreading grain boundaries as can be seen in Fig. 6.26. Often there were 1-3 pointed areas in close vicinity to each other where the grains developed. The polycrystalline area continued growing and spreading radially. In the beginning grains usually were small and elongated on the outer crystal surface, while in the upper region some larger grains emerged.

Longitudinal sections were cut in <110>-direction, polished and analyzed with DSL etching and IRT measurements. The cuts were made across the assumed polycrystalline starting point. Results for a SI GaAs crystal grown with a steady double-frequency TMF are shown in Fig. 6.27. This typical polycrystalline area extended to only the outer quarter of the crystals, the rest was monocrystalline. Here, the typical globular dislocation cellular structure was visible. The size of the cells heavily fluctuated within the crystal. In the crystal cone and in the crystal periphery dislocation cells were usually smaller compared to the cylinder center. In the surrounding of the polycrystalline area cells became very small and the cellular structure eventually disappeared. The dislocation density significantly rose (see also Fig. 6.34 in the following subsection). A few dislocation bundles proceeded in growth direction from cone to crystal end.

The dislocation distribution and cell sizes were analyzed on KOH etched (half)-wafers. They were taken from the monocrystalline lower cylinder from a crystal grown with steady TMF and graphite susceptor (reproduction of growth process with interface shape Fig. 5.4 (right)) and a crystal grown with current-matched double-frequency TMF and BN susceptor (with assumed similar interface in cone and cylinder, see Fig. 5.25). In the crystal grown with steady TMF, cell sizes along the [110]-direction for different radial positions on the opposite side of the polycrystalline area were measured. Results are shown in Fig. 6.28. The average cell diameter decreased from center to wafer periphery from 2.9 to 1.9 mm, corresponding to dislocation densities in this area well below $<1000\ \mathrm{cm}^{-2}$ [Hur04].

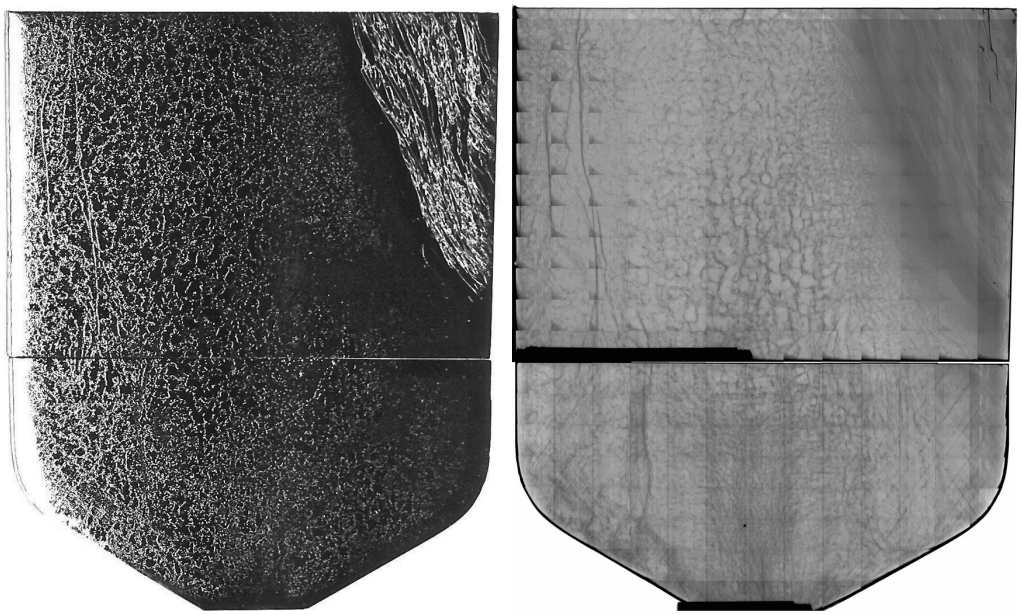

Figure 6.27: Longitudinal sections in <110>-direction of a SI GaAs crystal grown with a steady double-frequency TMF with a large polycrystalline area evolving in the crystal periphery: (left) DSL etched sample, (right) sample measured with IRT

Noticeable was the distinct increase of dislocation density and the absence of the cellular structure in the area where later the polycrystalline growth started (right area of the half-wafer). The local dislocation density significantly increased before the start of polycrystalline growth. Dislocation bundles were visible on the wafer in $[\bar{1}10]$-direction. As growth went further on, few centimeters later in this direction polycrystalline growth developed, too. A stable cellular structure developed in the area where no polycrystalline growth was observed. In the crystal grown with current-matched TMF, cell sizes along the [100]-direction were determined (Fig. 6.29). Here, average cell sizes were in the range 0.9-1.1 mm, corresponding to dislocation densities around 1000 cm^{-2}. Compared to Fig. 6.28, the cell size distribution was more homogeneous on the wafer. Dislocation bundles, closely arranged parallel dislocations, were visible in all <110>-directions. These bundles were most pronounced in the three directions, where polycrystalline growth started first (upper left, upper right and lower left area). Here, similar to Fig. 6.28, the dislocation cells disintegrated in the <110>-directions.

The application of different TMF parameters during growth led to different average EPD values in the monocrystalline lower cylinder areas. While in the crystal grown with steady double-frequency TMF and graphite susceptor the average EPD was 3580 cm^{-2}, the reduction of the concavity through application of a current-

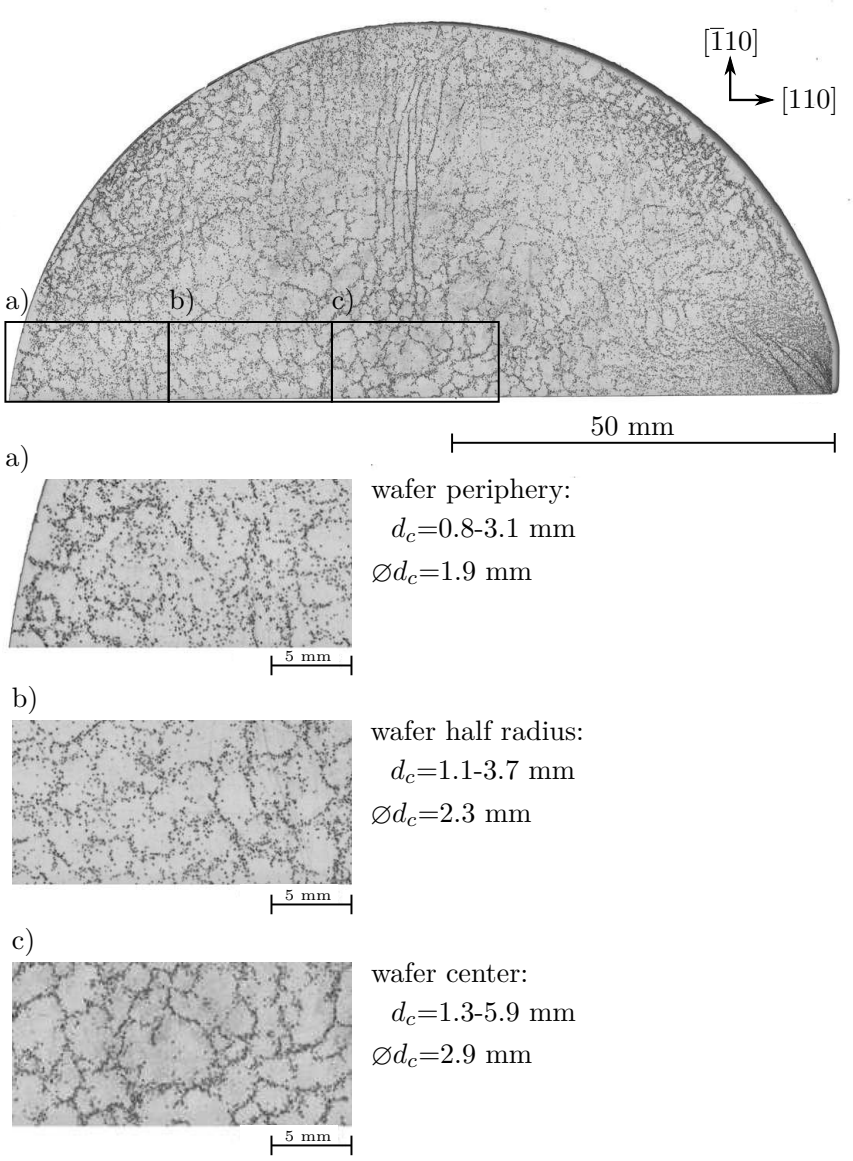

Figure 6.28: Dislocation distribution and cell size analysis for different radial positions along the [110]-direction on a half-wafer from a SI GaAs crystal grown with steady double-frequency TMF, the half-wafer was cut 5 mm below the start of the first polycrystalline transition area

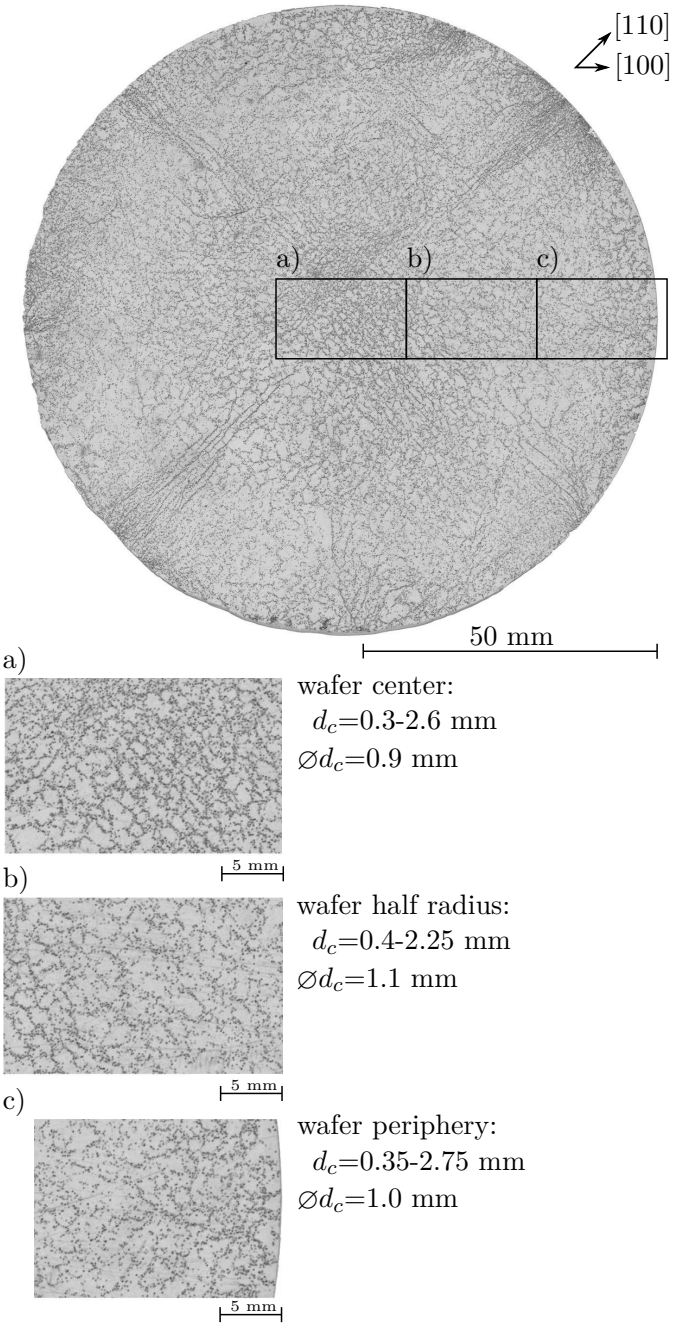

Figure 6.29: Dislocation distribution and cell size analysis for different radial positions along the [100]-direction on a wafer from a SI GaAs crystal grown with current-matched double-frequency TMF, the wafer was cut 25-35 mm below the start of the three polycrystalline transition areas

matched double-frequency TMF and a BN susceptor led to a reduced average EPD of 2120 cm^{-2}. This value is closer to reported average EPDs from industrially grown 4" VGF SI GaAs with around 1330 cm^{-2} [Bue01].

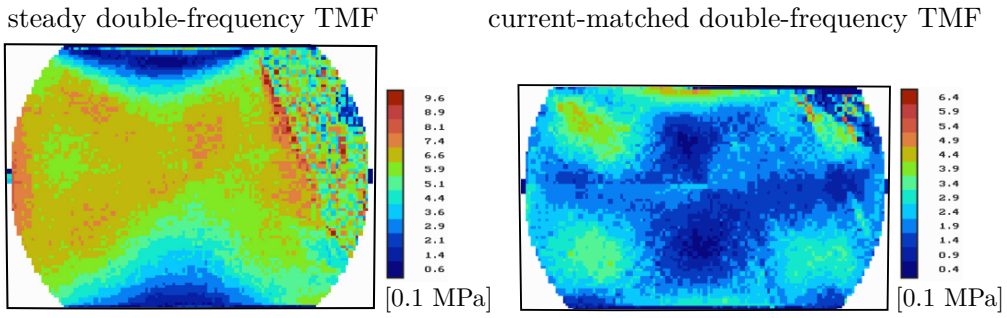

Figure 6.30: Comparison of measured residual stress in cylinder areas of longitudinal cross sections in <110>-direction of SI GaAs crystals grown with a steady double-frequency TMF and a current-matched double-frequency TMF

The measured residual stress in cylinder areas of longitudinal cross sections in <110>-direction of crystals grown with a steady double-frequency TMF and a current-matched double-frequency TMF are compared in Fig. 6.30. Both crystals were grown with applied graphite susceptor and identical standard growth recipe. In the upper right area rising and unequally distributed stress due to the polycrystalline growth was observed in both samples. Apart from that, the residual stress was rather equally distributed in the crystal cylinder. Average stress values in the crystal grown with steady double-frequency TMF were with 0.6 MPa higher compared to the crystal grown with current-matched double-frequency TMF. Here, the prevention of a w-shaped and asymmetric solid-liquid interface led to a decrease of residual stress to average values of 0.25 MPa. A correlation of the residual stress level on the tendency of polycrystalline growth was not observed.

6.2.3 Investigations on polycrystalline growth

Further analyses on the polycrystalline formation mechanisms were conducted based on the observed absence of the cellular structure and enhanced dislocation densities in <110>-direction before polycrystalline growth started. Laser scattering tomography was applied to investigate generation, progression, and types of dislocations, as well as grain boundaries in the transition areas. Polycrystalline areas from four grown SI GaAs crystals were analyzed.

The LST sample structure is depicted in Fig. 6.31. The polycrystalline areas were cut from the crystals. Two view modes were utilized. The tangential view provided a lateral view on polycrystalline structure, while the radial view provided analyses perpendicular to it. Polycrystalline areas in the analyzed SI GaAs crystals

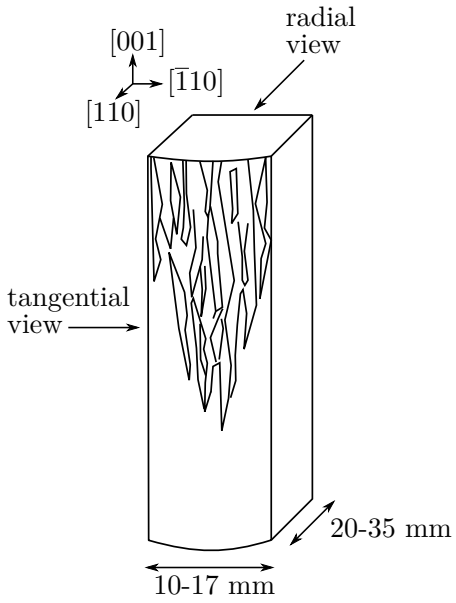

Figure 6.31: Sample structure for LST measurements with geometry, directions and applied view modes

grown with different TMF parameters and different susceptor materials did not show significant differences in their structure. The properties outlined in the following were observed in every analyzed polycrystalline transition area.

Fig. 6.32 shows a tangential and a radial view on a polycrystalline transition area, assembled from several individual LST measurements. With LST analyzed monocrystalline crystal areas showed reduced dislocation densities and the typical cellular structure. Remains of the dislocation cellular structure were visible in the lower part of both pictures. This cellular structure started to dissipate around 15-20 mm prior to the point where visible grains developed. Very high dislocation densities were observed inside and in the surroundings of the polycrystalline area (see also Fig. 6.34 for a more detailed view). No single starting point of polycrystalline growth in the vicinity of the crucible was observed, no indications of a heterogeneous nucleation in the supercooled area through crucible disruptions were found. The pictures revealed, that the multitude of small polycrystalline areas near the crucible in the vicinity of the <110>-direction started through accumulation of similar dislocations and the subsequent formation of small angle grain boundaries. The progression of polycrystalline areas followed the progression of the flattening interface and rounded wedge-shaped structures developed.

Fig. 6.33 (left) shows a close-up taken in a tangential view directly before grain boundaries were visible. Here, a dense multitude of parallel curved dislocations was observed, which fluently merged into the polycrystalline area, visible in the upper right of this picture. Some LST pictures even showed monocrystalline sections inside

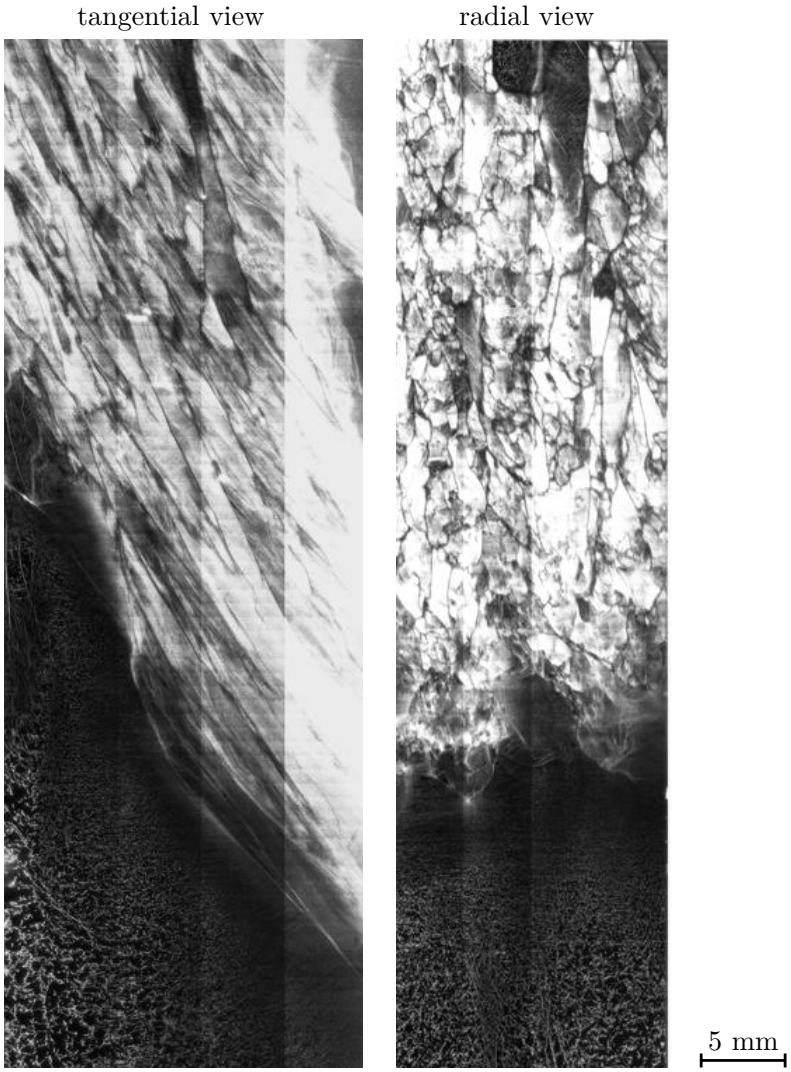

Figure 6.32: Overview of a polycrystalline transition area: (left) tangential view with crucible is on the right side, (right) radial view around 5 mm away from the crystal rim

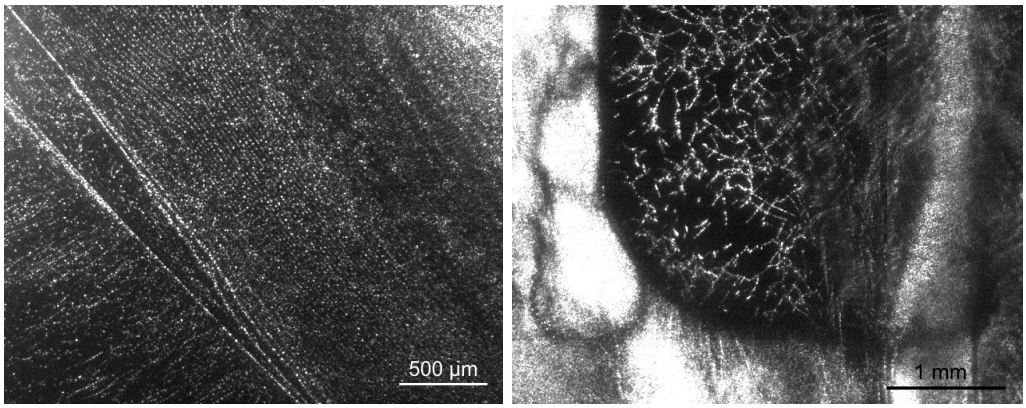

Figure 6.33: Detail pictures taken from radial and tangential view: (left) a multitude of parallel curved dislocations fluently merging into the polycrystalline area, (right) enclosed monocrystalline area surrounded by grain boundaries and areas with significantly enhanced dislocation density

the polycrystalline areas. Fig. 6.33 (right) shows a detail taken from the radial view in 6.32. The monocrystalline area, with a significantly reduced dislocation density compared to the surrounding grains, even contained a cellular-like structure. Locally confined monocrystalline areas within the transition area indicated several origins of polycrystalline growth, which might enclosed single crystal domains with original crystal orientation with progressing growth. Further analyses on the orientation of these domains remain to be carried out.

Fig. 6.34 shows a magnified view on the behavior of dislocations near the polycrystalline area. Generally, a restructuring of the dislocations was observed below the polycrystalline areas. Dislocations were bundling and forming dislocation walls proceeding perpendicular or increasingly perpendicular to the growing interface and ultimately leading into the polycrystalline area. A multitude of these structures was observed in surroundings of the polycrystalline area. These dislocation walls were also observed on the KOH etched wafers shown in Figs. 6.28 and 6.29. The formation of dislocation bundles consisting of a high number of parallel glide dislocations along [110] and [1$\bar{1}$0] directions was also described in GaAs crystals grown with LEC and VCz methods [Tow91, Shi93, Rud04]. Here, their generation and multiplication was associated with inclusions like Ga droplets or the accumulation of stress-induced dislocations. Within the framework of this investigation it was found that the observed dislocation bundles in the grown VGF crystals are consisting of grown-in dislocations. In the following, they are referred to as grown-in lineages.

A detailed overview on the observed transitions from enhanced dislocation densities to polycrystalline growth is shown in Fig. 6.35. Sections (a)-(d) show the progression of dislocations towards the polycrystalline area. The depicted area originated few millimeters away from the crystal rim, because here a continuous obser-

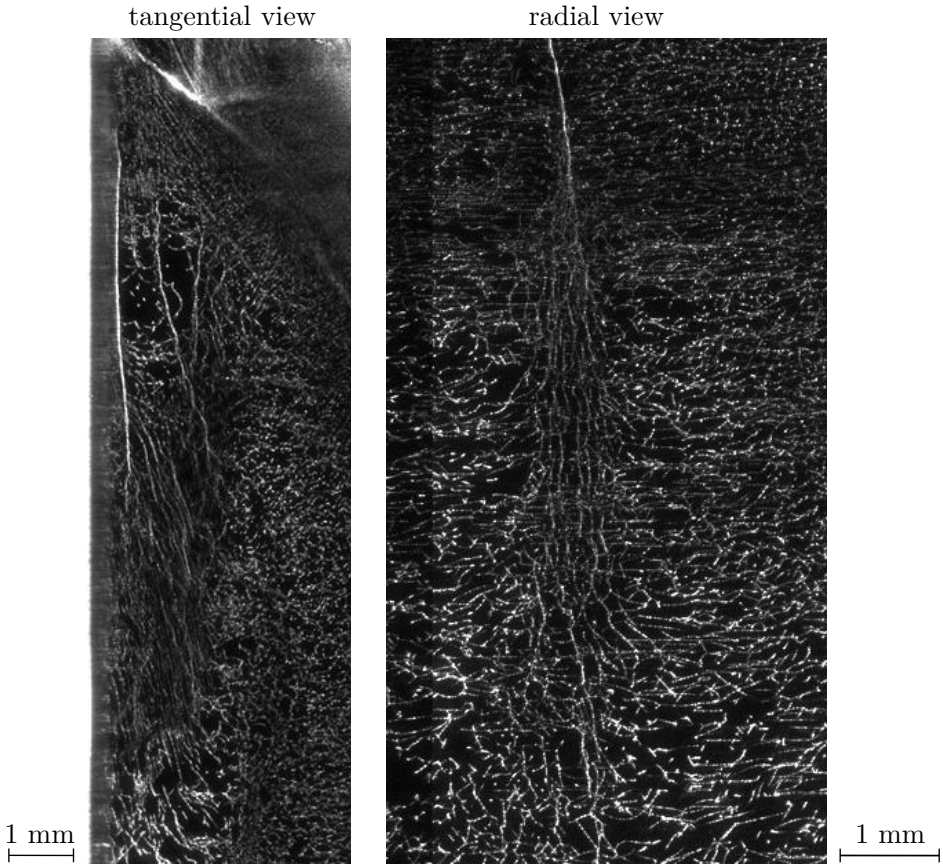

Figure 6.34: Details taken near the periphery of the polycrystalline area showing high dislocation densities and bundling of dislocations, (left) tangential view, (right) radial view

vation was easier accessible. Nevertheless, the depicted structures were observed in large numbers in close vicinity around the whole polycrystalline area, including the rim. First, glide dislocations dominated inside the crystals (a), which were generated shortly behind the solid-liquid interface during growth due to thermal stress. They started growing as grown-in dislocations as the glide-dislocations reached the growing interface [Oga89]. The number of glide dislocations was significantly reduced. The growth direction of the grown-in dislocations gradually changed from the diagonal direction of the glide plane to become more perpendicular to the concave interface with progressing growth (b, c). Adjacent grown-in dislocations started to couple and bundle (d). The enhanced parabolic interface morphology near the crucible walls promoted the formation of these grown-in lineages (see also Fig. 6.20 (right) for comparison). The grown-in lineages coalesced and small angle grain

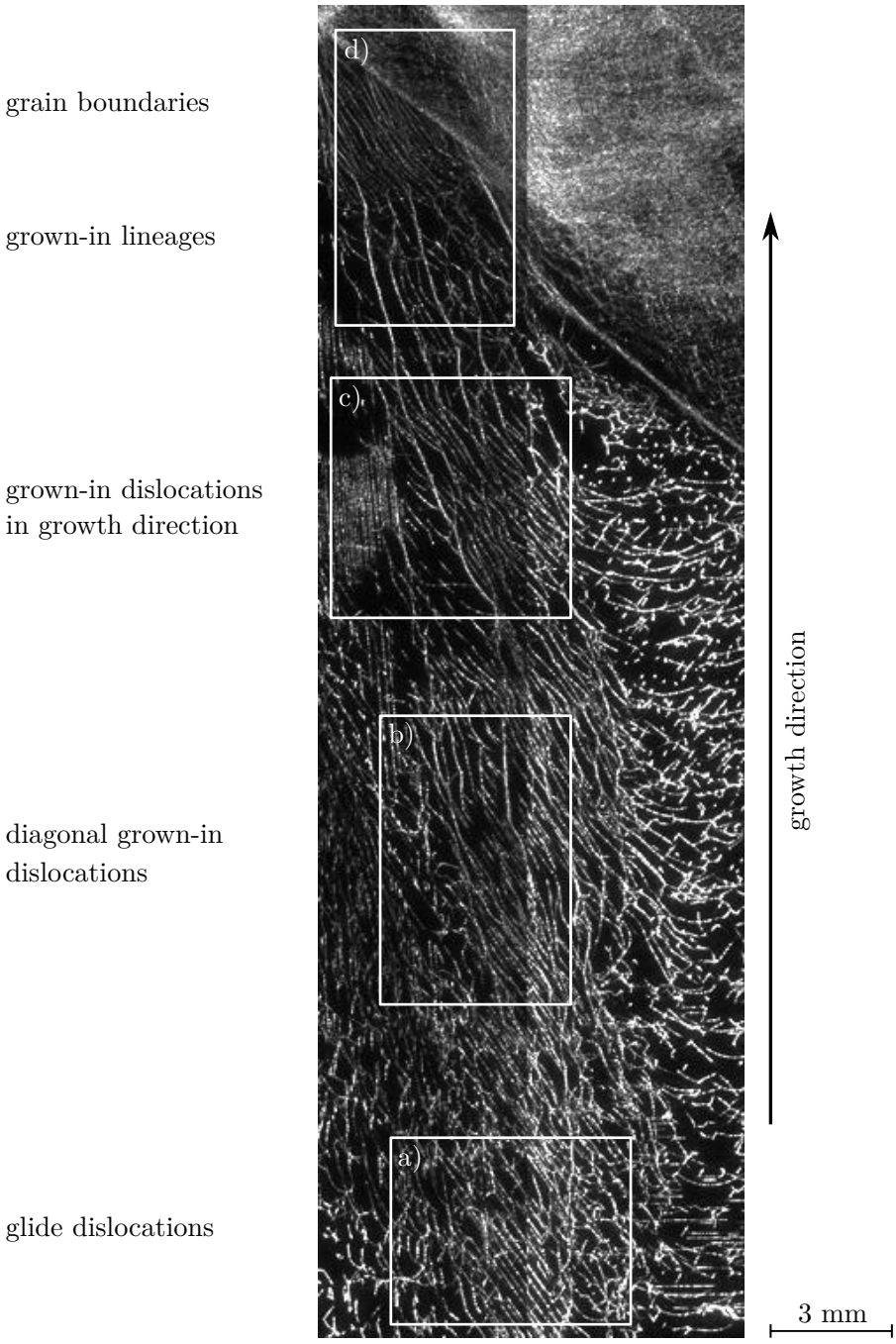

Figure 6.35: Overview on the transition from enhanced dislocation densities to polycrystalline growth

boundaries developed (d). Later, the tilting between the grains increased and large angle grain boundaries were formed.

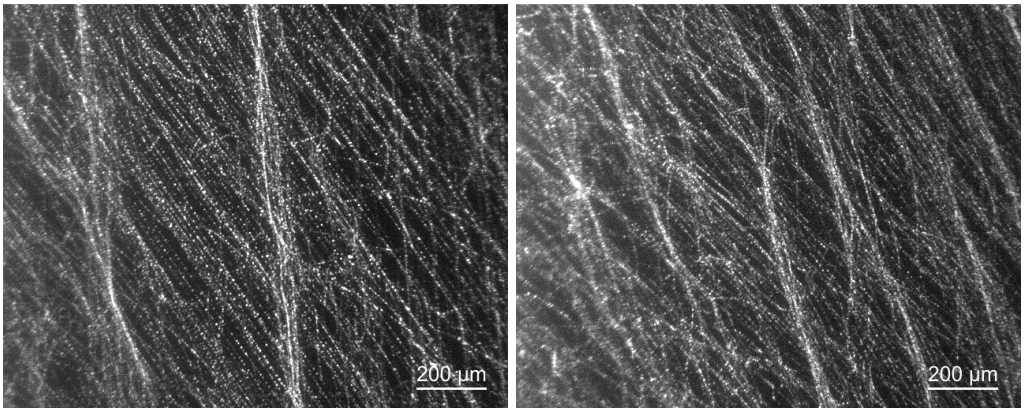

Figure 6.36: Detail pictures taken from radial and tangential view: (left) detail of a radial view taken below the start of a polycrystalline transition area showing mainly glide dislocations, (right) detail of a radial view taken near the start of a polycrystalline transition area showing enhanced bundling of grown-in dislocations

The pictures in Figs. 6.36 and 6.37 show a more detailed view on the transition from glide to grown-in dislocations during the growth process. Depth integrated LST pictures helped to prepare a three-dimensional layer-by-layer overview on selected areas of a crystal section. A proper assignment of the progression of the dislocations to specific glide planes and directions was possible. While below the start of a polycrystalline transition area mainly glide dislocations in one {111} glide plane were visible, with progressing growth more grown-in dislocations were formed with an advancing deviation from this glide plane. In Fig. 6.37 (right) the growth of the grown-in dislocations into grown-in lineages is noticeable.

In summary, IRT measurements, DSL etching, and KOH etching revealed a partial increase of the dislocation density before polycrystalline growth started. LST measurements helped to find indications that polycrystalline growth originated from the locally enhanced generation of glide dislocations in <110>-direction. Further, the transformation from glide dislocations to grown-in dislocations with progressing growth and their accumulation caused the generation of small angle grain boundaries, which ultimately led to polycrystalline growth. Several starting points were observed, no evidence was found that temperature fluctuations, facet breakdown, or dislocations inside the facets near the three-phase boundary were involved. Process related reasons for the significantly enhanced likeliness of polycrystalline transitions in SI GaAs compared to GaAs:Si can be doubted due to growth process reproductions and the assumed similarity of heat dissipation, asymmetries, and TMF action in doped and undoped material. Through the material specific lack of Si/B

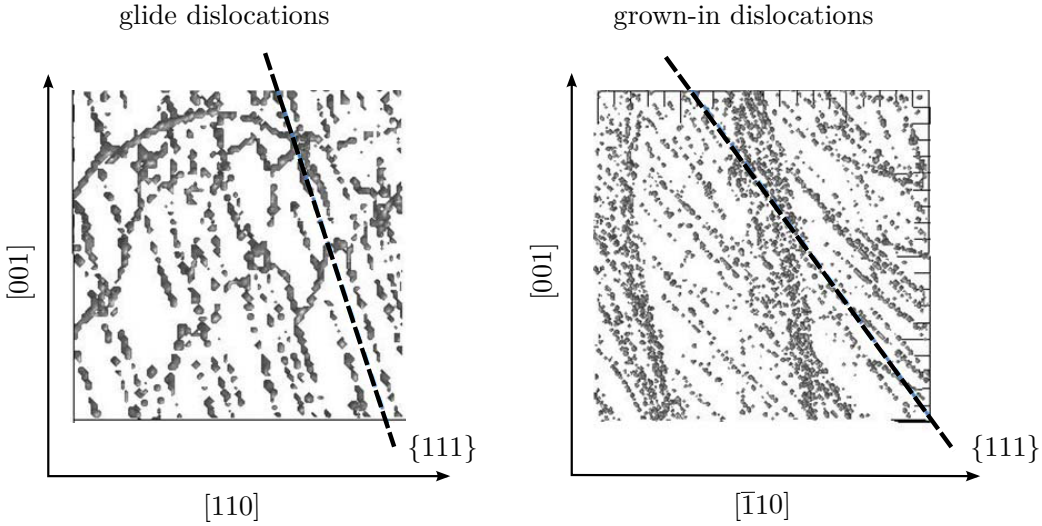

Figure 6.37: Dislocation arrangement reconstructed from a 3D layer-by-layer data set prepared with LST: (left) glide dislocations in one {111} glide plane below the start of a polycrystalline transition area, (right) grown-in dislocations clinging together into grown-in lineages

incorporation in undoped GaAs, the increase of the dislocation density and their arrangement was assumed to be responsible for the increase in probability of polycrystalline growth. It is known that the number of grown-in dislocations in SI GaAs is generally higher compared to GaAs:Si [Sek78, Gil86].

The local interface concavity near the crucible wall and thermal asymmetries have to be further reduced to prevent the generation of glide dislocations, their transformation to grown-in dislocations, and the subsequent bundling and development of grown-in lineages. Especially the conventional growth conditions need to be adjusted to match these requirements. A reduction of the growth velocity or alterations of the crucible support could improve the axial heat transfer in the lower crystal cylinder and crystal cone to further reduce thermal stress.

7 Summary and Conclusion

Within the framework of this thesis, Si-doped and semi-insulating 4" VGF-GaAs crystals were grown under the influence of TMF. First, the general interface shaping potential of a TMF as a function of its parameters was analyzed by growing GaAs:Si. Here, analyses of the varying solid-liquid interface shapes were feasible using the TMF interface marking technique. The shape of the solid-liquid interface reacted sensitively on modifications of TMF frequencies, phase shifts, and current magnitudes. The results of the TMF parameter study constituted the basis of the successful growth of GaAs single crystals in the HMM with a continuously reduced interface deflection by about 30% and with increased crucible-contact angle β within the order of 10%, compared to the growth without TMF. According to the presented observations, the following TMF conditions must be given to reduce the concave deflection of the solid-liquid interface:

- application of TMF frequencies between 10-200 Hz
- simultaneous utilization of a low- and a high-frequency TMF ($f_1 \approx 10 \times f_2$)
- a uniform phase shift between 90-100° or a non-uniform phase shift with 80°/120°
- low frequency AC share I_1 >> high frequency AC share I_2
- minimum of around B_0=1.5 mT for a distinct change of solid-liquid interface shape under standard growth conditions
- matching of the AC to the progress of solidification to compensate variations of the Lorentz force density distribution with varying melt height

However, unoptimized TMF parameters led to an enhancement of undesired interface asymmetries. Conventional growth conditions were adjusted to further improve interface morphologies. By replacing graphite with isotropic BN as susceptor material, the radial heat dissipation was decreased through its lower thermal conductivity and the local curvature near the crucible wall was further reduced. The best achieved shape of the solid-liquid interface showed average measured concave deflections around 4% with accompanied β-angles around 80°.

Positive synergy effects of TMF application on different process intensification approaches were initialized in GaAs:Si growth experiments. The yield of the growth processes increased. Within the scale-up approach, the ingot mass was notably enhanced from standard 5-7 kg to 9 kg. The benefiting impact of growth-matched

double-frequency TMF parameters on the interface shape was transferred from standard processes without difficulties. Results indicated, that setup specific enhanced thermal asymmetries with rising crystal length can be counterbalanced with pertinent TMF parameters. Growth velocities were enhanced to up to 5.0 mm/h within the speed-up approach. It was found that the TMF strength needs to be increased and matched to the amplified process velocity, to efficiently flatten the radial thermal gradients in the melt. Crystals grown with high growth rates and not correspondingly increased TMF strength showed enhanced interface concavities accompanied by a rising tendency of polycrystalline growth. For numbering-up of the VGF process, a new growth setup with a multi-crucible HMM, which embraced all four crucibles, was put into operation. Test runs in one crucible position revealed radially uniform and almost symmetric solid-liquid interfaces with applied single- and double-frequency TMF. Applied TMF parameters could not directly be transferred one-on-one from the single-crucible setup, but first basic parameter studies showed analogical qualitative behavior when frequency shares were altered. Two 4" VGF-GaAs:Si single crystals were simultaneously grown under the influence of a double-frequency TMF. A temperature offset and varying thermal gradients in the two opposing crucible positions resulted in a deviation of growth velocities of 8-10% and a height shift of respective interface positions by about 15 mm. Obtained values of deflections and crucible-contact angle in all crystals grown in the multi-crucible HMM were comparable to results from growth in the single-crucible setup when a graphite susceptor was applied. Structural compensation of deviations in every crucible position, enhanced axial heat dissipation, and the application of a BN susceptor in the multi-crucible HMM should lead to similar results in both VGF growth setups.

General changes in electronic and structural crystal properties through the application of different TMF parameters were analyzed in grown GaAs:Si single crystals. The application of a double-frequency TMF markedly reduced temperature fluctuations near the solid-liquid interface. The formation of growth striations was extensively suppressed under optimized homogeneous flow conditions in both the single- and multi-crucible setup. The TMF parameters needed to be carefully adjusted and ideally matched to the different process phases to obtain a mostly striation free crystal. Strong TMF with magnetic Taylor numbers $Ta_m > 1{\times}10^6$ and a high frequency led to time-dependent melt flow and the appearance of regular striation patterns. Irregular striations were again observed when the growth velocity was enhanced to >3.0 mm/h and the TMF strength was not correspondingly amplified.

Experimental and numerical findings indicated an enhancement of the Si incorporation due to the reduction of flow velocities with TMF. The TMF induced convection opposed the natural convection. Furthermore, TMF induced melt flow towards the crystal axis with low flow velocities contributed to the enhancement of the Si incorporation in this area. The radial charge carrier density profiles were flattened by the reduction of the concave deflection with applied TMF.

The TMF-induced change of the melt flow as well as the flattening of the interface shape had positive influence on further structural properties of the grown GaAs:Si single crystals. Facets lengths were stable under steady flow conditions with an applied double-frequency TMF. When the TMF was switched off, unsteady melt flow led to irregular facet lengths and to their breakdown. Dislocation densities in the grown crystals were reduced through a combined optimization of the conventional thermal layout and a reduction of the interface deflection near the crucible wall with TMF application. Average low EPD values around 100 cm^{-2} were obtained for growth with a current-matched double-frequency TMF and applied BN susceptor in the single-crucible growth setup. Average EPDs around 500-1000 cm^{-2} were reached in the simultaneously grown crystals in the multi-crucible growth setup with applied graphite susceptors. Thermal asymmetries during growth and cooling process need to be avoided in order to prevent the generation of glide dislocations in the crystal periphery. Crystal sections with asymmetric interfaces and interfaces with strong concavities showed enhanced residual stress. A decrease of the magnitude of residual stress was observed for crystals grown with small growth velocities and in crystals with an enhanced dislocation density.

Conducted SI GaAs growth experiments focused on the transfer of optimized conventional growth conditions and TMF parameters from GaAs:Si growth to reduce the occurrence of polycrystalline growth in VGF SI GaAs. The achieved reduction of the interface deflection and the accompanied enhancement of the crucible contact angle with a double-frequency TMF as well as the adjustment of the conventional growth conditions were not yet sufficient to fall below the overall critical conditions for polycrystalline growth. These conditions were found to be mainly predetermined by the thermal setup of the VGF furnaces. However, in some SI GaAs crystals grown with TMF the number of polycrystalline areas was reduced and developed in later stages of growth compared to reference crystals grown without TMF. Several locally confined wedge-shaped polycrystalline areas were observed near the crucible walls in <110>-directions within the cylinder of the grown SI GaAs crystals. Before polycrystalline growth started, the crystals grown with TMF showed average EPD values around 2100-3600 cm^{-2} and cellular dislocation structures up to several millimeters in diameter. Residual stress levels inside the crystals were low. A comprehensive investigation with LST measurements revealed new insights about origins and triggers of polycrystalline growth. Locally enhanced thermal stress, e.g. through minor interface asymmetries, caused a partial increase of glide dislocations in <110>-direction near the crucible wall with progressing growth. They acted as origin of grown-in dislocations when they reached the growing interface. Grown-in lineages formed through bundling due to the parabolic interface deflection in the crystal periphery. Small angle grain boundaries developed, which ultimately led to polycrystalline growth.

8 Outlook

The shape of the solid-liquid interface highly depends on conventional growth conditions, like growth velocity, thermal insulation, hot zone and crucible materials. Outstanding is the fact, that the utilization of a double-frequency TMF provides a tool to reduce the interface deflection independent from the given global growth conditions. In future experiments, especially the strong local bending in the crystal periphery, which is mainly caused by the anisotropic thermal conductivity of the pBN crucible, is aimed to be reduced to further flatten the interface near the crucible wall. A gentle adjustment of high-frequency TMF parameters is inevitable, because of its enhanced impact near the crucible wall. However, one has to take note that critical flow conditions can be easily exceeded with larger high-frequency TMF shares. Here, the danger of time-dependent melt flow and an asymmetric interface shape significantly rises. In particular asymmetries of the solid-liquid interface, evoked by thermal setup and by TMF, have to be strictly avoided in order to eliminate glide dislocations to further reduce the EPD in the GaAs crystals.

To enable the use of stronger high-frequency TMF, alterations of the HMM, e.g. the further reduction of the size of the HMM bus bars, are conceivable to minimize TMF induced asymmetries. Furthermore, structural modification of the thermal setups, e.g. changes of the crucible support material or thermal insulation, could reduce thermal asymmetries and promote axial heat transfer. At present, experiments with low density pBN crucibles are planned. Their thermal conductivity is significantly reduced [Shi09], which helps to inhibit heat removal through the crucible. Other electrically insulating susceptor materials shall be tested, too. A slightly enlarged diameter of the susceptor would prevent a direct crucible contact and could lead to decreased radial heat dissipation.

Enhanced thermal symmetry and further reduced interface deflections should also increase the yield in SI GaAs growth. The generation of glide dislocations, their transformation to grown-in dislocations and the subsequent bundling would be avoided, the probability of polycrystalline growth would be reduced. Further analyses on the origin of the enhanced risk of polycrystalline growth in SI GaAs growth should give further leads to its prevention.

While the principle applicability of a TMF to influence the interface shape with enhanced growth velocities was experimentally shown, the impact of stronger growth-matched double-frequency TMF in connection with a BN susceptor has to be studied. Aim is to identify the highest possible growth rates with TMF application before crystal properties impair compared to standard processes. Future strategies on process intensification with TMF lie in the consolidation of the different approaches. Without any structural modifications the maximum feedstock mass in the single-

crucible HMM lies around 10 kg. Due to the increased height of the multi-crucible HMM, longer crucibles can be used for a maximum GaAs feedstock mass of up to 13 kg, without the melt emerging out of the HMM. For enhanced melt heights, modifications of the multi-crucible growth setup in insulation and HMM, as well as heater power adjustments for larger axial thermal gradients are necessary to improve axial heat dissipation. Differences in temperature profiles in the four crucible positions have to be structurally equalized and TMF parameters have to be improved. A shift of the crucible positions further into the HMM may introduce a further enhanced TMF impact on the melt. Ultimate goal would be the simultaneous growth of four 13 kg SI GaAs single crystals with enhanced growth velocity with the use of a TMF.

In addition to further adjustments of TMF parameters, other variations of non-steady magnetic fields can be employed in the HMM without any structural setup refurbishments. 3D numerical studies investigated the potential of pulsed traveling magnetic fields (PTMF) [Dro14a]. Aim was the enhancement of the homogeneity of Lorentz force density distribution and radial temperature distribution on induced rotational asymmetries in the GaAs melt due to the HMM design. Numerical results showed that with a sinusoidal modulation of the AC with certain PTMF parameters a more planar radial temperature distribution can be obtained compared to conventional TMF application. Experimental analyses on utilized PTMF during VGF-GaAs growth are targeted. Furthermore, alternating magnetic fields (AMF) can be easily generated by setting the phase shift between the HMM coils to 0°. Resulting Lorentz force densities would point towards the crucible axis, perpendicular to the crucible wall. Resulting melt flow would be directed towards the center, too. Experimental analysis remains to be done, if the interface can be leveled out in the crystal periphery. Combinations between a low-frequency TMF, to gain a convex shape in the crystal center, and a high-frequency AMF for an enlarged force action with small penetration depths seem thinkable. Equally, the combined use of magnetic fields and ultrasonic vibration could enhance control on segregation, e.g. the diffusion boundary layer thickness along the axis could be reduced to further flatten the radial dopant incorporation profiles.

Beyond that, structural alterations of the HMM itself, e.g. the conversion of the inductive top heater into an additional HMM coil, could generate Lorentz force densities inside the melt with an direction towards the crucible walls. A melt flow from the center towards the critical triple point area could lead to convex interface shapes.

Appendix

Overview of the conducted growth experiments - single-crucible setup Kronos:

Experimental focus	Number of experiment	Growth conditions
Test runs - initial startup, seeding	V001, V002, V003	growth recipes 1.0 and 1.1, adjustments of growth recipes with respect to temperature profile measurements
Examination and testing of the marking technique	V004, V005	identical growth recipe 2.0, TMF switched on whole process, study on TMF parameter control and effects on interface
Comparision with and without TMF	V006, V007	identical growth recipe 2.0, growth either without or with steady TMF
Partially with and without TMF	V009, V031	different growth recipes 3.0 and 4.1, partial switching on of the TMF (steady and matched)
TMF parameter studies: frequency	V015, V016, V018, V019	identical growth recipes 4.0 (5 kg) and 4.1 (7 kg), varying GaAs masses and respective B_2O_3 content
TMF parameter studies: phase shift	V008, V024, V025	different growth recipes 2.0 and 4.1, varying GaAs masses
TMF parameter studies: current	V015, V016, V021	identical growth recipes 4.0 (5 kg) and 4.1 (7 kg), varying GaAs masses and respective B_2O_3 content
Matching of TMF parameters with progressing growth, focus on reduction of w-shape and asymmetry	V026, V028, V031, V035, V036, V037, V038	standard growth condition with recipe 4.1, partially grown with BN susceptor with adjusted growth recipes 5.0 and 6.0

Asymmetry effects	V008, V018, V019	different growth recipes 2.0 and 4.1, varying GaAs masses, influence of current, phase, and frequency on asymmetry effects
Test of BN susceptor	V033, V036, V037, V038, V040, V041	V033 with small axial gradients and growth recipe 5.0, others with standard growth conditions with adjusted growth recipes 6.0
Scale-up	V038	reproduction of V037, 9.1 kg, 2.0 mm/h, growth recipe accordingly extended
Speed-up	V022, V023, V024	recipe 4.1 up to 2.6 mm/h, recipe 4.2 up to 4.0 mm/h and recipe 4.3 up to 5.0 mm/h, identical thermal conditions, identical TMF parameters
SI GaAs	V020, V028, V037, V040, V041	reproductions of GaAs:Si growth processes with TMF, no marking of the interface, V041 is a reference crystal grown without TMF

Overview of the conducted growth experiments - multi-crucible setup ECM:

Experimental focus	Number of experiment	Growth conditions
Test runs - initial startup, seeding position	MECM01A, MECM02A, MECM03A, MECM04A	different growth recipes ECM-1.0, ECM-1.1, ECM-1.2 and ECM-1.3, TMF parameters from taken from Kronos, steady single- and weak double-frequency TMF
Adjustment of conventional growth conditions	MECM06A, MECM07A	growth recipes ECM-2.0, ECM-2.1,
Numbering-up	MECM05AC	growth recipe ECM-1.4, reproduction of MECM04A
Comparison small and large high-frequency share	MECM07A, MECM08A	growth recipe ECM-2.1
SI GaAs	MECM09A	growth recipe ECM-2.1, reference crystal grown without TMF

Bibliography

[Alb97] T. Alboussière, A. C. Neubrand, J. P. Garandet and R. Moreau. Segregation during horizontal Bridgman growth under an axial magnetic field. Journal of Crystal Growth 181, 133–144 (1997).

[Alt91] H. C. Alt and M. Maier. Assessment of the boron impurity in semi-insulating gallium arsenide by localized vibrational mode spectroscopy. Semiconductor Science and Technology 6, 343 (1991).

[Alt96] M. Althaus. Some new design features for vertical Bridgman furnaces and the investigation of small angle grain boundaries developed during VB growth of GaAs. Journal of Crystal Growth 166, 566–571 (1996).

[Amo98] J. Amon, F. Dumke and G. Müller. Influence of the crucible shape on the formation of facets and twins in the growth of GaAs by the vertical gradient freeze technique. Journal of Crystal Growth 187, 1–8 (1998).

[Amo99] J. Amon, J. Härtwig, W. Ludwig and G. Müller. Analysis of types of residual dislocations in the VGF growth of GaAs with extremely low dislocation density (EPD«1000cm-2). Journal of Crystal Growth 198-199, 367–373 (1999).

[Bas97] I. Bassignana. Variation in the lattice parameter and crystal quality of commercially available Si-doped GaAs substrates. Journal of Crystal Growth 178, 445–458 (1997).

[Bel04] M. Bellmann, O. Pätzold, U. Wunderwald and A. Cröll. Axial macrosegregation in Ga-doped germanium grown by the vertical gradient freeze technique with a rotating magnetic field. Crystal Research and Technology 39, 195–199 (2004).

[Bir00] B. Birkmann, M. Rasp, J. Stenzenberger and M. Müller. Growth of 3" and 4" gallium arsenide crystals by the vertical gradient freeze (VGF) method. Journal of Crystal Growth 211, 157–162 (2000).

[Bir02] B. Birkmann, R. Weingärtner, P. Wellmann, B. Wiedemann and G. Müller. Analysis of silicon incorporation into VGF-grown GaAs. Journal of Crystal Growth 237-239, 345–349 (2002).

[Bir03] B. Birkmann. *Züchtung und Charakterisierung von versetzungsarmen Silizium-dotierten GaAs-Substratkristallen.* PhD thesis, Universität Erlangen-Nürnberg, 2003.

[Bir05] B. Birkmann, J. Stenzenberger, M. Jurisch, J. Hartwig, V. Alex and G. Muller. Investigation of residual dislocations in VGF-grown Si-doped GaAs. Journal of Crystal Growth 276, 335–346 (2005).

[Bly97] J. M. Bly, M. L. Kaforey, D. H. Matthiesen and A. Chait. Interface shape and growth rate analysis of Se/GaAs bulk crystals grown in the NASA crystal growth furnace (CGF). Journal of Crystal Growth 174, 220–225 (1997).

[Bou91] E. Bourret and E. C. Merk. Effects of total liquid encapsulation on the characteristics of GaAs single crystals grown by the vertical gradient freeze technique. Journal of Crystal Growth 110, 395–404 (1991).

[Bue01] Th. Buenger, D. Behr, St. Eichler, T. Flade, W. Fliegel, M. Jurisch, A. Kleinwechter, U. Kretzer, Th. Steinegger and B. Weinert. Development of a vertical gradient freeze process for low EPD GaAs substrates. Materials Science and Engineering: B 80, 5–9 (2001).

[Bue06] Th. Buenger. *Ein Beitrag zur Kohlenstoffkontrolle bei der VGF- Züchtung von semi-isolierenden GaAs-Kristallen*. PhD thesis, Technischen Universität Bergakademie Freiberg, 2006.

[Bue08] F. Buellesfeld, U. Sahr, W. Miller, P. Rudolph, U. Rehse and N. Dropka. Verfahren zum Erstarren einer Nichtmetall-Schmelze, patent DE102008059521B4, 2008.

[Bur53] J. A. Burton, R. C. Prim and W. P. Slichter. The Distribution of Solute in Crystals Grown from the Melt. Part I. Theoretical. The Journal of Chemical Physics 21, 1987 (1953).

[Cam86] D. Camel and J. J. Favier. Scaling analysis and segregation of convective solute transport in Bridgman crystal growth from the doped melt. Journal of Crystal Growth 47, 1001–1014 (1986).

[Car88] D. J. J. Carlson and A. F. Witt. Determination of free charge carrier distribution and micro-segregation of dopants in n-type GaAs. Journal of Crystal Growth 91, 239–243 (1988).

[Car91] D. J. Carlson and A. F. Witt. Microsegregation in conventional Si-doped LEC GaAs. Journal of Crystal Growth 108, 508–518 (1991).

[Cha83] C. J. Chang and R. A. Brown. Radial segregation induced by natural convection and melt/solid interface shape in vertical Bridgman growth. Journal of Crystal Growth 63, 343–364 (1983).

[Cor79] S. R. Coriell and R. F. Sekerka. Lateral solute segregation during undirectional solidification of a binary alloy with a curved solid-liquid interface. Journal of Crystal Growth 46, 479–482 (1979).

[Cra11] A. Cramer, J. Pal, K. Koal, S. Tschisgale, J. Stiller and G. Gerbeth. The sensitivity of a travelling magnetic field driven flow to axial alignment. Journal of Crystal Growth 321, 142–150 (2011).

[Cul80] A. G. Cullis, P. D. Augustus and D. J. Stirland. Arsenic precipitation at dislocations in GaAs substrate material. Journal of Applied Physics 51, 2556 (1980).

[Cza98] M. Czapelski. Variable equilibrium partition coefficient. Journal of Crystal Growth 187, 138–139 (1998).

[Dad13] K. Dadzis, K. Niemietz, O. Pätzold, U. Wunderwald and J. Friedrich. Non-isothermal model experiments and numerical simulations for directional solidification of multicrystalline silicon in a traveling magnetic field. Journal of Crystal Growth 372, 145–156 (2013).

[Dol99] P. Dold and K. W. Benz. Rotating magnetic fields: fluid flow and crystal growth applications. Progress in Crystal Growth and Characterization of Materials 38, 7–38 (1999).

[Dre93] B. Drevet, J. P. Garandet, D. Camel and J. J. Favier. Influence of thermal bouyancy on fibrous eutectic growth I. Segregation results in the SnCu6Sn5 system. Journal of Crystal Growth 129, 549–558 (1993).

[Dre08] W. Dreyer, F. Duderstadt, St. Eichler and M. Naldzhieva. On unwanted nucleation phenomena at the wall of a VGF chamber. WIAS Preprint ISSN 0946- (2008).

[Dro10] N. Dropka, W. Miller, R. Menzel and U. Rehse. Numerical study on transport phenomena in a directional solidification process in the presence of travelling magnetic fields. Journal of Crystal Growth 312, 1407–1410 (2010).

[Dro11] N. Dropka, W. Miller, U. Rehse, P. Rudolph, F. Büllesfeld, U. Sahr, O. Klein and D. Reinhardt. Numerical study on improved mixing in silicon melts by double-frequency TMF. Journal of Crystal Growth 318, 275–279 (2011).

[Dro12a] N. Dropka, Ch. Frank-Rotsch, W. Miller and P. Rudolph. Influence of travelling magnetic fields on S–L interface shapes of materials with different electrical conductivities. Journal of Crystal Growth 338, 208–213 (2012).

[Dro12b] N. Dropka, Ch. Frank-Rotsch and P. Rudolph. Numerical study on stirring of large silicon melts by Carousel magnetic fields. Journal of Crystal Growth 354, 1–8 (2012).

[Dro13a] N. Dropka and Ch. Frank-Rotsch. Accelerated VGF-crystal growth of GaAs under traveling magnetic fields. Journal of Crystal Growth 367, 1–7 (2013).

[Dro13b] N. Dropka, Ch. Frank-Rotsch and P. Rudolph. Comparison of stirring efficiency of various non-steady magnetic fields during unidirectional solidification of large silicon melts. Journal of Crystal Growth 365, 64–72 (2013).

[Dro13c] N. Dropka, Ch. Frank-Rotsch, M. Ziem and P. Lange. Verfahren und Vorrichtung zur gerichteten Kristallisation von Kristallen aus elektrisch leitenden Schmelzen, patent DE102012204313B3, 2013.

[Dro14a] N. Dropka and Ch. Frank-Rotsch. Enhanced VGF-GaAs growth using pulsed unidirectional TMF. Journal of Crystal Growth 386, 146–153 (2014).

[Dro14b] N. Dropka, A. Glacki and Ch. Frank-Rotsch. GaAs - VGF Process Intensification. Crystal Growth and Design, DOI: 10.1021/cg500814m (2014).

[Duf00] T. Duffar, P. Dusserre, F. Picca, S. Lacroix and N. Giacometti. Bridgman growth without crucible contact using the dewetting phenomenon. Journal of Crystal Growth 211, 434–440 (2000).

[Eic05] St. Eichler. Parameterstudien zur VGF-Züchtung von GaAs. DGKK-Workshop Angewandte Simulation in der Kristallzüchtung (2005).

[Eic08a] St. Eichler, F. Börner, Th. Bünger, M. Jurisch, A. Köhler, U. Kretzer, M. Scheffer-Czygan, B. Weinert and T. Flade. Recent Progress in GaAs Growth Technologies at FREIBERGER. In *Crystal Growth Technology*, chapter 9, pages 230–266. (Wiley-VCH Verlag GmbH & Co. KGaA, 2008).

[Eic08b] St. Eichler, Th. Bünger, M. Butter, R. Rühmann and M Scheffer-Czygan. Anordnung und Verfahren zur Herstellung eines Kristalls aus der Schmelze eines Rohmaterials sowie Einkristall, patent DE102007026298A1, 2008.

[FR07] Ch. Frank-Rotsch, P. Rudolph, O. Klein, P. Lange and B. Nacke. Vorrichtung und Verfahren zur Herstellung von Kristallen aus elektrisch leitenden Schmelzen, patent DE102007028548B4, 2007.

[FR08] Ch. Frank-Rotsch, D. Jockel, M. Ziem and P. Rudolph. Numerical optimization of the interface shape at the VGF growth of semiconductor crystals in a traveling magnetic field. Journal of Crystal Growth 310, 1505–1510 (2008).

[FR09] Ch. Frank-Rotsch and P. Rudolph. Vertical gradient freeze of 4 inch Ge crystals in a heater-magnet module. Journal of Crystal Growth 311, 2294–2299 (2009).

[FR10] Ch. Frank-Rotsch and P. Rudolph. Vorrichtung und Verfahren zur Züchtung von Kristallen aus elektrisch leitenden Schmelzen in Mehrtiegelanordnungen, patent DE102008034029A1, 2010.

[FR12] Ch. Frank-Rotsch, U. Juda, B. Ubbenjans and P. Rudolph. VGF growth of 4in. Ga-doped germanium crystals under magnetic and ultrasonic fields. Journal of Crystal Growth 352, 16–20 (2012).

[Fra95] Ch. Frank. *Züchtung undotierter VGF-GaAs-Kristalle unter besonderer Berücksichtigung der Einstellung halbisolierender Eigenschaften*. Phd thesis, Technische Universität Bergakademie Freiberg, 1995.

[Fuj70] K. Fujimori and T. Ayusawa. Vorrichtung zum Züchten von Einkristallen aus Schmelzen, patent DE000002107646A, 1970.

[Gar90] J. P. Garandet, T. Duffar and J. J. Favier. On the scaling analysis of the solute boundary layer in idealized growth configurations. Journal of crystal growth 106, 437–444 (1990).

[Gar94] J. P. Garandet, J. J. Favier and D. Camel. Segregation phenomena in Crystal Growth from the Melt. In D.T. J. Hurle, editor, *Handbook of Crystal Growth 2b*, chapter 12, pages 661–707. (North-Holland, 1994).

[Gau86] W. Gault. A novel application of the vertical gradient freeze method to the growth of high quality III–V crystals. Journal of Crystal Growth 74, 491–506 (1986).

[Gil86] L. J. Giling, J. L. Weyher and A. Montree. Influence of Si and S doping on structural defects in LEC-grown gallium arsenide. Journal of Crystal Growth 79, 271–279 (1986).

[Gil96] E. Gilioli, J. L. Weyher, L. Zanotti and C. Mucchino. Growth Striations in GaAs as Revealed by DSL Photoetching. Materials Science Forum 203, 13–18 (1996).

[Gra04] I. Grants and G. Gerbeth. Stability of melt flow due to a traveling magnetic field in a closed ampoule. Journal of Crystal Growth 269, 630–638 (2004).

[Gra08] I. Grants and G. Gerbeth. Use of a traveling magnetic field in VGF growth: Flow reversal and resulting dopant distribution. Journal of Crystal Growth 310, 3699–3705 (2008).

[Gra09] I. Grants, A. Klyukin and G. Gerbeth. Instability of the melt flow in VGF growth with a traveling magnetic field. Journal of Crystal Growth 311, 4255–4264 (2009).

[Han99] C. Hannig, G. Schwichtenberg, E. Buhrig and G. Gärtner. Study of silicon-doped VGF-GaAs by DSL-etching and LVM spectroscopy and the influence of B2O3 coating. Materials Science and Engineering: B 66, 97–101 (1999).

[Hig12] E. Higham. 2011 GaAs Market Trends & Results. Technical report, 2012.

[Hig13] E. Higham. GaAs Industry Overview and Forecast : 2011 – 2016. CS MANTECH Conference, New Orleans, Louisiana, USA (2013).

[Hor58] J. Hornstra. Dislocations in the diamond lattice. Journal of Physics and Chemistry of Solids 5, 129–141 (1958).

[Hos80] K. Hoshikawa, H. Kohda, H. Hirata and H. Nakanishi. Low oxygen content Czochralski silicon crystal growth. Japanese Journal of Applied Physics 19, L33–36 (1980).

[Hur94] D. T. J. Hurle and R. W. Series. Use of a Magnetic Field in Melt Growth. In D.T. J. Hurle, editor, *Handbook of Crystal Growth 2a*, chapter 5, pages 261–283. (North-Holland, 1994).

[Hur95] D. T. J. Hurle. A mechanism for twin formation during Czochralski and encapsulated vertical Bridgman growth of III–V compound semiconductors. Journal of Crystal Growth 147, 239–250 (1995).

[Hur99] D. T. J. Hurle. A comprehensive thermodynamic analysis of native point defect and dopant solubilities in gallium arsenide. Journal of Applied Physics 85, 6957 (1999).

[Hur04] D. T. J. Hurle and P. Rudolph. A brief history of defect formation, segregation, faceting, and twinning in melt-grown semiconductors. Journal of Crystal Growth 264, 550–564 (2004).

[Ind79] V. L. Indenbom. Ein Beitrag zur Entstehung von Spannungen und Versetzungen beim Kristallwachstum. Kristall und Technik 14, 493–507 (1979).

[Jas85] T. Jasinski and A. F. Witt. On control of the crystal-melt interface shape during growth in a vertical Bridgman configuration. Journal of Crystal Growth 71, 295–304 (1985).

[Jun97] T. Jung and G. Müller. Amplitudes of doping striations: comparison of numerical calculations and analytical approaches. Journal of Crystal Growth 171, 373–379 (1997).

[Jur05] M. Jurisch, F. Borner, T. Bunger, S. Eichler, T. Flade, U. Kretzer, A. Kohler, J. Stenzenberger and B. Weinert. LEC- and VGF-growth of SI GaAs single crystals - recent developments and current issues. Journal of Crystal Growth 275, 283–291 (2005).

[Kas08] H. Kasjanow, B. Nacke, S. Eichler, D. Jockel, Ch. Frank-Rotsch, P. Lange, F. Kiesling, P. Rudolph and F. Kiessling. Investigation of asymmetry effects in a heater-magnet module for TMF VGF and LEC growth by three-dimensional numerical modeling. Journal of Crystal Growth 310, 1540–1545 (2008).

[Kla00] H. Klapper. Generation and propagation of dislocations during crystal growth. Materials Chemistry and Physics 66, 101–109 (2000).

[Koh95] H. J. Koh, T. Fukuda, M. H. Choi and I. S. Park. Twins in GaAs Crystals Grown by the Vertical Gradient Freeze Technique. Crystal Research and Technology 30, 397–403 (1995).

[Kor99] J. Korb, T. Flade, M. Jurisch and A. Köhler. Carbon, oxygen, boron, hydrogen and nitrogen in the LEC growth of SI GaAs: a thermochemical approach. Journal of Crystal Growth 199, 343–348 (1999).

[Kud13] Ch. Kudla, A. T. Blumenau, F. Büllesfeld, N. Dropka, Ch. Frank-Rotsch, F. Kiessling, O. Klein, P. Lange, W. Miller, U. Rehse, U. Sahr, M. Schellhorn, G. Weidemann, M. Ziem, G. Bethin, R. Fornari, M. Müller, J. Sprekels, V. Trautmann and P. Rudolph. Crystallization of 640kg mc-silicon ingots under traveling magnetic field by using a heater-magnet module. Journal of Crystal Growth 365, 54–58 (2013).

[Lan07a] P. Lange, D. Jockel, M. Ziem, P. Rudolph, F. Kiessling, Ch. Frank-Rotsch, M. Czupalla, B. Nacke and H. Kasjanow. Vorrichtung zur Herstellung von Kristallen aus elektrisch leitenden Schmelzen, patent DE102007028547B4, 2007.

[Lan07b] R. Lantzsch, V. Galindo, I. Grants, C. Zhang, O. Patzold, G. Gerbeth and M. Stelter. Experimental and numerical results on the fluid flow driven by a traveling magnetic field. Journal of Crystal Growth 305, 249–256 (2007).

[Lan08] R. Lantzsch, I. Grants, O. Patzold, M. Stelter and G. Gerbeth. Vertical gradient freeze growth with external magnetic fields. Journal of Crystal Growth 310, 1518–1522 (2008).

[Lan09] R. Lantzsch. *VGF-Kristallzüchtung unter dem Einfluss externer Magnetfelder*. Phd thesis, Technische Universität Bergakademie Freiberg, 2009.

[Lan10] D. Langheinrich, O. Pätzold, L. Raabe and M. Stelter. VGF growth of germanium single crystals without crucible contact. Journal of Crystal Growth 312, 2291–2296 (2010).

[Lan12] P. Lange, D. Jockel, M. Ziem, P. Rudolph, F. Kiessling, Ch. Frank-Rotsch, M. Czupalla, B. Nacke and H. Kasjanow. Device for producing crystals from electroconducting melts, patent EP2162570B1, 2012.

[Lei04] H. Lei, H. S. Leipner, V. Bondarenko and J. Schreiber. Identification of the 0.95 eV luminescence band in n-type GaAs:Si. Journal of Physics: Condensed Matter 16, S279–S285 (2004).

[Lyu04] T. P. Lyubimova, A. Croell, P. Dold, O. Khlybov and I. S. Fayzrakhmanova. Time-dependent magnetic field influence on GaAs crystal growth by vertical Bridgman method. Journal of Crystal Growth 266, 404–410 (2004).

[Mar80] G. M. Martin, J. P. Farges, G. Jacob, J. P. Hallais and G. Poiblaud. Compensation mechanisms in GaAs. Journal of Applied Physics 51, 2840 (1980).

[Mar08] M. Marchenko, W. Liu, M. Badawi and P. Yin. The influence of the scatter of heat flux at the m/c interface on the frequency of appearance of poly body and twin defects during 6" semi-insulating GaAs crystal growth by the VGF method. Journal of Crystal Growth 310, 2134–2140 (2008).

[Mit06] A. Mitric, T. Duffar, C. Diazguerra, V. Corregidor, L. Alves, C. Garnier and G. Vian. Growth of Ga(1-x)InxSb alloys by Vertical Bridgman technique under alternating magnetic field. Journal of Crystal Growth 287, 224–229 (2006).

[Mo83] P. Mo, J. Yang, L. Shouchun, D. Jiang and H. Zhao. A modified horizontal gradient-freeze technique for growth of dislocation-free Si-doped GaAs single crystals. 65, 243–248 (1983).

[Mue03] A. Muehe, B. Altekrüger and A. Vonhoff. Kristallzüchtungsanlage, patent DE000010349339A1, 2003.

[Mue12] G. Mueller. Crystal Growth - From Fundamentals to Technology. IKZ Summer School (2012).

[Nau00] M. Naumann, J. Donecker and M. Neubert. Laser scattering experiments in VCz GaAs. Journal of Crystal Growth 210, 203–206 (2000).

[Nau01] M. Naumann, P. Rudolph, M. Neubert and J. Donecker. Dislocation studies in VCz GaAs by laser scattering tomography. Journal of Crystal Growth 231, 22–30 (2001).

[Nau06] M. Naumann and F.-M. Kiessling. Axiale Verteilung von Punktdefekten in VGF GaAs:Si. DGKK-Workshop Massive Halbleiterkristalle (2006).

[Neu01] M. Neubert and P. Rudolph. Growth of semi-insulating GaAs crystals in low temperature gradients by using the Vapour Pressure Controlled Czochralski Method (VCz). Progress in Crystal Growth and Characterization of Materials 43, 119–185 (2001).

[New94] R. C. Newman. The lattice locations of silicon impurities in GaAs: effects due to stoichiometry, the Fermi energy, the solubility limit and DX behaviour. Semiconductor science and technology 9, 1749 (1994).

[Nie11] K. Niemietz, V. Galindo, O. Pätzold, G. Gerbeth and M. Stelter. Flow modelling with relevance to vertical gradient freeze crystal growth under the influence of a travelling magnetic field. Journal of Crystal Growth 318, 150–155 (2011).

[Nis93] J. Nishio and H. Fujita. Ambient gas constituents and segregation of carbon and boron in LEC GaAs single crystals: the role of water in boric oxide encapsulants. Journal of Crystal Growth 134, 97–104 (1993).

[Oga89] T. Ogawa. A study on dislocation lines in an In-doped LEC GaAs crystal by IR light scattering and transmission microscopy. Journal of crystal growth 96, 777–784 (1989).

[Ost92] A. Ostrogorsky and G. Müller. A model of effective segregation coefficient, accounting for convection in the solute layer at the growth interface. 121, 587–598 (1992).

[Pae02a] O. Paetzold, I. Grants, U. Wunderwald, K. Jenkner, A. Croll and G. Gerbeth. Vertical gradient freeze growth of GaAs with a rotating magnetic field. Journal of Crystal Growth 245, 237–246 (2002).

[Pae02b] O. Paetzold, I. Grants, U. Wunderwald, K. Jenkner, A. Croll and G. Gerbeth. Vertical gradient freeze growth of GaAs with a rotating magnetic field. Journal of Crystal Growth 245, 237–246 (2002).

[Pae04] O. Paetzold, U. Wunderwald, M. Bellmann, P. Gumprich, E. Buhrig and A. Cröll. New Developments in Vertical Gradient Freeze Growth. Advanced Engineering Materials 6, 554–557 (2004).

[Pae05] O. Paetzold, K. Jenkner, S. Scholz and A. Cröll. Detached growth behaviour of 2-in germanium crystals. Journal of Crystal Growth 277, 37–43 (2005).

[Pae13] O. Paetzold, R. Lantzsch, V. Galindo, I. Grants, M. Bellmann and G. Gerbeth. The use of magnetic fields in vertical Bridgman/Gradient Freeze-type crystal growth. The European Physical Journal Special Topics 220, 243–257 (2013).

[Pri05] J. Priede and G. Gerbeth. Breakdown of Burton–Prim–Slichter approach and lateral solute segregation in radially converging flows. Journal of crystal growth 285, 261–269 (2005).

[Pri07] J. Priede and G. Gerbeth. Matched asymptotic solution for the solute boundary layer in a converging axisymmetric stagnation point flow. International Journal of Heat and Mass Transfer 50, 216–225 (2007).

[Rud99] P. Rudolph and M. Jurisch. Bulk growth of GaAs An overview. Journal of Crystal Growth 198-199, 325–335 (1999).

[Rud04] P. Rudolph, Ch. Frank-Rotsch, U. Juda, M. Naumann and M. Neubert. Studies on dislocation patterning and bunching in semiconductor compound crystals (GaAs). Journal of Crystal Growth 265, 331–340 (2004).

[Rud07] P. Rudolph, Ch. Frank-Rotsch, U. Juda, St. Eichler and M. Scheffer-Czygan. Studies on dislocation patterning in 6-inch GaAs crystals. Physica Status Solidi (C) 4, 2934–2939 (2007).

[Rud08a] P. Rudolph. Travelling magnetic fields applied to bulk crystal growth from the melt: The step from basic research to industrial scale. Journal of Crystal Growth 310, 1298–1306 (2008).

[Rud08b] P. Rudolph, Ch. Frank-Rotsch, F.-M. Kiessling, W. Miller, U. Rehse, O. Klein, Ch. Lechner, J. Sprekels, B. Nacke, H. Kasjanow, P. Lange, M. Ziem, B. Lux, M. Czupalla, O. Root, V. Trautmann and G. Bethin. Crystal growth in heater-magnet modules-from concept to use. Proceedings of the International Scientific Colloquium Modelling for Electromagnetic Processing, 79–84 (2008).

[Rud09a] P. Rudolph, M. Czupalla and B. Lux. LEC growth of semi-insulating GaAs crystals in traveling magnetic field generated in a heater–magnet module. Journal of Crystal Growth 311, 4543–4548 (2009).

[Rud09b] P. Rudolph and K. Kakimoto. Crystal growth from the melt under external force fields. MRS Bulletin 34, 251–258 (2009).

[Sat90] N. Sato, K. Kakimoto and Y. Kadota. Proc. Conference Semi-Insulating III-V-Materials. (Adam Hilger, Bristol, 1990).

[Sch42] E. Scheil. Bemerkungen zur Schichtkristallbildung. Z. Metall. 34, 70–72 (1942).

[Sch92] P. Schlossmacher, K. Urban and H. Rüfer. Dislocations and precipitates in gallium arsenide. Journal of Applied Physics 71, 620 (1992).

[Sch04a] R. Schenk, V. Hessel, Ch. Hofmann, J. Kiss, H. Löwe and A. Ziogas. Numbering-up of micro devices: a first liquid-flow splitting unit. Chemical Engineering Journal 101, 421–429 (2004).

[Sch04b] P. Schwesig, M. Hainke, J. Friedrich and G. Mueller. Comparative numerical study of the effects of rotating and travelling magnetic fields on the interface shape and thermal stress in the VGF growth of InP crystals. Journal of Crystal Growth 266, 224–228 (2004).

[Sek78] Y. Seki, H. Watanabe and J. Matsui. Impurity effect on grown-in dislocation density of InP and GaAs crystals. Journal of Applied Physics 49, 822 (1978).

[Shi93] M. Shibata, T. Suzuki, S. Kuma and T. Inada. LEC growth of large GaAs single crystals. Journal of Crystal Growth 128, 439–443 (1993).

[Shi09] Shin-Etsu Chemical Co. Ltd., Pyrolytic Boron Nitride, 2009.

[Son97] K. Sonnenberg and E. Kussel. Developments in vertical Bridgman growth of large diameter GaAs. III-Vs Review 10, 30–34 (1997).

[Son00] K. Sonnenberg, E. Küssel, Th. Bünger, T. Flade and B. Weinert. Verfahren und Vorrichtung zur Herstellung von Einkristallen sowie Kristallkeim, patent DE19912486A1, 2000.

[Sta00] A. Stankiewicz and J. A. Moulin. Process intensification. Chemical Engineering Progress, 22–34 (2000).

[Ste03] J. Stenzenberger, Th. Bünger, F. Börner, St.. Eichler, T. Flade, R. Hammer, M. Jurisch, U. Kretzer, S. Teichert and B. Weinert. Growth and characterization of 200mm SI GaAs crystals grown by the VGF method. Journal of Crystal Growth 250, 57–61 (2003).

[Til53] W. A. Tiller, K. A. Jackson, J. W. Rutter and B. Chalmers. The redistribution of solute atoms during the solidification of metals. Acta Metallurgica 1, 428–437 (1953).

[Tow91] J. P. Tower, R. Tobin, P. J. Pearah and R. M. Ware. Interface shape and crystallinity in LEC GaAs. Journal of Crystal Growth 114, 665–675 (1991).

[Ubb12] B. Ubbenjans. *Einsatz von Vibratoren und Ultraschall in der Züchtung von Halbleiterkristallen für die Photovoltaikindustrie.* PhD thesis, Wilhelm Leibniz Universität Hannover, 2012.

[Ueh00] K. Uehara and H. Okada. Multiple single crystal producing device, patent JP2000203981A, 2000.

[vB86] H. J. von Bardeleben, D. Stiévenard, D. Deresmes, A. Huber and J. C. Bourgoin. Identification of a defect in a semiconductor: EL2 in GaAs. Physical Review B 34 (1986).

[vdP58] L. J. van der Pauw. A method of measuring specific resistivity and Hall effect of discs of arbitrary shape. Philips Research Reports 13, 1–9 (1958).

[Vol99] T. Volkmann, P. R. Sahm and I. Egry. *Schmelze, Erstarrung, Grenzflächen: Eine Einführung in die Physik und Technologie flüssiger und fester Metalle.* (Friedr. Vieweg & Sohn Verlagsgesellschaft mbH Braunschweig/Wiesbaden, 1999).

[Wal79] W. Walukiewicz, L. Lagowski, L. Jastrzebski, M. Lichtensteiger and H. C. Gatos. Electron mobility and free-carrier absorption in GaAs: Determination of the compensation ratio. Journal of Applied Physics 50 (1979).

[Wan06] X. Wang, N. Ma, D. Bliss and G. Iseler. Solute segregation during modified vertical gradient freezing of alloyed compound semiconductor crystals with magnetic and electric fields. International Journal of Heat and Mass Transfer 49, 3429–3438 (2006).

[Wey83] J. L. Weyher and J. Van de Ven. Selective etching and photoetching of {100} Gallium arsenide in CrO3-HF aqueous solutions: I. Influence of composition on etching behaviour. Journal of Crystal Growth 63, 285–291 (1983).

[Wey86] J. L. Weyher and J. Van de Ven. Selective etching and photoetching of GaAs in CrO3-HF aqueous solutions:: III. Interpretation of defect-related etch figures. Journal of Crystal Growth 78, 191–217 (1986).

[Wil78] Lynn O Wilson. On interpreting a quantity in the burton, prim and slichter equation as a diffusion boundary layer thickness. Journal of Crystal Growth 44, 247–250 (1978).

[Wil88] K.-Th. Wilke and J. Bohm. *Kristallzüchtung*. (VEB Deutscher Verlag der Wissenschaften, 1988).

[Wu07] A. Wu. Bridgman growth of langasite-type piezoelectric crystals. Crystal Research and Technology 42, 862–866 (2007).

[Wun06] U. Wunderwald. *Beeinflussung des Wärme- und Stofftransports bei der Vertical Gradient Freeze-Kristallzüchtung durch ein rotierendes Magnetfeld*. PhD thesis, Technische Universität Bergakademie Freiberg, 2006.

[Xu04] J. Xu, S. Fan and B. Lu. Growth of 4" Li2B4O7 single crystals by multi-crucible Bridgman method. Journal of Crystal Growth 264, 260–265 (2004).

[Yol12] Yole Développment. GaAs wafer market & applications. Technical Report April 2012, 2012.

[Yu86] M. L. Yu. Chemical enhancement effects in SIMS analysis. Nuclear Instruments and Methods in Physics Research B15, 151–158 (1986).

[Zha12] N. Zhang, A. Yeckel and J. J. Derby. Maintaining convex interface shapes during electrodynamic gradient freeze growth of cadmium zinc telluride using a dynamic, bell-curve furnace profile. Journal of Crystal Growth 355, 113–121 (2012).

[Zie07] M. Ziem, P. Rudolph and P. Lange. Vorrichtung zur Herstellung von Kristallen aus elektrisch leitfähigen Schmelzen, patent DE102007020239B4, 2007.

List of Figures

List of Tables

Acknowledgment

First of all, I would like to thank Dr. Christiane Frank-Rotsch for the excellent support, the fruitful cooperative work, for sharing her long-term expertise in the field of VGF growth, and for helpful comments on this thesis. Furthermore, this work would not have been possible without the other two members of the GaAs group at the IKZ Berlin: I am thankful to Dr. Natasha Dropka for numerical simulations, inspiring discussions, helpful suggestions, and her effort in proofreading of parts of this thesis. A large thank you to Oleg Root for the excellent experimental support in the laboratory.

I am indebted to Prof. Dr. Roberto Fornari for giving me the opportunity to work in the field of crystal growth at the IKZ Berlin, for his ongoing interest in my research, and useful comments. I would like to thank Prof. Dr. Peter Wellmann and Prof. Dr. Matthias Bickermann for the interest in my work their willingness to review this thesis.

I am specially grateful to Dr. Uta Juda for DSL etching and EPD analysis and Martin Naumann for IR transmission, LST, and residual stress measurements. Comprehensive and fruitful discussions helped to generate a deeper understanding.

I am thankful to Ralph-Peter Lange, Mario Ziem, Uwe Kupfer, Bernd Spotowitz, Jörg Fischer, Friedemann Münter, and Jens Klose for their contributions to the growth setup, technical help, and their fast responds to one or another special request.

I want to express my gratitude to further colleagues at IKZ: Manuela Imming-Friedland, Viola Lange, and Thomas Wurche for crystal machining and sample polishing, Mike Pietsch for Hall measurements, Albert Kwasniewski for XRD measurements, Dr. Klaus Irmscher for discussions and measurement efforts, and Dr. Frank-Michael Kießling for his interest in my work and occasional suggestions. Thanks also to my roommates Robert Menzel, Nico Werner, and Michael Wünscher for interesting discussions and the good atmosphere during work.

Furthermore, I would like to thank Georg Bethin and Bernd Eberhardt from AUTEAM Industrie-Elektronik GmbH for excellent collaboration during the start-up of the multi-crucible VGF setup and Freiberger Compound Materials GmbH for financial support of this project.

Last but not least, I want to thank my parents for the all-embracing support, my girlfriend Juli for sharing her life with me and little Henri for the pleasant distraction.

Publications

Journal publications:

A. Glacki, N. Dropka, Ch. Frank-Rotsch, U. Juda, and M. Naumann. Characterization of 4 inch VGF GaAs single crystals grown in a heater-magnet module. Journal of Crystal Growth 397, 6-12 (2014).

Ch. Frank-Rotsch, N. Dropka, A. Glacki, and U. Juda. VGF growth of GaAs utilizing heater-magnet module. Journal of Crystal Growth 401, 702-707 (2014).

N. Dropka, A. Glacki, and Ch. Frank-Rotsch. GaAs VGF Process Intensification. Crystal Growth & Design, Accepted Manuscript, DOI: 10.1021/cg500814m (2014).

Conference contributions:

A. Glacki, Ch. Frank-Rotsch, U. Juda, and O. Root. Erste Züchtungsergebnisse von 4"-VGF-GaAs Kristallen mit kombiniertem Heizer-Magnet-Modul. German Conference on Crystal Growth (DKT) 2012 in Freiberg/Germany, March 2012.

A. Glacki, Ch. Frank-Rotsch, U. Juda, M. Naumann, and N. Dropka. Züchtung und Charakterisierung von 4"-VGF-GaAs Kristallen im Heizer-Magnet-Modul. DGKK Workshop on Bulk Semiconductors in Freiberg/Germany, October 2012.

A. Glacki, Ch. Frank-Rotsch, U. Juda, and M. Naumann. Influence of a traveling magnetic field on micro- and macrosegregation during VGF growth of 4"-GaAs. German Conference on Crystal Growth (DKT) 2013 in Erlangen/Germany, March 2013.

A. Glacki, Ch. Frank-Rotsch, M. Naumann, and U. Juda. Improvement of VGF growth of 4" GaAs single crystals with traveling magnetic fields. IV World Materials Summit and Forum for Next Generation Researchers in Strasbourg/France, October 2013.

Selbständigkeitserklärung

Ich erkläre, dass ich die vorliegende Arbeit selbständig und nur unter Verwendung der angegebenen Literatur und Hilfsmittel angefertigt habe.

Ich habe mich an keiner anderen Universität um einen Doktorgrad beworben und besitze keinen entsprechenden Doktorgrad.

Ich habe Kenntnis der dem Verfahren zugrunde liegenden Promotionsordnung der Mathematisch-Naturwissenschaftlichen Fakultät der Humboldt-Universität zu Berlin.

Berlin, den 14. Mai 2014 Alexander Glacki